Doctoral Dissertation
博士論文

Capsule-shaped metallic InGaAs/InP cavity laser for photonic integrated circuits
−proposal, simulation and demonstration

(光集積回路に向けたカプセル形状 InGaAs/InP 金属共振器レーザの研究
−提案，解析，実証)

Baifu ZHANG

張　柏富

Department of Electrical Engineering and information Systems,

School of Engineering, The University of Tokyo

Capsule-shaped metallic InGaAs/InP cavity laser for photonic integrated circuits
−proposal, simulation and demonstration

(光集積回路に向けたカプセル形状
InGaAs/InP 金属共振器レーザの研究
−提案，解析，実証)

Baifu　Zhang

張　柏富

Under the supervision of
Professor Dr. Yoshiaki Nakano

June　2015

Abstract

Large scale photonic integrated circuits (PICs), as a future target for a wide range of applications such as optical communication, interconnects, biological/chemical sensing, and imaging, have attracted researchers' interest and efforts over the past years. To achieve this goal, more complex and higher-capacity of PICs is increasingly demanded, also called "Photonic Moore's Law" (PML) that is proposed in 2012. One natural strategy of pursuing PML is miniaturizing the photonic devices with acceptable sacrifice of the property.

Semiconductor laser, as one of the most indispensable and important devices in PICs, has been experiencing a shrinking-size revolution since 2007, when the first metal-coated semiconductor cavity laser is demonstrated experimentally by electrical pumping. The idea of using metallic clad is based on utilizing the advantage of strong confinement of light by metal, which dramatically miniaturizes laser size and path the way to deep sub-wavelength region (even nano scale). A variety of different types of metallic semiconductor cavities are proposed and studied recently, basically including circular shape cavity with Whispering-Galley (WG) mode and rectangular shape cavity with Fabry-Perot (FP) mode.

One major challenge of the revolution of metallic laser is the huge optical loss from the metal. Some natural considerations, which are studied in previous works, are utilizing high gain material such as InGaAs/InGaAsP Multiple Quantum Wells (MQW), and operating lasers in low temperature. Besides, continuous effort of improving fabrication technology and thus reducing loss caused by the imperfection of cavity shape and property, is another key to get better performance of metallic lasers. So here is a natural question: what is next progress of metallic cavity lasers, especially after efforts such as choosing high gain material, operating at low temperature and improving the fabrication technique to a bottle neck?

In this dissertation, a novel structure of capsule-shaped metallic semiconductor cavity laser is proposed for the first time, aiming at reducing the metallic loss and improving the cavity property. By introducing cylindrical ends with optimal curvature at both ends of the cavity, Gaussian-like mode profile can be formed inside, which drastically reduces the field overlap at the metallic sidewall and thus lower down the optical loss. This new structure is designed for FP mode, considering the fact that FP mode is relatively easier to be coupled into waveguide and applied in PICs. Also, the proposed idea mainly designs and optimizes the cavity shape, so that it is naturally compatible with other methods of improving metallic lasers.

In order to theoretically study the property of the proposed structure, a systematically numerical investigation is carried out by well-established computational method as 3 dimensional (3D) finite-difference time-domain (FDTD). The simulation results show an obvious improvement of cavity Q factors (more than 50%) by using the capsule-shaped structure. Meanwhile, the threshold gain and threshold current can be reduced exponentially when using this new design, which can be estimated from the rate equation theory. Many other interesting issues are also studied by simulation, including design of waveguide coupling, external radiation efficiency, far field pattern and so on.

Fabrication of the proposed capsule-shaped metallic semiconductor cavity is explored and improved. For such a tiny and characteristic cavity, many detailed but not trivial issues may hinder a perfect fabrication. All the information is discussed detailed in the dissertation, including improvement of lithography resolution, trade-off in dry etching and effort for good metal deposition.

Photoluminescence (PL) measurement of fabricated cavity is carried out to demonstrate the proposed structure in the form of proof of concept. Up to 4-fold improvement in the Q factor of the fabricated capsule-shaped cavity, compared with a conventional rectangular one, has been experimentally confirmed by PL

characterization with 532-nm wavelength focused beam at room temperature. The measured results are consistent with our simulation prediction of 3D FDTD method, and verify the effectiveness of introducing optimal curvature at the cavity ends.

In conclusion, a novel metallic semiconductor laser structure named as "capsule-shaped cavity" is proposed, simulated and demonstrated in this dissertation for the first time. It has been shown that the proposed design does have advantages to be applied as a compact light source in PICs. Both numerical and experimental results show the huge improvement of cavity Q factors by the original structure. Furthermore, the proposed structure is compatible with other works focused on material and fabrication improvement, so that capsule-shaped design open up the possibility of creating an ultra-small, low cost and high speed cavity laser for advanced applications in optical communication, interconnects, sensing and imaging.

Contents

Chapter 1

Introduction

1.1 Photonic integrated circuits

Human beings utilize light in the nature for a long history. Even from the prehistoric time, sunlight has been used in the form of collecting and focusing by the bulk of ice to make a fire. In ancient era, beacon-fire was used to alarm a war, taking the advantage of the fast speed of light. Around 16th and 17th centuries, accompany with the invention of the microscope and telescope, universe and micro cosmos broke into people's eyes, under the help of controlling light propagation in free space. Until last a few decades before, the advent of optical fiber, which is widely applied in telecommunication, takes people into a new region to use light propagation in waveguide.

Since 1969, the concept of Photonic Integrated Circuits (PICs) was proposed by Stewart E. Miller [1], PICs has been developed with great enthusiasm and opens up a new era. It is a revolution of controlling, designing and utilizing light in photonic devices with the connection of integrated waveguide, instead of propagation in free space, for the first time in human beings' whole history.

After decades of development, PICs has been able to integrate hundreds of components in one single chip [2] and realize several comprehensive functions such as optical switch [3-4], polarization-multiplexed differential quadrature phase-shift keying (PM-DQPSK) transmitter [5], arbitrary waveform generator [6], tunable wavelength router [7] and so on. Considering the numbers of integrated components in PICs is continuously increasing from single digit [8–10] at its infant age to hundreds recently, Moore's law in photonics is proposed [11], which can be compared to the fact that the number of transistors per chip becomes double every two years in microelectronics. Figure 1.1 shows the increasing complexity of InP-based PICs [11], by counting the numbers of integrated components in a single chip, including Arrayed Wavelength Gratings (AWGs), Multilmode Interferences (MMIs), Semiconductor Optical Amplifiers (SOAs) and modulators.
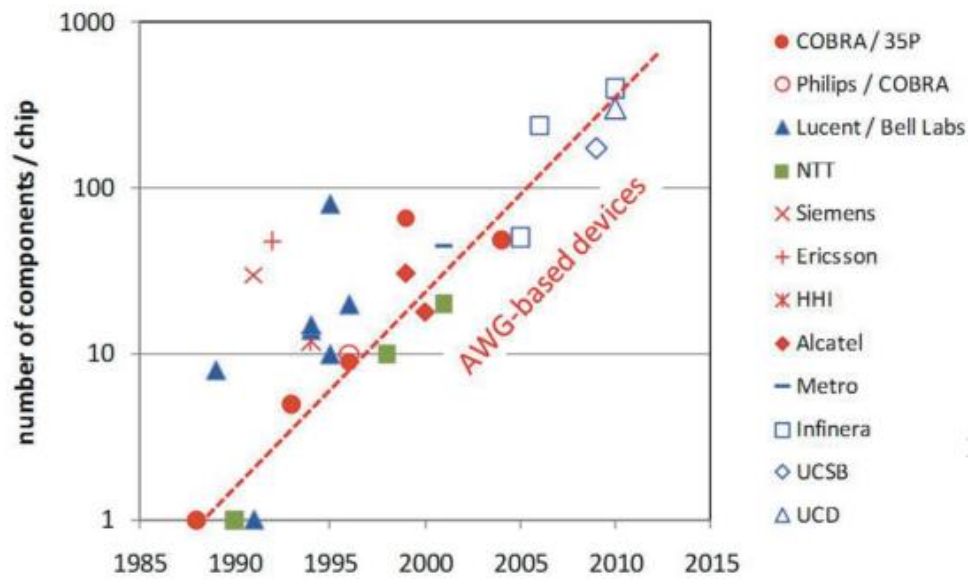
Figure 1.1 Photonics Moore's Law of PICs [11]. The number of components is counted in a single chip, including AWGs, MMIs, SOAs and modulators. It does not take into account the fact that a distributed feedback (DFB) laser has more complexity than a MMI coupler.

For large scale PICs which integrate hundreds of components and realize complicate functions, a natural design is collecting a variety of small basic components and devices in different topologies to form large circuits or systems. These small components include lasers, optical amplifiers, modulators, detectors, couplers, filters and (de)multiplexers. And by proper and logical design, these components and devices can be recounted into even smaller building blocks, which serve as combining, guiding and splitting light. Figure 1.2 shows a schematic of the basic building blocks in PICs [11].
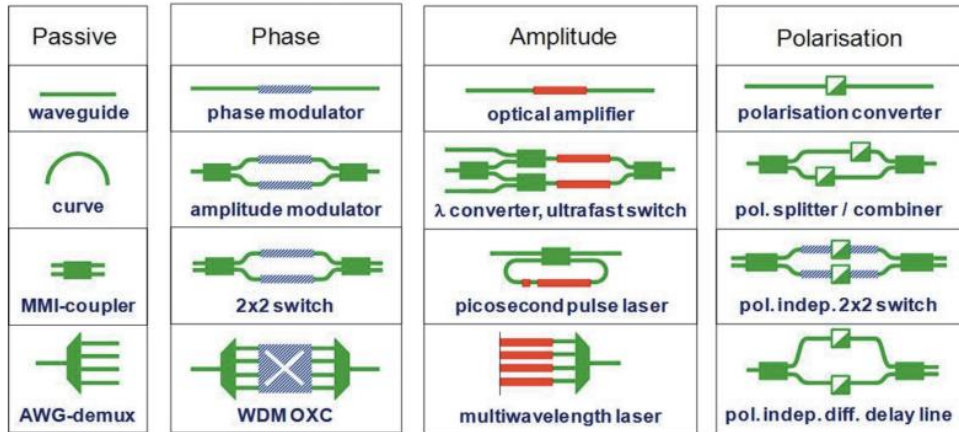
Figure 1.2 Functionalities of PICs that can be realized in a set of basic building blocks: passive waveguide devices, modulators, SOAs and polarization converters (PCs) [11].

For the functionalities and related components listed in Fig. 1.2, generic integration technology has developed over the past years and optimize them with an efficient integration in PICs [2]. And designing good performance of an active device such as light sources also plays an important role of large scale PICs in next generation, with higher capacity and more complexity. Micro or Nano lasers have small size and low cost, thus can be integrated in a large number on one single chip and potentially have high speed [12]. Thus, miniaturization of semiconductor lasers becomes one of the critical issues of achieving a large scale PICs in the future.

1.2 Trend of miniaturization of lasers

Since the first laser was demonstrated by Theodore Harold Maiman in 1960, the evolution of laser never stops. Just 2 years later, the first semiconductor laser was invented [13]–[16] and after that, many different types of lasers based on semiconductor gain materials [17]–[49] are studied and demonstrated for various applications such as light source, imaging, sensing, optical communications and so on [11], [50].

Recently, some novel types of small semiconductor lasers have been proposed and demonstrated, such as lambda-scale embedded active-region PhC laser (LEAP laser) [51]–[53], membrane distributed feedback (DFB) laser [54], [55], micropillar cavity laser [56], and three-dimensional photonic crystal (PhC) laser [57]. These lasers are designed with new structures to achieve high cavity quality factors (Q factors) and low energy cost, taking the advantages of PhC cavity, DFB, or distributed Bragg reflectors (DBRs) respectively.

As the growing demands for more complex and higher-capacity PICs operating at lower energy cost, the issue of shrinking the laser size becomes attractive to researchers. Figure 1.3 shows a brief history of miniaturizing the laser size [58].
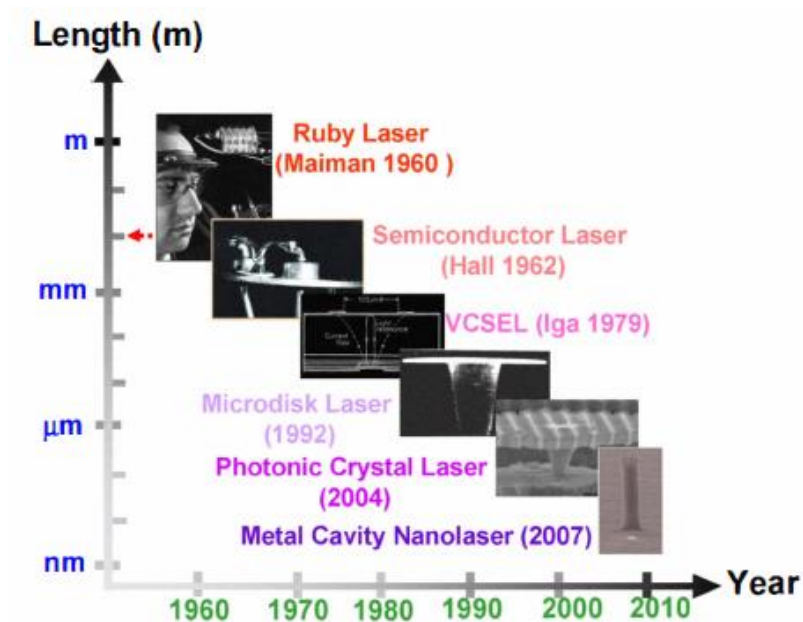
Figure 1.3 A brief history of miniaturization of lasers [58]. After 2007, metallic cavity structure becomes an important topology to shrink the laser size to deep sub-wavelength range and even in nano-scale.

From Fig. 1.3, we can see the trend of shrinking semiconductor laser size, from ~mm of the first demonstration to ~100 μm of Vertical Cavity Surface Emitting Laser (VCSEL) [42], then to a few micro-meters size of microdisk laser [59], and to sub-wavelength range of PhC laser [24]. And since 2007 when the metallic-

cavity semiconductor laser was demonstrated for the first time in the world [60], using metallic clad to get extremely tight confinement of light and thus shrink the laser size becomes a new method to achieve an ultra-small laser [61]–[75]. In this first demonstration, lasing wavelength around 1.4μm was achieved by a metallic pillar with diameter of only 260 nm, even under the diffractive limit. This milestone-like work enlighten researchers to study and design a variety of different metallic cavity lasers and path the way to deep sub-wavelength scale.

1.3 Metallic cavity semiconductor lasers

1.3.1 The role of metal in metal-clad semiconductor lasers

As the material with a negative permittivity in optical frequencies, metal (especially noble metal) exhibits different optical properties from that of dielectric materials. Why and how can metal help shrinking the laser size?

A quite intuitive understanding is the effect of skin depth. That is, the penetration depth of Electromagnetic (EM) wave into metal is usually much shorter than the wavelength. So if metal serves as a clad of semiconductor cavity, light can be confined tightly just inside. For more strict understanding in some cases of cavity size under diffraction limit, the effect of Surface Plasmon Polariton (SPP) should be taken into account. That is, when an EM field is incident into the interface of metal and dielectric, SPP can be stimulated if the electrical polarization has a component normal to the interface. It is a coupled oscillation between free electrons at the metal surface and an external electromagnetic field. SPP has higher effective refractive index than that of dielectric, thus can shrink the EM field profile into much smaller dimension, even under the diffraction limit.
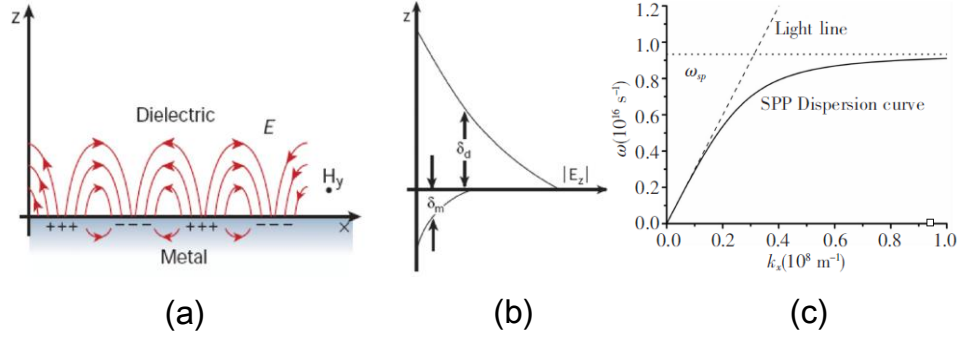
Figure 1.4 Schematic of SPP [76]. (a) stimulation of SPP; (b) penetration depth of SPP; (c) dispersion curve of SPP.

Figure 1.4 shows the schematic of the generation of SPP. According to the continuity of displacement vector $(D_z = \varepsilon_0\varepsilon_d E_{zd} = \varepsilon_0\varepsilon_m E_{zm})$, the electrical field is not continuous at the z direction normal to the interface, which causes a period bound charges along the interface shown in the Fig. 1.4 (a) . SPP mode propagates along the surface of the interface for a few micrometers (for superior design, this length can be larger), and can penetrate into the dielectric and metal plate for only tens of nanometers, shown in Fig. 1.4 (b).

The dispersion curve of SPP is depicted in Fig. 1.4 (c). The angular frequency and wave vector of SPP can be derived from Maxwell's Equations with the boundary condition of continuity of displacement vector [76], as following:

$$\omega_{spp} = \frac{\omega_p}{\sqrt{1+\varepsilon_d}},$$

(1.1)

$$k_{spp} = k\sqrt{\frac{\varepsilon_d\varepsilon_m}{\varepsilon_d+\varepsilon_m}},$$

(1.2)

where ω_p is the frequency of electron plasma, ε_d and ε_m is the permittivity of the dielectric material and metal respectively. From Eqs. (1.1) and (1.2) we can know SPP is a kind of electromagnetic wave coupled to the free-electrons in the

metal. The wave vector of SPP will reach to extremely large (infinite large if the imaginary part of the metal can be ignored) which means the moment of the wave is so large that the light is localized in somewhere. Large wave vector means large effective index (larger than that of dielectric and semiconductor materials), and thus SPP can help achieve extreme miniaturization of semiconductor lasers.

The penalty of using metal to confine the light field is the high metallic loss, coming from the image part of its permittivity. So another issue is that if metal is necessary to a small semiconductor laser in sub-wavelength scale, considering its high loss?

In order to illustrate the effect of metals on the sub-wavelength lasers, we can use FP theory to compare the metallic cavity with semiconductor cavity (without metal) for an intuitive understanding. The Q factor of FP cavity can be written as:

$$\frac{1}{Q} = \frac{1}{Q_{abs}} + \frac{1}{Q_{mirror}}, \tag{1.3}$$

$$\frac{1}{Q_{abs}} = \frac{v_g}{\omega}\alpha, \tag{1.4}$$

$$\frac{1}{Q_{mirror}} = \frac{v_g}{\omega}\frac{1}{L}\ln(\frac{1}{R}), \tag{1.5}$$

where Q_{abs} and Q_{mirror} are the Q values corresponding to the absorption loss and mirror loss, while v_g, α, L and R are the group velocity, propagation loss, cavity length and reflectivity of mirrors respectively. In sub-wavelength scale, usually around 1 micro-meter of the footprint, DBR, DFB and PhC structure are too large to be applied to achieve a high reflectivity. By introducing metal-clad outside the semiconductor cavity, the reflectivity of both cavity mirrors increases, which improves the Q factor. However, on the other hand, the propagation loss α will also be increased by metal, which will reduces the Q factor. These two factors compete with each other. Figure 1.5 plots the Q factors of both cavities as a function of cavity

length. (We use one dimensional simulation to calculate the reflectivity between InP and Air is 0.8, while the reflectivity with additional 20-nm SiO2 and 50-nm silver layers becomes 0.95. We assume different propagation loss α from 200 /cm to 400 /cm).
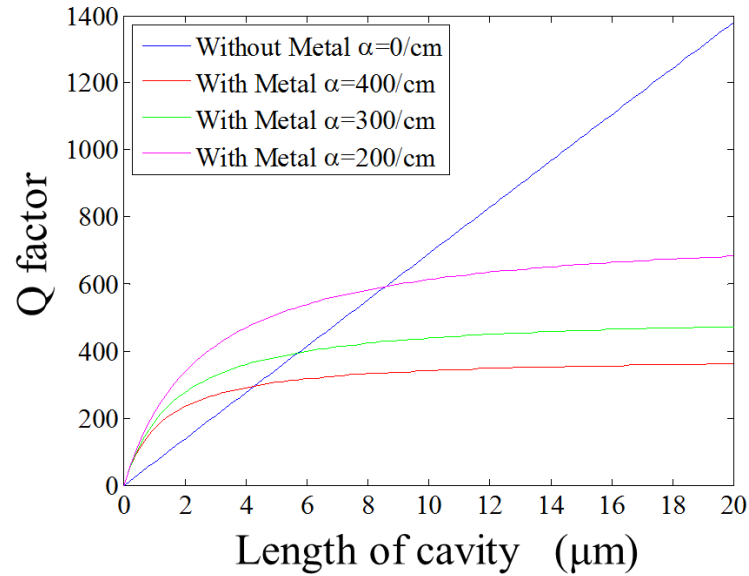
Figure 1.5 *Q* factors as a function of cavity length. The blue line is corresponding to the semiconductor cavity without metal-clad, while other three curves show the property of metallic FP cavity.

From Fig. 1.5, a self-explanatory result is that in small dimension of a few micro-meters, metallic cavities have higher *Q* factors rather than bared semiconductor cavity, which shows that the improvement of reflectivity overcomes the high metallic loss. While in the relatively large size, above 10 μm, even bared semiconductor cavity can achieve higher *Q* factor, as the mirror loss is diluted by longer cavity length. This result also illustrates the reason why metal is used after laser size is miniaturized into around micro-meter scale, shown in Fig. 1.3.

In short, metal plays a role in small lasers, not only for shrinking the laser size but also for increasing the reflectivity to reduce the mirror loss.

1.3.2 Demonstrations of sub-wavelength metallic semiconductor lasers

The first successful metallic laser is a semiconductor pillar cladded by gold [60]. The diameter is 260 nm which is under the diffraction limit. In this deep sub-wavelength dimension, SPP mode exists and surfers from quit high metallic loss. To achieve lasing, it is operated at low temperature of 10 k by 4-µA current injection. This demonstration attracts a host of interests of researchers and enlightens a new way to shrink laser size by metal.

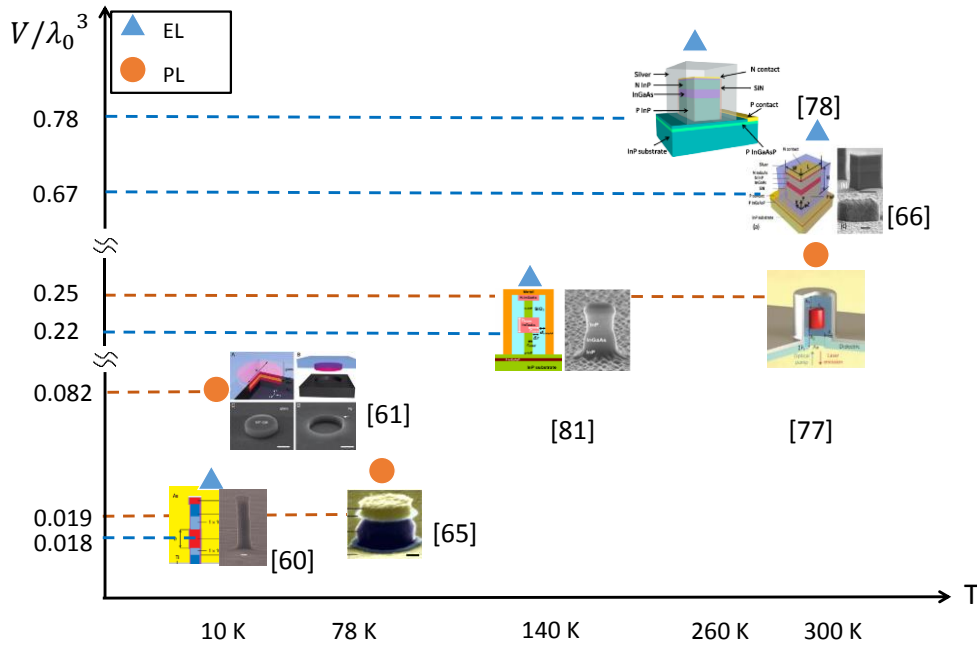Figure 1.6 Demonstrations of sub-wavelength metallic semiconductor lasers. The operation temperature and conditions are compared in the figure.

After that, many different designs with metals are studied and demonstrated, including circular cavities such as pillar [63], [67], [70], [71], [77], pan [61], disk

[65] and rectangular cavities [62], [64], [66], [78], [79], and even some novel structure with metallic element instead of cavity scheme [80]. All these metallic lasers utilize high gain materials (usually III-V semiconductors) to overcome the high loss, and most of them apply low temperature operation to lower down the loss in further. Some representative works are shown in Figure 1.6 [60], [61], [65], [66], [77], [78], [81].

1.4 Objective of this dissertation

State of the art of metallic semiconductor lasers is the trade-off and rebalance of two factors: scaling and loss. Except for choosing proper active materials with high gain and operating at low temperature, another natural consideration is to make efforts on improving fabrication technique, and thus improving the cavity properties. However, fabrication process of metallic cavity in such small scale (around 1 μm and even smaller) is so difficult that the space for improvement is not adequate [82]. So some new idea of reducing loss, which is independent on materials, fabrication technique and operation conditions, is necessary for metallic semiconductor lasers. This is the objective of this dissertation.

The dissertation will be organized as following:

In Chapter 1, a brief background of metallic semiconductor lasers is introduced.

In Chapter 2, a new structure called "capsule-shaped" cavity is proposed for the first time for metallic lasers, considering the mode selection, potential applications in PICs (for example, waveguide coupling and compatibility with other devices) and other issues.

In Chapter 3, some theory and analysis methods are introduced and applied on metallic semiconductor lasers.

In Chapter 4, 3D FDTD simulation is applied on the proposed structure and investigated many cavity properties, such as Q factor, confinement factor, threshold

gain, threshold current, radiation efficiency, *etc*. Near field (radiated field from the cavity) to far field transformation and waveguide coupling scheme is also taken into account in this chapter.

In Chapter 5, fabrication process of capsule-shaped metallic cavity is introduced. Some difficulties and limitations of fabrication technique is discussed and related effort on improvement is also given in this chapter.

In Chapter 6, PL measurement is applied on fabricated samples. Up to 4-fold improvement in the Q factor of the capsule-shaped cavity, comparing to its conventional rectangular alternation, has been experimentally confirmed. The measured results are consistent with our simulation prediction and demonstrate the proof of concept of capsule-shaped metallic semiconductor cavity structure.

In Chapter 7, a brief conclusion of this dissertation is made.

Chapter 2

Proposal of capsule-shaped metallic semiconductor laser

2.1 Topological-type selection of metallic semiconductor cavities

Among most demonstrations of metallic semiconductor laser up to now, circular-shape and rectangular-shape cavities are two basic topologies. These two types of cavities support WG mode (or circular mode) and FP mode inside respectively, thus exhibit different properties, including Q factors, laser size and possible waveguide coupling scheme. Some pioneering works of these two topological structures are compared in Figure 2.1.
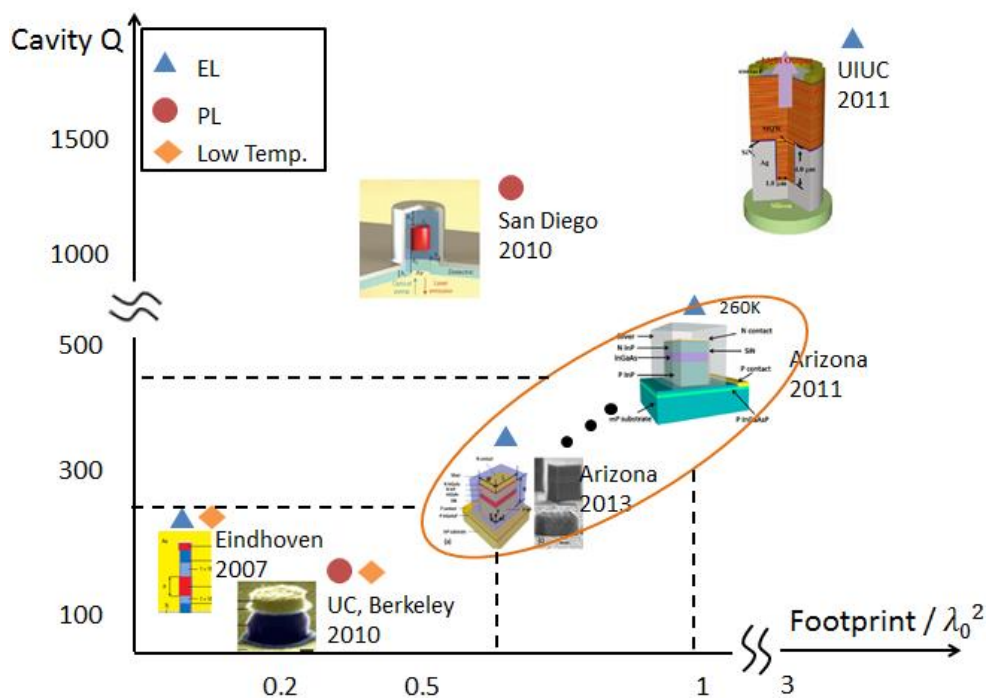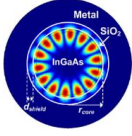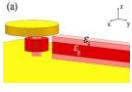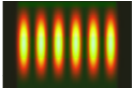

Figure 2.1 Some pioneering works of circular and rectangular metallic semiconductor cavities. Rectangular-topology cavity has moderate Q factor and footprint, compared with the circular one.

Fig. 2.1 shows the Q factors and footprints of two topologies. Circular cavities can achieve higher Q factors (above 1000) in the similar laser size than those of rectangular ones (usually around a few hundreds), which is coming from properties of WG modes. Thus, circular structures can achieve extremely small laser size, although under low-temperature operation, such as the pillar structure [60] and nano-patch structure [65]. While rectangular topologies, which support FP modes, both Q factors and footprints are in the moderate range (compared to circular topologies), and show a linear-like relationship. This is a natural property result from FP theory.

Except Q factors and footprint, some other properties should also be taken into account for possible applications in PICs, including confinement factor of gain materials (mainly depending on the resonant mode profile), waveguide coupling scheme. These characteristics are listed and compared in Table 2.1.

Table 2.1 Properties of two topological metallic cavity lasers

Topology	Mode type	Mode profile	Confinement factor	Waveguide coupling	Reference
Circular	Whispering -Galley				[85]
Rectangular	Fabry -Perot				[62], [86]

From Tab. 2.1, we can see that the profile of WG mode inside circular cavity is mainly distributed around the sidewall and have poor overlap with the active materials, leading to a relatively low confinement factor. As a contrast, rectangular

cavity support FP mode which has better overlap with gain materials and thus gets higher confinement factor.

Another issue is the scheme of waveguide coupling of these two topologies. For conventional circular cavities such as microdisks, in-plane waveguide coupling is usually applied; however, for achieving ultra-small dimension, metallic clad is used to shrink the laser size and thus hinder the conventional in-plane coupling [83], [84]. One possible solution is using only metallic top on the circular structure with bared semiconductor around the sidewall, which can be applied to in-plane coupling still [85]. However, circular-shaped semiconductor cavity with only metallic top partly sacrifices the ability of confinement of the light field, and is difficult in fabrication. For rectangular-shaped metallic cavity, light field can be coupled into waveguide under the substrate [62], [86], which is relatively easier to be fabricated.

Thus for potential applications in PICs, rectangular topology (or FP mode) is more suitable because of the advantages of higher confinement factors, ease of waveguide coupling and fabrications.

2.2 Mode selection inside metallic FP cavity

There exist two basic modes inside a rectangular cavity. If the electric polarization is normal to the metallic sidewall in the cross-section plane, it is defined as Transverse Electric (TE) mode. And its counterpart one-Transverse Magnetic (TM) mode is defined with a magnetic field normal to the sidewall.

As the existence of metallic clad, TE mode here can stimulate SPP at the interface of metal and dielectric layer, thus is also called plasmonic-like mode. As a contrast, TM mode still exhibits conventional dielectric property. Figure 2.2 shows the schematic of TE and TM modes in the cross-section plane of a metallic semiconductor waveguide. Note that we follow the conventional definition of TE and TM modes used for semiconductor waveguide lasers, but this definition may

be opposite to those used in the literatures on metal–insulator–metal (MIM) plasmonic lasers.
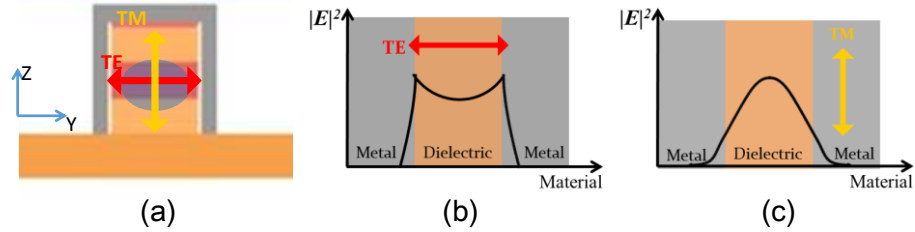
Figure 2.2 Schematic of TE and TM modes in the cross-section plane of metallic semiconductor waveguide: (a) definition; (b) and (c) mode profiles. The red and yellow arrows show the electric polarizations of TE and TM modes respectively.

TE and TM modes exhibit different properties in metallic semiconductor waveguide. With the help of SPP, TE modes can shrink the field distribution in a quite small area, even under diffraction limit, but suffers from high loss. Figure 2.3 shows the refractive index and propagation loss of TE and TM modes in metallic semiconductor waveguide [62]. Note that the exact values of these physical quantities are dependent on the detailed structure (materials, thickness, *etc.*), but the trend of these curves is meaningful.

From Fig. 2.3, a self-explantory fact is that TE mode has higher real part of the effective index rather than TM modes, which means TE mode can confine light field inside a smaller dimension. Furthermore, TM mode has the diffraction limit cut-off, similar to mode in conventional dielectric waveguide; while TE mode has no such cut-off. However, TE mode suffers from higher propagation loss than that of TM modes, as a penalty of its confinement ability.

From the electrical field distribution ($|E|$) of both modes (insert of Fig. 2.3), we can see that TE mode has better overlap with waveguide core in vertical direction, and thus has higher confinement factor than that of the TM mode. This is another

advantage of the TE mode. And other properties of TE mode such as the compatibility with other device, higher material gain by compressive MQW are also better than those of the TM mode.
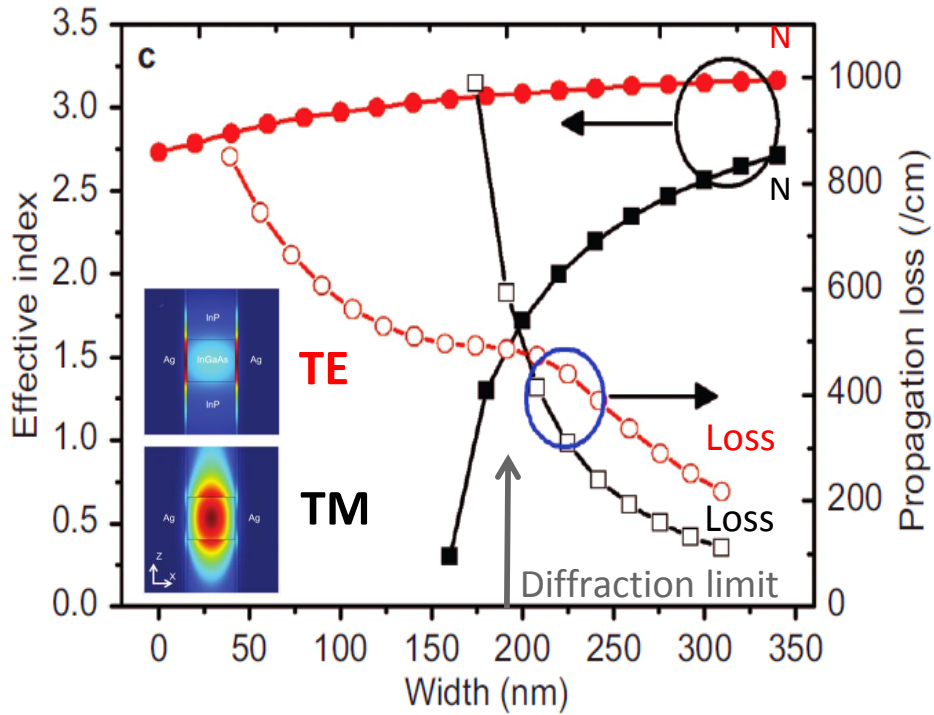
Figure 2.3 Effective index (real part) and propagation loss of TE (red curve) and TM (black curve) modes in a metallic semiconductor waveguide. Insert, mode patterns ($|E|$) of TE and TM modes [62].

As TE mode has many advantages discussed above, it is suitable for metallic cavity lasers used in PICs, in spite of its high loss. And the question "how to reduce the metallic loss of TE mode" becomes an important issue, which will be discussed and studied in the next section by proposing a new structure.

2.3 Proposal of capsule-shaped metallic FP cavity

From the above discussion, TE mode (plasmonic-like mode) within a FP cavity is more suitable for metallic semiconductor lasers for potential applications in PICs. However, due to the high metallic loss of TE mode, especially when narrowing down the cavity width, TM mode (dielectric-like mode) is selected as the lasing mode in the recent experiments with 1.3×1.1 μm^2 cavity [66]. Thus reducing the metallic loss effectively becomes a critical issue.

It should be mentioned that the benefits from lowering down the operation temperature, high gain materials and better fabrication are helpless for TE mode to compete with TM mode, as the latter one can also get these improvements equally. So some new design or scheme to reduce the metallic loss of TE mode is necessary, for improving the cavity property furtherly.

From the FP theory and Eqs. (1.3)-(1.5), the total loss of a rectangular metallic cavity comes from mirror loss ($\propto \frac{1}{L}\ln(\frac{1}{R})$) and propagation loss α. R is the reflectivity of the cavity mirrors and is almost fixed once the materials are selected. When shrinking the laser size, the length L decreases and thus the mirror loss increases. Thus, how to reduce the propagation loss α is critical.

(a) (b)
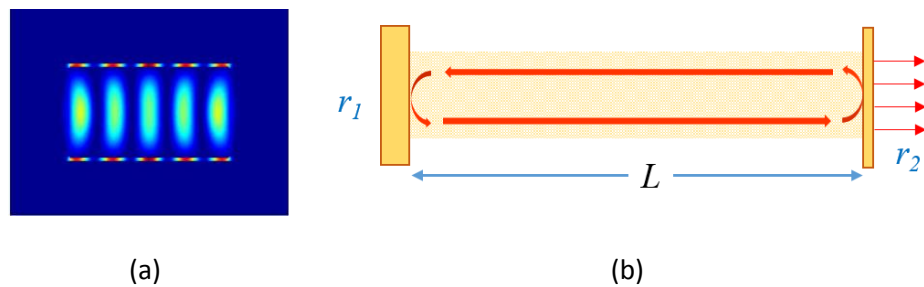
Figure 2.4 Schematic of light propagation in metallic FP cavity. (a) electrical field distribution ($|E|^2$) of TE mode in the top-view plane; (b) analogous to an open cavity with flat mirrors.

Figure 2.4 (a) shows the electrical field distribution ($|E|^2$) of the TE mode of a conventional FP cavity (rectangular topology), numerically calculated from 3D FDTD simulation, which will be discussed in detail in Chapter 3 and 4. The metallic loss is mainly from the SPP field which exists at the interface of metal and dielectric layer. If the field overlap at the metallic sidewalls can be reduced, the loss in the form of SPP should be decreased effectively.

Fig. 2.4 (b) makes an analogous comparison to macro lasers with an open cavity. Light propagates back and forth with mirror loss and has a plane wave-like profile. This can be regarded as an open cavity with flat mirrors at both ends. A classical improvement is using curved mirrors to make a stable cavity, which pushes the light field into the center and forms a Gaussian profile.

Now we think back to the metallic semiconductor cavity, if we imitate the improvement in an open cavity system and change the flat cavity ends to cylindrical ones, we should get a similar result. That is, Gaussian-like mode profile will be formed inside the cavity and the overlap at the metallic sidewalls should be dramatically reduced. In this way, metallic loss can be reduced effectively without sacrifice of the cavity dimension.
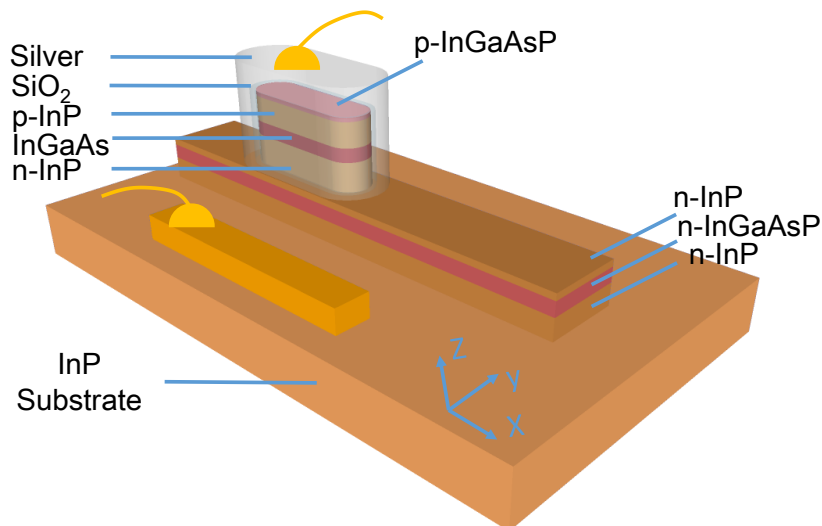
Figure 2.5 Schematic of the capsule-shaped metallic laser.

Here, a new structure with cylindrical mirrors of metallic semiconductor cavity laser is proposed for the first time, and is nominated as "capsule-shaped" cavity. Metallic cladding outside the semiconductor structure is not only used for a tight confinement of the light, but also acts like the electrode for current injection. The light mode of such a metallic cavity laser can be coupled into a waveguide vertically from the bottom side, which aims at potential applications in PICs. Figure 2.5 shows the schematic of the proposed structure. In order to demonstrate the proof of concept, design of this structure in detail (for example, the thickness of each layer, the length, width and curvature, *etc.*) and its related simulation, fabrication and measurement are studied, which will be discussed in following chapters.

2.4 Summary

In this chapter, different topologies and cavity modes of metallic semiconductor lasers are discussed in detail, and FP cavity with TE mode is suitable for the potential applications in PICs.
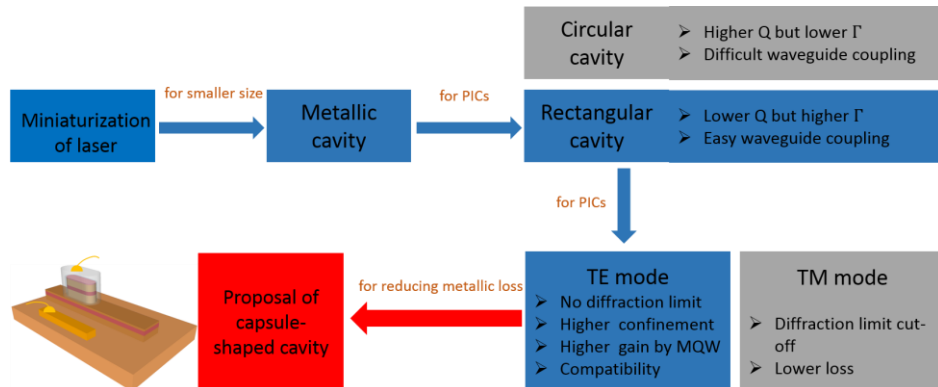
Figure 2.6 Roadmap of the proposal of capsule-shaped metallic semiconductor lasers.

In order to reduce the metallic loss, a new structure of FP cavity is proposed for the first time, with cylindrical mirrors instead of conventional flat ones. It is

nominated as "capsule-shaped" metallic semiconductor cavity. It should be mentioned that this proposal is based on the design of a topological structure, and thus is compatible with other methods of improving cavity properties, such as choosing high gain materials, using low optical-loss metal and reducing imperfection of fabrication by better technique. Figure 2.6 shows the roadmap of the proposal, as a summary of Chapter 2.

Chapter 3

Analysis and theories of metallic semiconductor laser

3.1 Introduction

Basic analysis of metallic semiconductor laser is discussed in this chapter. Firstly, by the rate equation theory, we can obtain an intuitive understanding of the behavior of semiconductor lasers. For steady-state, threshold gain and threshold current can be estimated as long as the cavity Q factor is known. Secondly, waveguide model is introduced to calculate the propagation loss of a FP-cavity based metallic semiconductor laser, for estimating the Q values. However, 2D waveguide model cannot precisely derive the propagation loss, the reflectivity loss and resonant wavelength of a 3D cavity, and cannot obtain some important information such as cavity mode pattern, external radiation ratio and radiate field, *etc*. Thus, a 3D based simulation is necessary. Thirdly, FDTD method is briefly introduced for the simulation of the proposed structure in this dissertation. And the near-to-far-field transformation (NFFT) method is also derived.

3.2 Rate equation analysis

3.2.1 General rate equation of semiconductor lasers

In semiconductor lasers, basically there exist two physical processes. One is the carrier generation and recombination in the active region, another is the photon generation and loss in the cavity.

For the first process, the current generation depends on the injection efficiency η_i, while the recombination is more complicated and includes many mechanisms such as spontaneous recombination R_{sp}, stimulated recombination R_{st}, non-radiative recombination R_{nr} and carrier leakage R_l. The stimulated recombination requires the presence of photons. The other three terms refer to natural or unstimulated carrier

decay processes, and can be described by empirical polynomial $AN + BN^2 + CN^3$, which estimate defect, spontaneous and Auger recombination, respectively.

For the other process, the main photon generation above threshold is stimulated recombination R_{st}, which is usually intuitively written in the form of optical gain. That is, when the light propagates in the active region for a unit length (enough small), the increase of the photon density can be described as the product of optical gain and propagated distance. Besides, spontaneous recombination process also contributes to the photon generation, and can be coupled into the lasing mode by a spontaneous emission factor. Considering that the active region occupied by the electrons is usually smaller than that occupied by photons, thus the concept of confinement factor Γ is introduced to describe the electron-photon overlap. On the other hand, the photon decay process is defined by the photon lifetime, which is related to the cavity Q factor.

According to the conservation of numbers of carriers and photons, rate equations can be written [87]:

$$\frac{dN}{\mathrm{dt}} = \frac{\eta_i I}{qV} - \frac{\mathrm{N}}{\tau} - v_g g N_p, \qquad (3.1)$$

$$\frac{dN_p}{dt} = \Gamma v_g g N_p - \Gamma \beta_{sp} R_{sp} - \frac{N_p}{\tau_p}, \qquad (3.2)$$

where N is the electron density, N_p is the photon density, τ is the carrier lifetime, τ_p is the photon lifetime, η_i is the current injection efficiency, I is injection current, q is the charge of the carrier (here is the electron), V is the volume of the active region, R_{sp} is the spontaneous recombination, β_{sp} is the spontaneous emission factor, Γ is the confinement factor, v_g is the group velocity of cavity mode, and g is the material gain of active region.

Based on the analysis of Eqs. (3.1) and (3.2), behavior of semiconductor lasers can be discussed, which is detailed in the next section.

3.2.2 Threshold gain and threshold current

Considering the photon generation and recombination processes which are described in Eq. (3.2), the steady-state is the photon decay rate equals to the photon generation rate, thus dN_p/dt is zero. If we neglect the spontaneous term, which is a small fraction coupled into the lasing mode, we can get the threshold gain [87],

$$g_{th} = \frac{1}{\Gamma v_g \tau_p},$$ (3.3)

where g_{th} is the threshold gain, Γ is the confinement factor, v_g is the group velocity of lasing mode, and τ_p is the photon lifetime.

The photon lifetime can be defined in the form of Q/ω, where Q is the cavity quality factor and ω is the angular frequency of the lasing mode. So g_{th} can be estimated naturally if Q is known:

$$g_{th} = \frac{\omega}{\Gamma v_g Q},$$ (3.4)

Another expression of the threshold gain is considering the loss inside the cavity by FP theory, can be written as:

$$g_{th} = \frac{1}{\Gamma}(\alpha_i + \frac{1}{L}\ln(\frac{1}{R})),$$ (3.5)

where α_i is internal modal loss of lasing mode during one round propagation, L is the length of the cavity and R is the reflectivity of the mirrors. By waveguide model, the propagation loss of the waveguide mode can be regarded as an approximation of α_i in Eq. (3.5) and thus can be used for estimation of g_{th}. This discussion will be included in the next section.

On the other hand, from the steady state of Eq. (3.1), threshold current can be estimated. Under steady state (dN/dt), the carrier generation rate equals to the

recombination rate. Taking into account that the stimulated recombination rate is a small fraction of total recombination and can be neglected here, Eq. (3.1) can be written as

$$I_{th} = \frac{qV}{\eta_i} \frac{N_{th}}{\tau}, \qquad (3.6)$$

where I_{th} is the threshold current and N_{th} is the threshold carrier density. The carrier density decay can be expressed as polynomial $AN + BN^2 + CN^3$ (here, the first term usually can be neglected), and the material gain can be written empirically in the form of carrier density as

$$g = g_{0N} ln \frac{N}{N_{tr}}, \qquad (3.7)$$

where g_{0N} is the empirical gain coefficient and N_{tr} is the transparency carrier density, both can be searched from experimental data. Finally the threshold current is derived as

$$I_{th} = \frac{qV(BN_{th}^2 + CN_{th}^3)}{\eta_i}, \qquad (3.8)$$

$$N_{th} = N_{tr} \exp(\frac{g_{th}}{g_{0N}}), \qquad (3.9)$$

Now the threshold gain and threshold current are derived from the rate equation theory. To estimate these values, only the photon lifetime or the cavity Q factor is needed. Next section will take waveguide analysis to calculate approximate threshold values for simplicity. More accurate and precise calculation will be done in the next chapter.

3.3 Waveguide analysis

From the discussion above, it is clear that the threshold gain and current of a semiconductor laser can be estimated if the cavity Q factor and confinement factor are known. To evaluate the Q factor precisely, 3D calculation is necessary, which is usually complicated and takes time. Before taking a strict 3D calculation, waveguides theory can be used firstly for an intuitive understanding and approximation of the semiconductor cavity, for simplicity.

Definition	Material	Thickness (nm)	Complex Refractive Index
Metal cover	Ag	200	0.469-9.32i
p-Contact	P-InGaAs	100	3.6+0.0984i
p-Clad	P-InP	500	3.16+0.0002i
buffer layer	U-InP	50	3.16
SCH	U-InGaAsP	100	3.39
MQW layer		150	3.53
SCH	U-InGaAsP	100	3.39
n-Clad	N-InP	700	3.17

SiO₂: thickness=20nm   n=1.45

Figure 3.1 Cross-section of 2D waveguide model of metallic semiconductor laser.

For a waveguide structure with multi layers (usually materials with different refractive indices), the electric field E and magnetic field H in each layer can be expressed by Helmhortz equation, which can be derived from the Maxwell's equations, if taking into account the condition of time harmonic field. Considering the boundary conditions that the normal components of both the electric and magnetic displacement vectors should be continues at the interface of two materials, the EM field distribution in a waveguide structure can be analytically derived.

Figure 3.1 shows the cross-section of the 2D waveguide model of metallic semiconductor lasers in previous work of our lab [88]. The resonant mode is regarded to propagate back and forth in a waveguide, and the cross-section of that waveguide with detailed parameters is shown in Fig. 3.1.

For this complicate structure of waveguide, analytical derivation is difficult while the simulation based on the finite element algorithm by COMSOL is carried out. The simulated propagation loss and confinement factor of TE and TM modes are shown in Figure 3.2 [88].
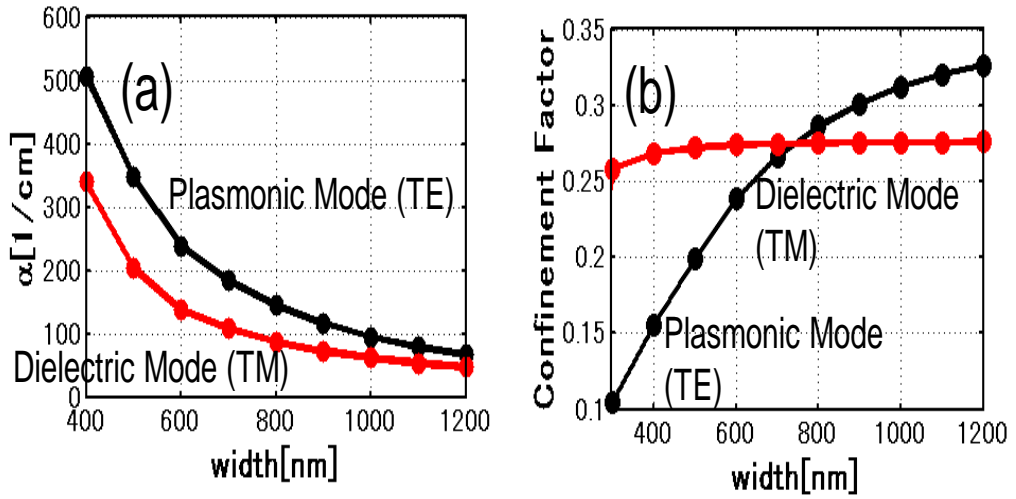
Figure 3.2 Propagation loss (a) and confinement factor (b) of TE and TM modes of the 2D waveguide in Fig. 3.1 [88].

From Fig. 3.2 (a), it is obvious that the propagation loss of TE mode is higher than that of TM mode, which is resulted from the high SPP loss of the TE mode. This point is discussed in detail in the previous chapters and is consistent with the result of Fig. 2.3, in which the propagation loss of similar waveguide shows the same trend above the diffraction limit. From Fig. 3.2 (b), the confinement factor of TM mode shows insensitive property to the dimension of waveguide, as the

dielectric mode profile does not change so much with varying width; however, as the SPP loss at the waveguide sidewalls depends heavily on the width, the confinement factor of TE mode decreases dramatically with narrower waveguide.

With the known propagation loss and confinement factors in Fig. 3.2, and using the formulation written in Eq. (3.5), threshold gain of metallic semiconductor lasers can be estimated by 2D waveguide model. Here, reflectivity of the waveguide end can be derived, using the model of a plane wave reflected by a flat mirror.

The waveguide method is a simplified model of a cavity, and cannot provide some important information such as the cavity mode pattern, the strict accurate Q factor and confinement factors. And as the waveguide model only solves the EM field distribution in one cross-section plane, by assuming that the resonant field inside the cavity should remain the same profile during propagation. This assumption can be acceptable in the case of conventional rectangular cavity, which using flat mirrors at the end of the waveguide. However, when the slope angles or undercut is introduced to the cavity, considering some practical issues that are caused from imperfections of fabrication process, the simple waveguide model can hardly give a solution. Furthermore, some new designs rather than the conventional rectangular structure, for example, the proposed capsule-shaped cavity, cannot be modelled by 2D waveguide.

Because of those limitations of the waveguide model, 3D analysis of metallic semiconductor cavity is necessary in this research.

3.4 3D analysis based on FDTD algorithm

For a 3D metal-clad cavity with isotropic material inside, the analytical solution of the EM field distribution can be theoretically derived. Nevertheless, for more complicated structures with multi-layers and materials, numerical-simulation methods are widely used. Among various algorithms, FDTD uses no linear algebra

and discretizes the Maxwell's equations in time domain, thus can treat nonlinear and impulsive behavior naturally [89]. As its accuracy and robustness, FDTD method is applied in this dissertation to solve the 3D simulation of metallic semiconductor cavities. By setting a dipole-source inside the cavity and recording the EM-field evolution in time domain, the Q factor can be analyzed from the decay of the field. By Fourier transform (FT), spectrum inside the cavity in the frequency domain also can be calculated, and the EM-field distribution of the resonant mode is obtained. Then the confinement factor can easily be calculated by a simple integration of the field overlap with the active material. The property of the simulated cavity can be estimated from these known quantities by Eqs. (3.4) and (3.8).

As the FDTD algorithm aims at the discretization of Maxwell's equations, the real size of the computational area depends on the concrete wavelength and structures involved in the simulation, considering the calculation efficiency and time. For the cases in this research, infrared light around 1.55 μm and the cavity scale of 1 μm are applied in the simulation, and the calculated EM field is in the near-field range. To investigate the property of radiation from the cavity in a macro range, which can be useful in characterization measurement and other concrete applications, NFFT rather than simulating the far field directly by FDTD is necessary. Analytical derivation of such transformation will be discussed briefly in the next section.

3.4.1 Near to far field transformation

According to the equivalence theorem, if the tangential components of electrical field E and magnetic field H of one enclosed surface maintain the same values, the EM field distribution outside that surface remains unchanged even though it varies inside that surface. Thus, the far field of the calculated cavity can be derived

theoretically, as long as the boundary condition of one enclosed surface of that cavity is obtained from the FDTD simulation. This efficient procedure is called near to far field transformation, shown in Figure 3.3.

Here, the fields to be computed can be written in the form of vector potentials

$$\vec{E}(\vec{r}) = -j\omega\mu\vec{A}(\vec{r}) + \frac{1}{j\omega\varepsilon}\nabla\left(\nabla\cdot\vec{A}(\vec{r})\right) - \nabla\times\vec{F}(\vec{r}) \qquad (3.10.\text{a})$$

$$\vec{H}(\vec{r}) = -j\omega\varepsilon\vec{F}(\vec{r}) + \frac{1}{j\omega\mu}\nabla\left(\nabla\cdot\vec{F}(\vec{r})\right) - \nabla\times\vec{A}(\vec{r}) \qquad (3.10.\text{b})$$

and

$$\vec{A}(\vec{r}) = \int\vec{J}(\vec{r})\,G(\vec{r},\vec{r}')dV' \qquad (3.11.\text{a})$$

$$\vec{F}(\vec{r}) = \int\vec{J}_m(\vec{r})\,G(\vec{r},\vec{r}')dV' \qquad (3.11.\text{a})$$

where ω is the angular frequency, ε and μ are the permittivity and permeability, $\vec{A}$ and $\vec{F}$ are the vector potentials, $\vec{J}$ and $\vec{J}_m$ are the equivalent currents of electrical and magnetic field, $G(\vec{r},\vec{r}')$ is the Green function in the free space, $\vec{r}$ and $\vec{r}'$ are the position vectors of the observation point and the source point respectively.
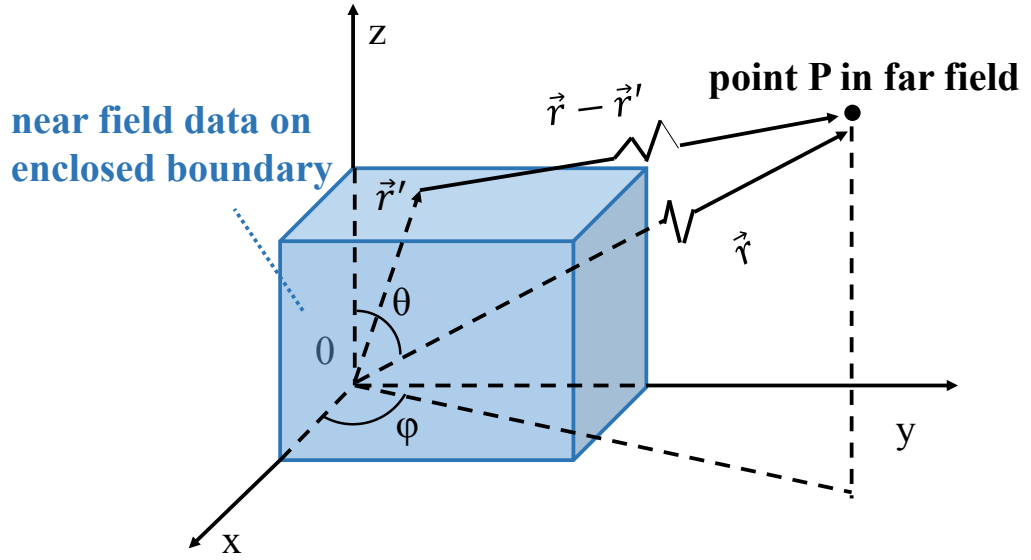
Figure 3.3 Schematic of NFFT, using the EM field on the enclosed boundary in near field.

In 3D case, the Green function can be written as

$$G(\vec{r}, \vec{r}') = \frac{\exp(-jk|\vec{r}-\vec{r}'|)}{4\pi|\vec{r}-\vec{r}'|} \approx \frac{\exp(-jkr)}{4\pi r} \exp(jk\vec{r}' \cdot \vec{e}_r) \qquad (3.12)$$

where $\vec{e}_r$ is the unit vector in the direction of $\vec{r}$. Here, far-field approximation of $|\vec{r} - \vec{r}'| \approx r - \vec{r}' \cdot \vec{e}_r$ is taken into account.

Using the far-field approximation of Green function in Eq. (3.12), vector potentials in Eq. (3.11) can be rewritten into

$$\vec{A}(\vec{r}) = \frac{\exp(-jkr)}{4\pi r} \int \vec{J}(\vec{r}') \exp(jk\vec{r}' \cdot \vec{e}_r) \, ds' = \frac{\exp(-jkr)}{4\pi r} \vec{f}(\theta, \varphi)$$

$$(3.13.a)$$

$$\vec{F}(\vec{r}) = \frac{\exp(-jkr)}{4\pi r} \int \vec{J}_m(\vec{r}') \exp(jk\vec{r}' \cdot \vec{e}_r) \, ds' = \frac{\exp(-jkr)}{4\pi r} \vec{f}_m(\theta, \varphi)$$

$$(3.13.b)$$

In far-field zone, considering that the operator ∇ can be replaced by $(-j\vec{k})$, and by projecting into spherical coordinates, the field in Eq. (3.10.a) can be rewritten into

$$
\begin{cases}
E_\theta = \frac{\exp(-jkr)}{4\pi r}(-jk)\left(Zf_\theta + f_{m\varphi}\right) \\
E_\varphi = \frac{\exp(-jkr)}{4\pi r}(-jk)\left(-Zf_\varphi + f_{m\theta}\right) \\
E_r = 0
\end{cases}
\tag{3.14}
$$

where $Z = \sqrt{\mu/\varepsilon}$ is the wave impedance. As the relationship between the electrical field E and magnetic field H in the far-field zone is similar to that of a plane wave, here the formulation of H is not necessary to list.

Eq. (3.14) is the far-field expression of the electrical field, which is derived from the vector-potential theory by the approximation of the far-field zone. Another issue is that the near field is numerical simulated by 3D-FDTD simulation, which is in the formulation of a rectangular coordinate system. To utilize the numerical data directly, transformation from rectangular to spherical coordinates is derived as following. Here the $\vec{f}(\theta, \varphi)$ and $\vec{f}_m(\theta, \varphi)$ in Eq. (3.13) can be obtained from numerical simulation in rectangular coordinates

$$
f_\xi = \int \vec{J}_\xi(\vec{r}') \exp(jkx' \sin\theta \cos\varphi + jky' \sin\theta \sin\varphi + jkz' \cos\theta)ds'
$$

$$
\tag{3.15.a}
$$

$$
f_{m\xi} = \int \vec{J}m_\xi(\vec{r}') \exp(jkx' \sin\theta \cos\varphi + jky' \sin\theta \sin\varphi + jkz' \cos\theta)ds'
$$

$$
\tag{3.15.b}
$$

where $\xi = x, y, z$ represents the components of the rectangular coordinates, respectively, while $\vec{J}_\xi$ and $\vec{J}m_\xi$ can be obtained by integration of the tangential components of the EM fields on the enclosed output plane (raw data from the 3D-FDTD simulation). And then substituting f_ξ and $f_{m\xi}$ into Eq. (3.14), the far field can be derived finally as following

$$
\begin{cases}
E_\theta = -jk \dfrac{\exp(-jkr)}{4\pi r}[Z(f_x \cos\theta \cos\varphi + f_y \cos\theta \sin\varphi - f_z \sin\theta) \\
\qquad + (-f_{mx} \sin\varphi + f_{my} \cos\varphi)] \\
E_\varphi = jk \dfrac{\exp(-jkr)}{4\pi r}[Z(f_x \sin\varphi - f_y \cos\varphi) + (f_{mx} \cos\theta \cos\varphi \\
\qquad + f_{my} \cos\theta \sin\varphi - f_{mz} \sin\theta)] \\
E_r = 0
\end{cases}
$$

(3.16)

3.5 Summary

In this chapter, theoretical analysis of metallic semiconductor cavity lasers is discussed. Firstly, from rate equation theory, threshold gain and current of a semiconductor cavity laser are derived in the form of empirical parameters of recombination and cavity-properties such as Q factor, confinement factor, *etc*. To calculate these values needed in estimation of threshold gain and current, waveguide theory is introduced and discussed for an intuitive understanding, in spite of the many limitations of this 2D model. For a rigorous and accurate study, 3D simulation based on FDTD algorithm is necessarily applied in this research. At last, the NFFT is also introduced and derived, based on the numerical data from the

FDTD simulation. In the next chapter, series of results by 3D-FDTD simulation of proposed capsule-shaped structure will be discussed in detail.

Chapter 4

Simulation results of capsule-shaped metallic semiconductor laser

4.1 Introduction

As discussed in Chapter 3, lasing behavior such as the threshold gain and threshold current can be estimated once the cavity Q factor is known. Considering that the waveguide model has limitations and can hardly take into account the radiation from the substrate, reflection at mirrors, resonant cavity mode, *etc.*, 3D calculation of the whole cavity is necessary.

In this chapter, 3D simulations of capsule-shaped metallic semiconductor cavity lasers are carried out in details. To evaluate the effectiveness of the proposed structure, a series of capsule-shaped cavities with sets of assumed parameters is taken into 3D FDTD simulation. The designed cavity is illustrated in Figure. 4.1 and related parameters are listed in Table 4.1 [90].
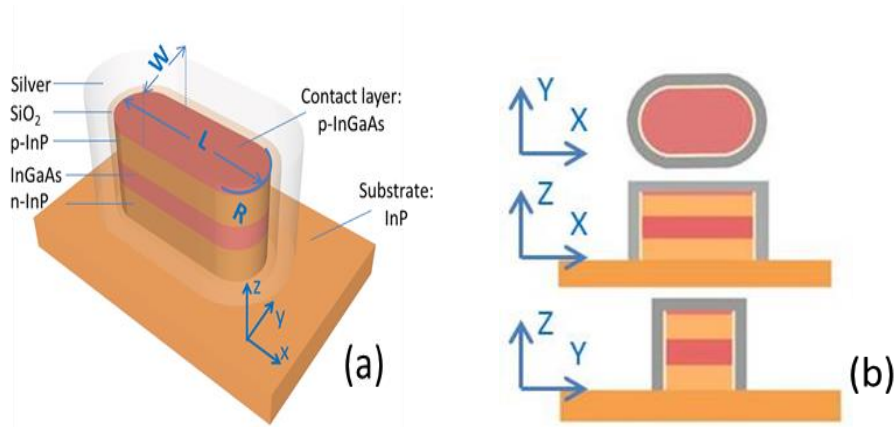

Figure. 4.1 The designed structure of capsule-shaped metallic semiconductor cavity that is used in the 3D FDTD simulation. (a) the 3D view, where W is the width, L is the length and R the curvature of cylindrical mirrors. (b) three cross-section planes.

Table 4.1. Material parameters used in 3D-FDTD simulations [90]. The definitions and thickness of each layers are corresponding to those in Fig. 4.1 (a). The permittivity of silver is fitted to the experimental values [105] by using a single Lorentzian pole [89].

Layer	Material	Thickness (nm)	Refractive index
Bottom clad	n-InP	500	3.17
Active core	InGaAs	300	3.53
Top clad	p-InP	500	3.17
Contact layer	p-InGaAs	100	$3.6+0.0984i$
Insulator layer	SiO_2	30	1.45
Metal clad	Silver	100	Lorentz fit to data

For the fully vectorial 3D FDTD simulation, B-CALM, an open-source simulator based on graphical processing units (GPUs) [91] is employed to rapid and efficient calculation. The discretization grid size is set to 10 nm, which shows good convergence in our calculation with confirmation. Taking into account the symmetry, only one-quarter of the structure (in the $x > 0$ and $y > 0$ region) is carried out into the computational cell. By setting perfect electrical conductor (PEC) or perfect magnetic conductor (PMC) boundary conditions at planes of $x = 0$ and $y = 0$ (center of the structure) respectively, either the TE or the TM mode can be selectively excited. For each of the other four boundaries, we set 15 convolutional perfectly matched layers (CPMLs) to eliminate the reflection [92].

Following sections will discuss simulation results under these settings in details.

4.2 Cavity *Q* factors and mode patterns

From 3D-FDTD simulation, the spectrum of resonant mode inside the cavity can be obtained by doing FT of the electrical field that decay in the time domain. Then cavity *Q* factor can be derived from the ratio of the resonant wavelength to the corresponding linewidth $\lambda/\Delta\lambda$.

The length (*L* in Fig. 4.1 (a), excluding SiO2) is fixed to 1100 nm and cavities with different values of width (*W* in Fig. 4.1 (a), excluding SiO2) are investigated. Here the length *L* and width W are elaborately selected, so that the resonant modes of the cavities fall within 1450–1650 nm wavelength range. Figure. 4.2 plots the *Q* values as a function of the mirror curvature *R* for the TE modes (plasmonic modes) and the TM modes (dielectric modes) respectively [90]. For simplicity, x-axis in Fig. 4.2 is defined as a ratio of cavity length *L* to the curvature *R*, so the case of *L/R* = 0 (*R* = ∞) corresponds to the conventional rectangular cavity.

From Fig. 4.2 (a), firstly, a self-evident fact is that, for all different values of width, the *Q* factors of the TE modes always increase by introducing the mirror curvature (for cases of *L/R* > 0). This result demonstrates our proposal of capsule-shaped structure does reduce the metallic loss, which is predicted in Chapter 2. Besides, for all cases with different width, the *Q* values increase along the x-axis and reach the maximum at *L/R* > 1. For example, in the case of *W* = 840 nm, the *Q* factor improves from 197 to 297 (about 51% increase) when *L/R* = 1.43.

From Fig. 4.2 (b), the *Q* factors of the TM modes exhibit no obvious correlation of the curvature of *R*. As for TM modes, no SPP is stimulated at the interface of metal and insulator layer, so that even cylindrical mirror pushes the light field far away from the metallic sidewall, it does not show much influence of *Q* values. So in the following discussion, only TE mode is investigated.
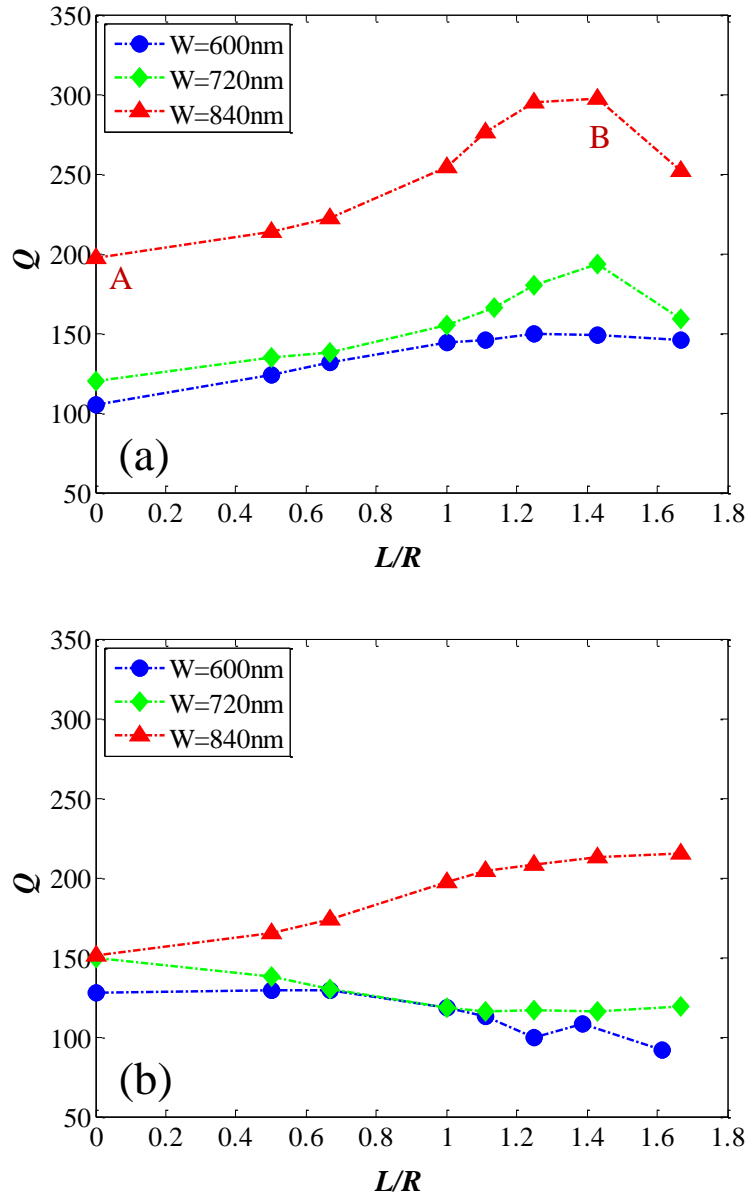
Figure. 4.2 Cavity Q factors of capsule-shaped metallic cavities for the TE (a) and TM (b) modes, as a function of the mirror curvature R. (L is fixed to 1100 nm, three cases of different widths are compared. Other parameters are written in the text.)

One thing should be mentioned is that, for a narrower cavity width ($W = 720$ or 600 nm), Fig. 4.2 (b) shows that the TM mode has initially higher Q than the TE mode when there is no curvature (L/R=0, conventional rectangular cavity). We attribute this to the larger metallic loss of the TE modes for narrow cavities [62], which is discussed in Chapter 2. However, by introducing the curvature (when L/R>0), the Q factor of the plasmonic mode gets effectively improved, exceeding that of the TM mode, which is actually not influenced much by the curvature. For example, in the case of $W = 720$ nm, the Q factor could be increased from 120 to 193 by the optimal curvature, and thus be able to achieve lasing of the TE mode in such a narrow-width cavity as well.
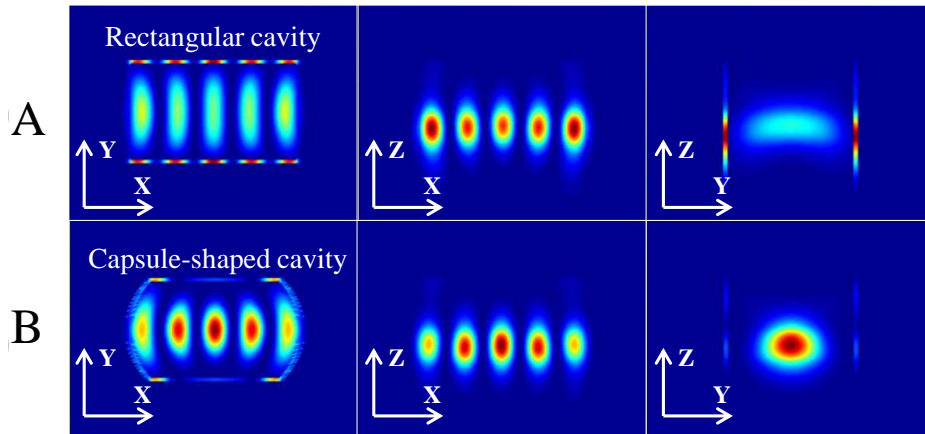
Figure. 4.3 Electric field distribution $|E|^2$ of the TE mode in three cross-section planes (xy, xz, and yz planes crossing the center of the cavity). The top and bottom rows respectively show the cases of the rectangular cavity ($L/R = 0$) and the optimized capsule cavity ($L/R = 1.43$) with the same width of $W = 840$ nm, corresponding to the two marked cases A and B in Fig. 4.2 (a).

The cavity mode pattern is also obtained from the 3D-FDTD simulation. Figure. 4.3 compares the electric field distribution of the TE mode for both rectangular and capsule-shaped cavities [90]. In the conventional rectangular case (*A* in Fig. 4.3),

significant amount of intensity is confined in the SiO2 layer, which contributes to the plasmonic loss. By introducing the curvature (*B* in Fig. 4.3), as a contrast, the field distribution is effectively pushed into the center of the cavity and its overlap with the metallic sidewalls is eliminated significantly. As a result, metallic loss of TE mode is reduced dramatically.
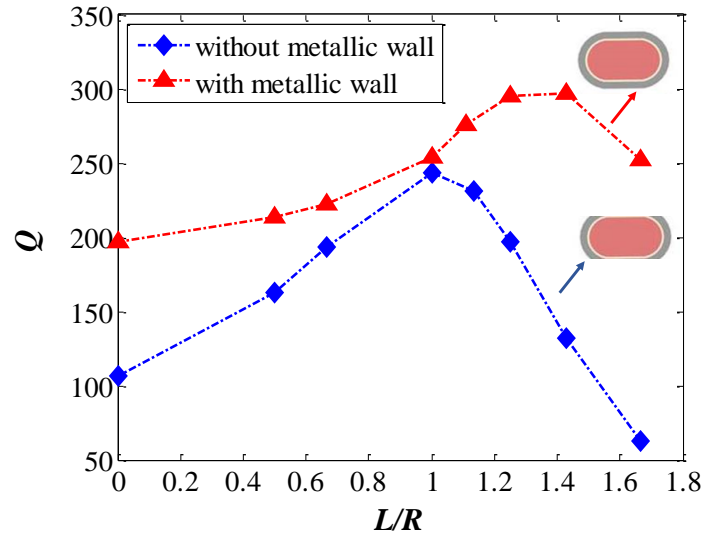
Figure 4.4 Cavity *Q* factors for the TE mode of capsule-shaped metallic cavities with (red curve) and without (blue curve) metallic walls respectively, as a function of the mirror curvature *R*. (*L* = 1100 nm, *W* = 840 nm. Other parameters are written in the text.) Inset, the schematic of the top view of a cavity in each case.

From Fig. 4.2 and 4.3, the effectiveness of capsule-shaped topology is numerically validated. Here comes a question, is the use of metals at the sidewalls necessary for such cavities with subwavelength dimension? One intuitive understanding is that, the metallic sidewalls can confine the light mode in the width dimension, however, it increases the metallic loss meanwhile. These two factors

compete with each other and a more rigorous discussion by 3D-FDTD simulation should be carried out.

Figure 4.4 shows the Q values as a function of the mirror curvature R for the TE modes of two capsule-shaped cavities with and without metallic sidewalls (all other structures and parameters of these two cavities maintain the same), respectively. First of all, the cavity without metallic sidewalls has lower Q value than that of its counterpart with an entire metallic clad. It can be explained that the radiation loss of the resonant mode from the cavity sidewalls overwhelms the metallic loss, because of the weak confinement of the light field in the narrow width dimension. One interesting thing is that for confocal topology ($L/R = 1$) in Fig. 4.4, the Q factors of both cases are almost the same, as the confocal cavity can confine the light mode like a perfect Gaussian-beam, which limits the radiation from the sidewalls. Meanwhile, metallic loss at the sidewalls is also reduced, and the cavities with and without metallic sidewalls show similar properties of Q factors.

From the discussions up to now and the results plotted in Fig. 4.2-4.4, it can be concluded that both the capsule-shaped topology and the entire metallic clad (including the metallic sidewalls) are necessary for increasing the cavity Q factors and reducing the optical loss.

From the mode pattern, confinement factor Γ can be derived by integrating the electric intensity $|E|^2$ inside the active InGaAs core layer, normalized by the total intensity. Figure 4.5 displays the confinement factor Γ of the TE mode inside the capsule-shaped cavity, as a function of the mirror curvature R [90]. Consistent with the Q factor in Fig. 4.2, the confinement factor Γ also shows obvious increase by introducing the mirror curvature. For the case with a narrow width ($W = 600$ nm or 720 nm), the improvement of Γ is more significant, as the curved mirror pushes the light field into the center of the cavity and reduces its overlap with the metallic sidewalls more effectively. In the case of $W = 600$ nm for instance, Γ improves from 0.366 to 0.488 (about 33% improvement) when $L/R = 1.67$.
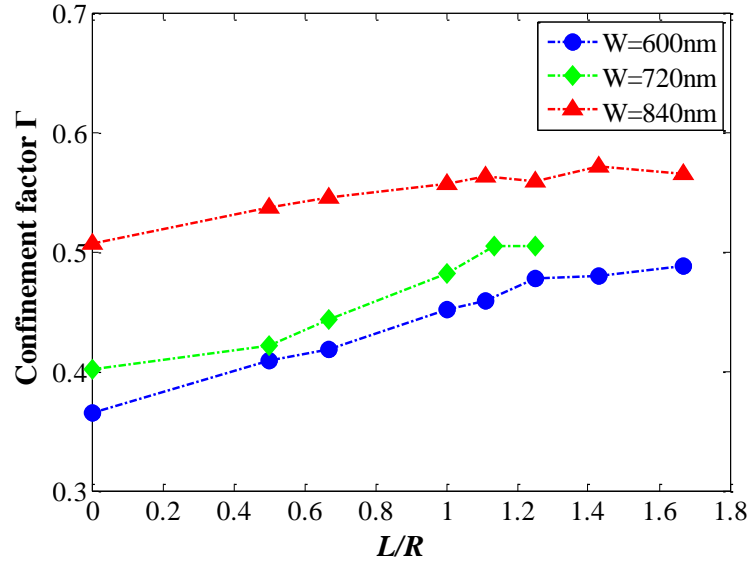
Figure 4.5 Confinement factors Γ of a capsule-shaped metallic laser for the plasmonic mode, as a function of mirror curvature R ($L = 1100$ nm. Other parameters are written in the text.). Note that for the case of $W = 720$ nm (the green curve), there is no information of confinement factor Γ, because two different modes overlap at a same resonant wavelength when $R < 0.7L$, and we could not extract the accurate field distribution of TE mode in these regimes to calculate Γ.

The direct results from 3D-FDTD simulation of capsule-shaped metallic semiconductor cavities are discussed up to now, and can reveal the effectiveness of the Q factor improvement property of the proposed new structure. In the following section, the 3D-FDTD results will be taken into the calculation of threshold gain and threshold current.

4.3 Threshold gain and threshold current

In Chapter 3, the threshold gain g_{th} has been derived from the rate equation and written in Eq. (3.4). It is inversely proportional to the cavity Q factor, group velocity

v_g and the confinement factor Γ, so that the threshold gain g_{th} should be reduced if both Q and Γ are increased. Since we ignore the material dispersion for simplicity in the 3D-FDTD simulation, we assume the group refractive index of the InGaAs layer to be 3.53 to calculate v_g to keep consistent with the simulation.
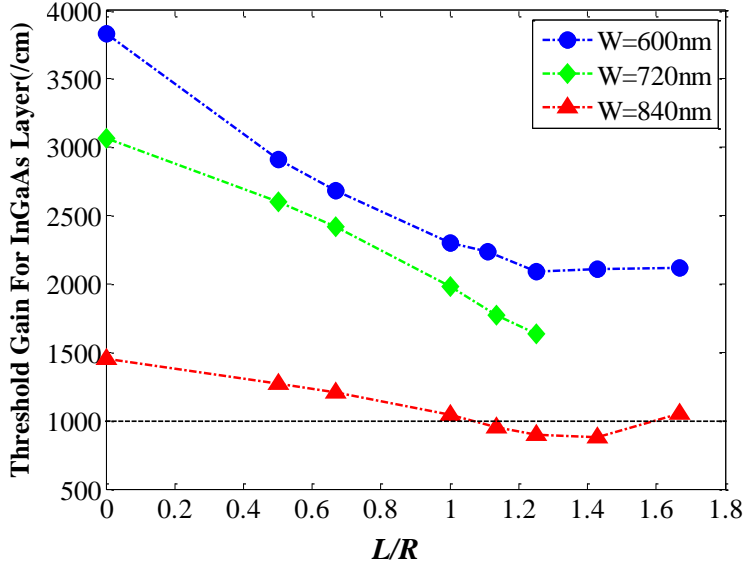

Figure 4.6 Threshold gain required at the InGaAs layer of a capsule-shaped metallic laser for the plasmonic mode, as a function of the mirror curvature R. (L = 1100 nm. Other parameters are given in the text.)

Figure 4.6 depicts the threshold gain g_{th} required at the active InGaAs layer, calculated by using Eq. (3.4) for the TE mode as a function of mirror curvature R [90]. By introducing the curved mirrors, both the Q factor and the confinement factor Γ get improvement (shown in Fig. 4.2 and Fig. 4.5), thus the threshold gain decreases significantly. For example, in the case of W = 840 nm, the threshold gain can be reduced below 1000 cm-1 when 1<L/R<1.6, which value is achievable for high gain materials such as InGaAs [87].

By using the derived threshold gain g_{th} and the conventional theory on semiconductor lasers based on the rate equations, we can estimate the threshold current I_{th} by Eq. (3.8). The material parameters are also given in Table 4.2 [90], which is derived from the reported parameters for the bulk InGaAs crystal, lattice-matched to InP [90], [93], [94].

Before taking rigorous calculation, an intuitive understand of the effect of capsule-shaped cavity on the threshold current can be examined. As shown in the text above, the curved mirrors can increase Q and Γ, which results in significant decrease of g_{th}. On the other hand, the volume of the active layer V is reduced by cutting a rectangular cavity into a capsule-shaped one, which is obvious from Fig. 4.1. Both factors contribute to the reduction of I_{th}.

Table 4.2 Material parameters of bulk InGaAs crystal, lattice matched to InP, used in estimating the current threshold.

Variable	Definition	Value	Unit	Ref.
B	Bimolecular recombination coefficient	1.0×10^{-10}	cm^3/s	[94]
C	Auger recombination coefficient	4.15×10^{-29}	cm^6/s	[93]
η_i	Current injection coefficient	1	-	-
N_{tr}	Transparency carrier density	1.1×10^{18}	cm^{-3}	[87]
g_{oN}	Empirical coefficient	1000	cm^{-1}	[87]

Figure 4.7 shows the calculated I_{th} as a function of L/R [90]. For all values of cavity width, current threshold I_{th} is reduced exponentially by introducing the curved mirror. In the case of $W = 840$ nm, for example, the I_{th} can be reduced from 291 µA ($L/R = 0$) to 60 µA when $L/R = 1.43$.

The I_{th} dependence on the cavity width (rigorously speaking, dependence on

the active volume) is more sensitive for the conventional rectangular cavities. For example, the rectangular cavity with $W = 840$ nm requires a threshold current of 291 µA, which is 2-orders smaller than that for $W = 720$ nm (22.7 mA), and 3-orders smaller than that for $W = 640$ nm (178.0 mA).
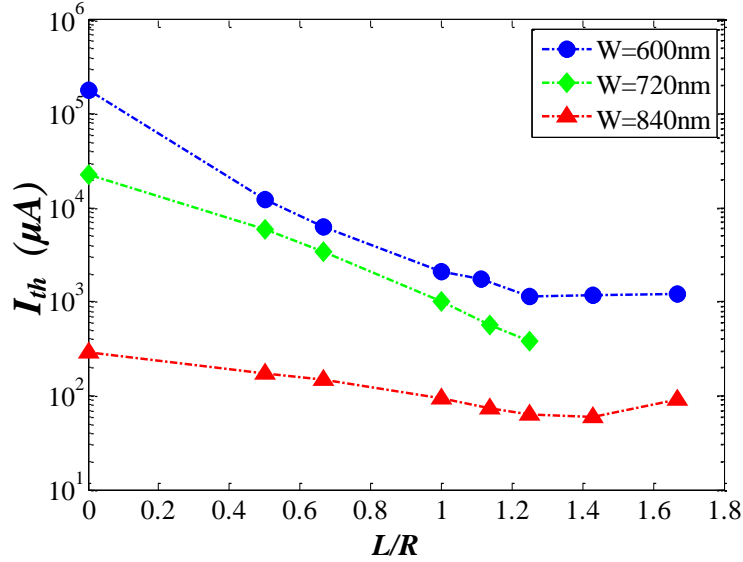

Figure 4.7 Threshold current of a capsule-shaped metallic laser for TE mode, as a function of the mirror curvature R. ($L = 1100$ nm. Other parameters are given in the text.)

It is in line with the cavity width dependence of propagation loss, which is estimated by waveguide analysis [62]. This is one reason why TE mode is increasingly difficult to achieve lasing when shrinking the laser size using the conventional rectangular cavity. As a result, a latest effort on rectangular metallic cavity only achieved TM mode but TE mode (Note that the nomination of TE or TM mode in Ref. 66 is opposite to that in this dissertation. In this dissertation, the definition of TE and TM modes follows the researches of conventional semiconductor lasers, and all the modes in the text obey to this rule.) [66]. However, by introducing capsule-shaped cavity, the threshold current of the TE mode can be dramatically reduced, and thus lasing TE mode with many benefits for PICs

becomes achievable.

Another natural issue is how high Q value is sufficient for a FP cavity-based metallic laser, especially by introducing capsule-shaped structure? In other words, if further improvement of Q factors is necessary and worthy to be achieved? To investigate this issue, a series of cavities with the same dimensions of 1.1 μm by 0.84 μm is taken into the calculation, with an assumption that the Q values vary from 50 to 1000. Then the threshold current as a function of Q factors can be studied, which is shown in Figure 4.8.

From Fig. 4.8, it shows that when the Q factor is smaller than 250, the threshold current can be reduced exponentially as the Q factor increases. However, when the Q factor becomes larger than 250, the threshold current will be reduced slowly as the Q factor goes on to increase. In other words, a-few-hundreds Q-factor is enough for sub-wavelength metallic cavity with about 1 μm by 1 μm dimensions.

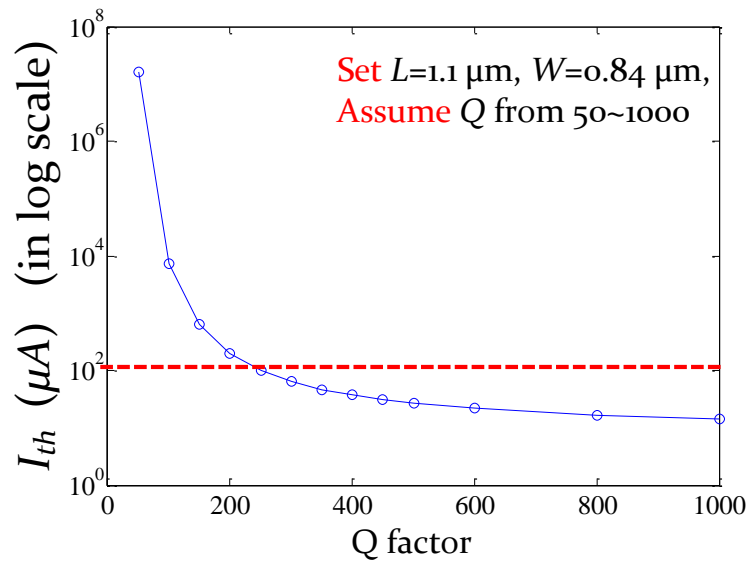Figure 4.8 Threshold current of a capsule-shaped metallic cavity with 1.1 μm by 0.84 μm dimensions, as a function of Q factor.

It also should be mentioned that lambda-scale lasers with well designed cavities can achieve the low threshold current of a few tens μA with Q factors of a few hundreds, which is discussed in the research of LEAP laser [51]. From this point of view, relatively low Q factors of our capsule-shaped metallic lasers can be practical by optimizing the cavity structure and parameters. And we theoretically demonstrate in this paper that an optimized capsule-shaped cavity with Q factor of 297, which has the effective modal volume of 0.45 μm^3 and footprint of 1.1×0.84 μm^2, can achieve the threshold current as low as 60 μA.

4.4 Size shrinking effect of capsule-shaped metallic semiconductor laser

From the point of view that the large scale PICs requires light source with ultra-small footprint and low energy cost, metallic semiconductor lasers should be designed as small as possible. However, from the previous discussion in Section 4.3, it is concluded that a smaller cavity can generally increase the threshold gain, which may increase the threshold current. As the factors of small volume and low cost compete with each other, there should exist a limit of shrinking the laser size.

In order to examine the relationship between laser size and threshold current, series of cavities with different volumes are investigated. Figure 4.9 depicts the threshold current I_{th} as a function of the width of the capsule-shaped cavities. For all the cases, the cavity length L is fixed to 1100 nm, and the mirror curvature is fixed to $L/R = 1.25$ (red curve) and $L/R = 0$ (blue curve).

From Fig. 4.9, firstly, it reveals that for all values of the width, the capsule-shaped cavities (red curve) always have smaller threshold current than that of the rectangular ones (blue curve), which demonstrates the advantage of capsule-shaped metallic cavity. Secondly, in the range of narrow width ($W < 800$ nm), I_{th} increases with decreasing width, because the effect of increasing g_{th} is exponentially [see in

Eq. (3.8)] and overwhelms the reduction of V which is linearly. On the other hand, in the range of broader width ($W > 800$ nm), I_{th} becomes relatively insensitive to the width, because the decrease of g_{th} compensates the increase of V. As a result, there exists an optimal width of 840 nm for $L/R = 1.25$ (red curve), where I_{th} is reduced to as small as 64 μA.
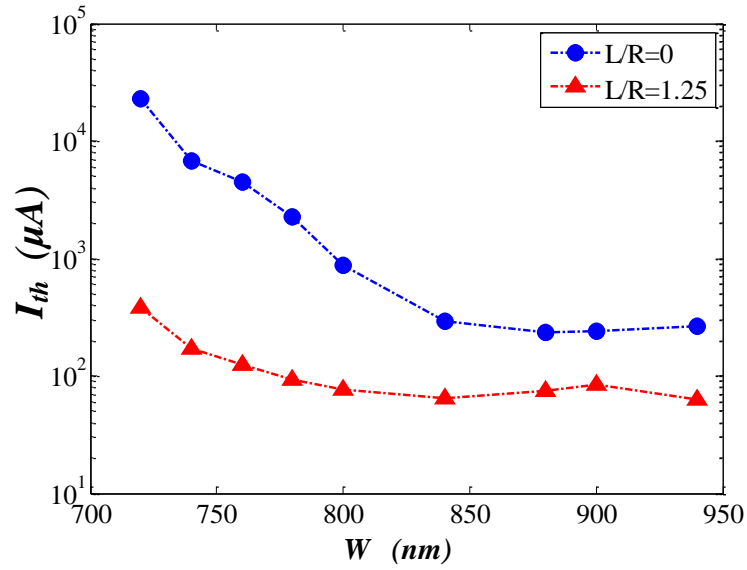

Figure 4.9 Threshold current of a capsule-shaped metallic laser (red curve) and a rectangular metallic laser (blue curve) for the plasmonic mode, as a function of the cavity width W. ($L = 1100$ nm. Other parameters are given in the text.)

Up to now, the idea of designing a capsule-shaped metallic semiconductor cavity laser is to achieve high Q factor and low threshold. In this basis, optimal size exists. However, from another point of view, if some level of Q factor and threshold is acceptable, how small the laser size can go? For example, in Fig. 4.2 (a), a capsule-shaped cavity with 720-nm width has a similar Q value to a rectangular cavity with 840-nm width. In this case, capsule-shaped structure can be utilized to shrink the laser size without sacrifice of the performance.

In order to investigate this size shrinking effect of the capsule-shaped metallic semiconductor lasers further, a series of both rectangular and capsule-shaped cavities with different dimensions are carried out into 3D-FDTD simulation, and the calculated Q, g_{th}, and I_{th} are all listed in Table 4.3 [90].

In Tab. 4.3, there are 3 pairs of different examples to show that the capsule-shaped structure can shrink the laser size effectively, compared to conventional rectangular one. In Case 3, for example, the footprint can be reduced from 0.92×0.80 µm^2 to 0.72×0.64 µm^2 (about 42% reduction) by introducing curved mirrors ($L/R = 1.25$) while keeping the Q factor and the resonant wavelength unchanged. As a result, the threshold current can be reduced to 593 µA.

Table 4.3 Size shrinking effect of capsule-shaped metallic semiconductor cavity lasers.By introducing an optimal curvature, significant size reduction is achieved without changing the Q factor and resonant wavelength.

Case	1		2		3	
L (nm)	1580	1360	1340	1140	920	720
W (nm)	1000	1000	1000	900	800	640
L/R	0	1.25	0	1.25	0	1.25
λ (nm)	1548	1546	1557	1572	1620	1620
Q	285	315	257	259	142	143
g_{th} (cm^{-1})	884	788	1059	1045	2155	2006
I_{th}(µA)	113	72	150	103	1572	593
V_{total}/λ^3	0.60	0.49	0.50	0.34	0.24	0.14
Size reduction	18%		32%		42%	

4.5 External radiation and waveguide coupling scheme

As high loss is caused from metal-clad in types of metallic semiconductor lasers, how efficient the lasing mode can be extracted from the cavity is an important issue. In this section, firstly the external radiation ratio is derived and simulated to estimate the total radiation efficiency. Then a waveguide coupling scheme which extracts the evanescent wave from the cavity substrate is proposed and studied.

The total Q factor plotted in Fig. 4.2 can be regarded as an expression of total cavity loss, which has two different contributions, including the metallic loss and the radiated loss. It can be written as

$$\frac{1}{Q} = \frac{1}{Q_{\mathrm{metal}}} + \frac{1}{Q_{\mathrm{rad}}}, \tag{4.1}$$

where $1/Q_{\mathrm{metal}}$ and $1/Q_{\mathrm{rad}}$ denote the metallic absorption and the external radiation rate, respectively. Extracting sufficient radiated lasing mode is an important issue in practical applications. From Eq. (4.1), the external radiation efficiency can be expressed as

$$\eta_{ext} = \frac{Q}{Q_{rad}} \tag{4.2}$$

where η_{ext} is the external radiation efficiency. To investigate η_{ext} quantitatively for various capsule-shaped cavities, 3D-FDTD simulations are repeated for the same structures but without metallic losses, which can be realized easily by just setting the damping coefficient of the Lorentzian model to be zero. In this case, the Q factor derived only from the contribution of the external radiation with the assumption that the modal profile does not vary substantially with and without the metallic losses. Thus, an approximate Q_{rad} of the given cavity structure can be obtained.

Finally, external radiation efficiency η_{ext} can be calculated by Eq. (4.2).

Figure 4.10 depicts η_{ext} of different capsule-shaped cavities as a function of L/R for various values of cavity width [90]. Firstly, it shows that the cavities with wider width have lower external radiation efficiency, which is consistent with the general trend that the wider width increases the confinement factor Γ as shown in Fig. 4.5. Besides, Fig. 4.10 also shows that η_{ext} is relatively insensitive to the mirror curvature (L/R). As a mirror with curvature of R is introduced to the rectangular cavity, the metallic loss is reduced, which can contribute to an increase of η_{ext}. On the other hand, however, confinement factor Γ is also enhanced, which donates to a decrease of the external radiation rate. As a result, these two factors compensated for each other and η_{ext} behaves insensitively to the curvature of R. Thus, depending on the applications (whether you need to minimize the threshold current or maximize the laser output power), there exists an optimal design for the cavity width and L/R.
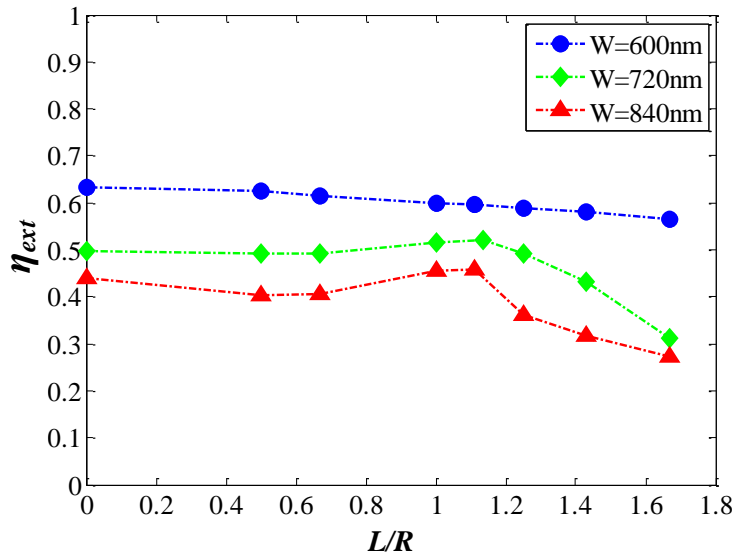

Figure 4.10 External radiation efficiency of a capsule-shaped metallic laser for the TE mode, as a function of the mirror curvature R. ($L = 1100$ nm. Other parameters are given in the text.)

From Fig. 4.10, it is important to point out that high η_{ext} ranging from 40 to 60% can be achieved reasonably in all cases calculated in the simulation. This indicates that although the high metallic losses have non-negligible effects on the overall performance, it is not the most (if not the least) dominant effect that determines the Q factor. It should also be mentioned that the field is radiated into the bottom InP substrate for the structures considered here, thus the radiated field, in principle, could be coupled into a waveguide structure underneath the metallic cavity.

Some different schemes of waveguide coupling are reported with numerical demonstration [85], [86]. As it is discussed in Chapter 2, for circular metallic lasers, an in-plane-coupling structure is proposed. The circular cavity is capped with metallic top while the sidewall is only bared semiconductor without metallic claddings. In this way, the radiate field from the sidewalls can be coupled into a waveguide placed nearby the cavity. This scheme of waveguide coupling sacrifices the advantage of the tight confinement by an entire metallic clad; and it surfers from practical difficulties in fabrication, as an asymmetric metallic top of the circular semiconductor pillar is assumed for the optimal coupling efficiency of 22% [85]. Considering the poor Q factors of a capsule-shaped cavity without metallic sidewalls, which is plotted in Fig. 4.4, the in-plane-coupling scheme is not suitable for the proposal in this dissertation.

Another scheme of waveguide coupling is collected the radiation from the bottom side of the cavity with entire metallic clad [86]. Unlike the in-plane-coupling, it couples the light radiation vertically from the cavity substrate, which owns the advantages of ease of fabrication and higher coupling efficiency.

Here a structure of waveguide coupling based on the vertical coupling is proposed and taken into 3D-FDTD simulation, to make an intuitive perspective. Figure 4.11 shows the schematic of waveguide coupling design of capsule-shaped metallic semiconductor lasers. A waveguide of InGaAsP core with InP clads is

located underneath the metallic cavity, which can extract the external radiation of the cavity from the bottom side.
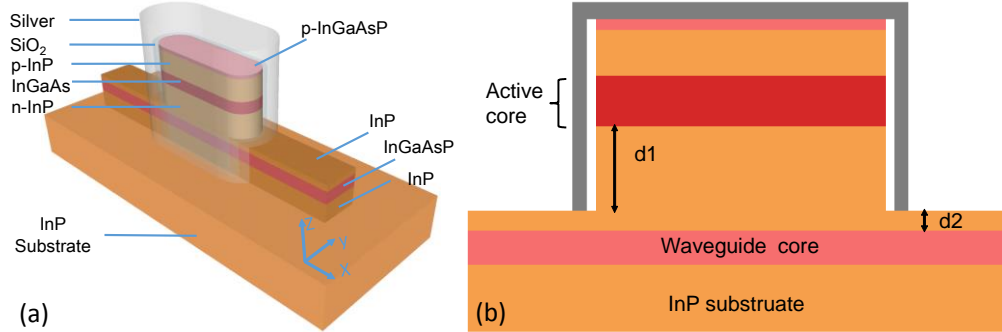

Figure 4.11 Schematic of waveguide coupling design. (a) 3D view; (b) cross-section plane along the wave-propagation direction. The active core of the metallic cavity can be either bulk InGaAs or InGaAs/InGaAsP MQW.

The active core of the metallic cavity can be either bulk InGaAs or InGaAs/InGaAsP MQW. Here a bulk-InGaAs active layer is used in the simulation for example, and the length and width of the cavity are 1600 nm and 1000 nm respectively, while the thickness of the waveguide core is 350 nm. As the similar structure of metallic semiconductor modulator is designed in our lab [95], here a similar set of parameters of that work is directly applied to the structure in Fig. 4.11 for simplicity, with d1 = 350 nm and d2 = 100nm. The waveguide-coupling efficiency is defined as the ratio of $\gamma_{waveguide}/\gamma_{rad}$, where the $\gamma_{waveguide}$ and γ_{rad} respectively represent the cavity-to-waveguide coupling rate and the total cavity radiation rate [86]. The γ_{rad} is calculated by integrating the ponyting vector in an enclosed plane that includes all the simulated structure. For a conservative estimation, the $\gamma_{waveguide}$ is derived from integrating the poynting vector within the waveguide-core (InGaAsP) region in the cross-section plane (part of the enclosed plane) that is perpendicular to light propagation direction. The estimated

waveguide-coupling efficiency is about 38.7%, and the electrical field distributions in three cross-section planes are shown in Figure 4.12.
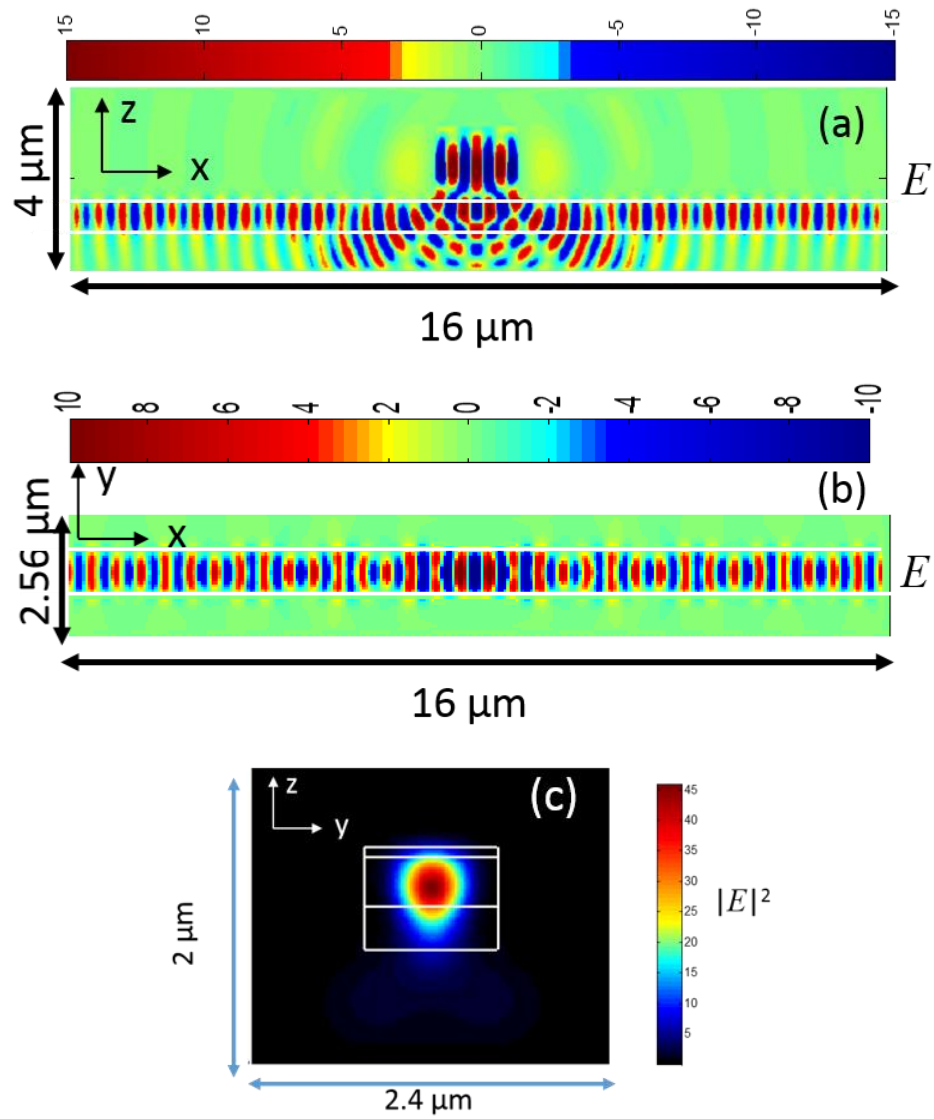

Figure 4.12 Electrical field distributions in three cross-section planes of xz-plane crossing the center of the cavity (a), xy-plane crossing the center of the waveguide (b) and yz-plane that is perpendicular to the light-propagation direction (c). White lines show the position of the waveguide structure.

Here the vertical waveguide-coupling scheme is proposed and numerically investigated, while more efforts on the optimizing this vertical coupling scheme for higher coupling efficiency can be done in future work. For instance, the substrate of the waveguide can be coated with lower-index layer such as SiO_2 to reduce the radiation loss. Besides, the optimization of parameters d1 and d2, which is sensitive to cavity Q factor, can also improve the coupling efficiency. Further, asymmetric lengths in two directions of the waveguide can be designed to couple the cavity mode into one definite direction, which is more efficient for applications in PICs.

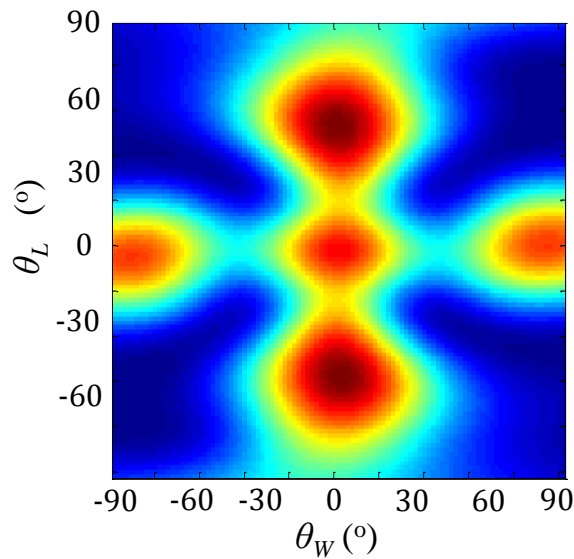# 4.6 Far-field radiation of capsule-shaped metallic semiconductor laser

Figure 4.13 Far-field pattern of capsule-shaped metallic semiconductor cavity. (L = 1100 nm, W = 840 nm, L/R = 1.25, other parameters are the same as the cavity shown in Fig. 4.1)

By the NFFT that is derived in Chapter 3, the far-field pattern of radiation from the capsule-shaped cavity can be obtained, which is illustrated in Figure 4.13. For simplicity and consistence with other simulation results in this chapter, the topology of this cavity is the same as those in Fig. 4.1, while $L = 1100$ nm, $W = 840$ nm and $L/R = 1.25$. From Fig. 4.13, it shows that the main patterns with the highest intensity in the far field pattern exist around $\theta=60^{\circ}$, which is beyond the light cone of an objective lens with a numerical aperture (NA) lower than 0.86. However, a moderate field at $\theta=0^{\circ}$, $\varphi=0^{\circ}$ can still be collected into the photon detector, by an objective lens with a low numerical aperture. This will be dealt with in detail in following chapters.

4.7 Summary

In this Chapter, a systematically numerical calculation of proposed capsule-shaped metallic semiconductor cavity laser is carried out by 3D-FDTD simulation. Firstly, the cavity Q factor is calculated and shows above 50% improvement by introducing curved mirror with optimal curvature of R. The electrical field distribution inside the capsule-shaped cavity exhibits a Gaussian-like mode profile with reduced overlap at the metallic sidewalls, which intuitively explains the reason why the capsule-shaped structure can reduce loss and improve Q value effectively. Then the confinement factor is also estimated and shows increase by capsule-shaped design, which is consistent with the results of Q value and mode pattern.

Secondly, by substituting the known Q value and confinement factor into the derived rate equation in Chapter 3, the threshold gain and threshold current of capsule-shaped cavity are calculated as well. Capsule-shaped design can lower down both the threshold values dramatically.

Thirdly, the external ratio efficiency is investigated and about 40-60% light field can be radiated from the cavity, according to the simulation. Then a scheme of

waveguide coupling under the cavity substrate is proposed and taken into calculation. About 38.7% coupling efficiency is achieved for optimal case, and shows potential applications in PICs. Besides, far field of the radiation is also studied to give a guidance for collection and measurement of the lasing mode.

In short, the advantage and effectiveness of capsule-shaped cavity for metallic semiconductor lasers are numerically demonstrated in this chapter. Following works will concentrate on the experimental investigation of this proposal.

Chapter 5

Fabrication of capsule-shaped metallic semiconductor laser

5.1 Introduction

Fabrication Technologies of semiconductor devices have been developed for decades with the growing demands for more complex and higher-capacity large-scale integration (LSI), in both Si-based and compound semiconductor applications. As the rise of various plasmonic-based devices with metals, the fabrication technique is processed in deep sub-wavelength scale to achieve ultra-small devices. On the other hand, as the compound semiconductors, for example, InP-based materials, are suitable for building lasers because of the direct bandgap, thus plasmonic or metallic III-V lasers which aim at ultra-compact and low-energy consumption light source in PICs are developed prosperously in recent years. Due to the ultra-small dimension of such metallic semiconductor lasers, it is a great challenge to fabrication technology [82].

In this chapter, the proposed capsule-shaped metallic InGaAs/InP cavity lasers are fabricated for the first time. There are mainly 3 steps as a standard procedure of device fabrication: depositing, patterning and etching. Some difficulties and imperfections are suffered during the process such as the property of Ag deposition, device profile after dry etching, contamination of patterning mask and *etc*. All these important issues will be discussed in details in following sections, and get improved by some procedures.

5.2 Fabrication process flow

The schematic of fabrication process flow of capsule-shaped metallic semiconductor cavity (similar structure in Figure 4.1) is briefly shown in Figure 5.1. As the objective of this dissertation is to demonstrate the proof of concept of the capsule-shaped structure, fabrication for PL measurement is designed for simplicity. The whole process is started from an epitaxial wafer with an active layer of InGaAs,

which is cladded by InP, shown in Fig. 5.1 (a). The wafers used in fabrication and measurement in this work are grown by the metalorganic vapor-phase epitaxy (MOVPE) technology, and are ordered from LandMark Optoelectronics Corporation (LMOC). The parameters of each layers in the epitaxial wafers are listed in Tables 5.1 (with active layer of bulk InGaAs) and 5.2 (with active layer of InGaAs/InGaAsP MQW).
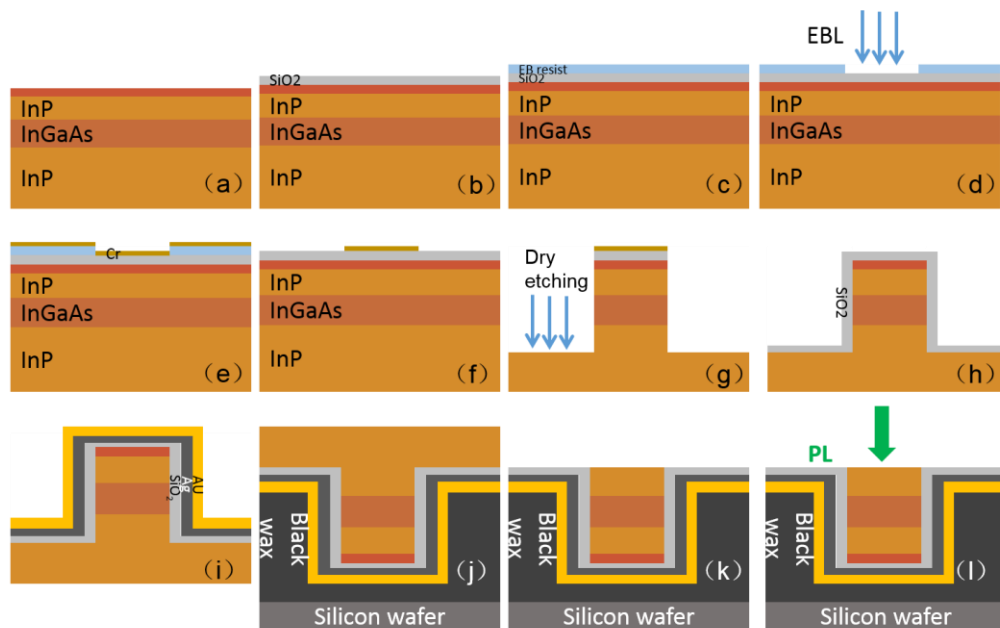

Figure 5.1 Schematic of fabrication process flow of capsule-shaped metallic semiconductor cavity.

As shown in Fig. 5.1, the brief fabrication process flow is as following:

a) Crystal growth by MOVPE, which is done by LMOC.

b) Deposition or sputtering of silicon oxide. Here SiO$_2$, which is used as a mask for dry etching, is deposited or sputtered on the top of wafer firstly. During

sputtering, plasma is induced by radio-frequency (RF) voltage to generate high-energy molecules of SiO_2, which is sputtered and deposited on the surface of the wafer. As damage may be caused by the plasma of sputtering, it is not best choice for deposition of the etching mask. Another method to deposit SiO_2 is plasma-enhanced chemical vapor deposition (PEVCD). By introducing SiH_4 and O_2 on the surface of a substrate, the Si and O radicals react each other and produce SiO_2 film. The quality of SiO_2 formed by PECVD is preferable to that deposited by sputtering in this process.

c-d)   Spin coating resist and patterning the wafer by electron beam lithography (EBL). Here, resist "ZEP 520-A" is used and a 3-min pre-baking is also dealt with. High voltage (50kV) is applied for fine resolution of EBL as the objective pattern is quite small in the range of ~μm or even ~100nm.

e-f)   Chromium deposition and EB resist lift-off. In order to protect the EBL pattern, Cr is deposited on the top of the wafer by electron beam (EB) evaporator. High voltage is applied to the target of Cr and makes it melt and form plasma. Then the Cr gas evaporates and gets solidified on the surface of the wafer to form a thin film. After lift-off process of EB resist by ZED MAC, capsule-shaped patterns of Cr are realized.

g)   Dry etching of SiO_2 with Cr mask, and of InGaAs/ InP with SiO_2 mask. Using CHF_3/Ar (5:5) to dry etch SiO_2 layer is well controlled and shows straight and smooth etching profile. However, dry etching for InGaAs/ InP multi-layer structure meets difficulty and imperfection. A basic issue is the balance of vertical profile and roughness of the etching surface. During this process, both chemical and physical etching exist, lead to anisotropic or isotropic profile respectively. Anisotropic profile is crucial for making a good waveguide and cavity, although it can introduce some roughness of the device surface. The trade-off of profile and

roughness is the main issue during this process, and two schemes of dry etching by Cl_2/Ar and CH_4/H_2 are investigated in this research, which will be discussed in detail latter.

h) Deposition of SiO_2 as an insulator layer. To deposit SiO_2 uniformly to the sidewalls and the top of the mesas, atomic layer deposition (ALD) is applied in this process and achieve high-quality insulator layer.

i) Deposition silver and gold by EB evaporation. Ag is used as the metallic clad for the capsule-shaped cavity, while Au is applied as a protecting layer for Ag. Due to the nature of EB evaporator in our lab, the holder for the samples cannot rotate horizontally during evaporating, there exists some leakage of after Ag deposition and drop off occurs. To solve this problem, some improvement is done to fabricate an entire Ag clad without blind angle, which will be detailed discussed in following section.

j) Bonding to silicon wafer. After thermal annealing, the fabricated chip is flipped over and then bonded to a silicon wafer by black wax and BCB. As the evanescent field of the resonant mode is radiated from the InP substrate, this step is helpful to an easy measurement of the fabricated samples. During bonding process, making it as flat as possible.

k) Removing the InP substrate by wet etching with hydrochloric acid. InP substrate is etched by HCl solution until etch-stop layer of InGaAsP.

l) Ready to be measured.

Table 5.1 Parameters of each layers of epitaxial wafer (active layer of bulk-InGaAs) ordered from LMOC.

Definition	Material	Thickness (nm)	Doping (cm^{-3})
P-contact	P-InGaAs	100	>1×10^{19} P
Upper cladding	P-InP	600	5×10^{17} P
Etch stop	U-InGaAsP	8	
Upper buffer	U-InP	50	
Core	U-InGaAs	350	
Lower buffer	U-InP	50	
Lower cladding	N-InP	700	5×10^{17} N
Etch stop	N-InGaAsP	8	5×10^{17} N
Lower cladding	N-InP	250	1×10^{18} N
N-contact	N-InGaAsP	100	>5×10^{18} N
Buffer	N-InP	300	>5×10^{18} N
Substrate	InP		

Table 5.2 Parameters of each layers of epitaxial wafer (active layer of InGaAs/InGaAsP MQW with band gap for 1550-nm wavelength) ordered from LMOC.

Definition	Material	Thickness (nm)	Doping	Refractive index
P-contact	P-InGaAs	100	>1 × 10^{19} P	3.6
Upper	P-InP	600	5 × 10^{17} P	3.17
Etch stop	U-InGaAsP	8		
Upper buffer	U-InP	50		
SCH	U-InGaAsP	100		
MQW layer	6 × u-InGaAs (well) 5 × u-InGaAsP (barrier)	6 × 15nm (well) 5 × 12nm (barrier) 150nm		3.53
SCH	U-InGaAsP	100		
Lower buffer	U-InP	50		
Lower	N-InP	700	5 × 10^{17} N	
Etch stop	N-InGaAsP	8	5 × 10^{17} N	
Lower	N-InP	250	1 × 10^{18} N	
N-contact	N-InGaAsP	100	>5 × 10^{18} N	
Buffer	N-InP	100	>5 × 10^{18} N	
Substrate	SI-InP			

Statuses during or after some important processes are shown in Figure 5.2. From next sections to the end of this chapter, imperfections of the fabrication will be discussed and some improvement is obtained.
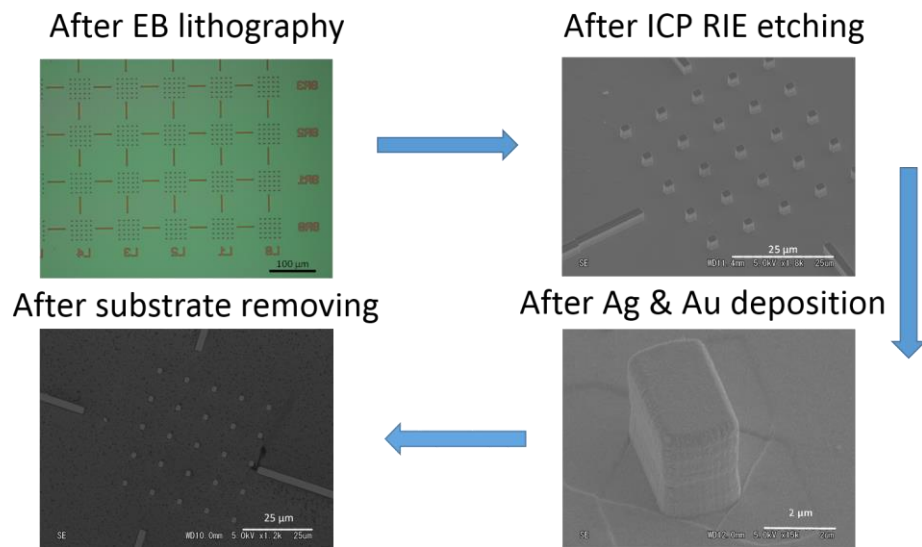

Figure 5.2 Statuses of fabrication after some important processes.

5.3 Difficulty and improvement of dry etching

5.3.1 Basic knowledge of dry etching in this research

In this research, devices are fabricated by dry etching to build a cavity structure. Unlike wet etching that is processed in solutions, dry etching process is using ions, molecules and radicals produced by plasma in gas-phase and in low pressure to react with materials, which is called reactive-ion etching (RIE). The basic setup of RIE is setting two plate electrodes face to face in a vacuum chamber and using RF between them to form oscillated ions and radicals. RF power, pressure, temperature, gas flow, and *etc.*, depend on the concrete materials and process. This technique is known as charge-coupled plasma (CCP), and regarded as a normal one of RIE.

Another technique used in RIE is inductively coupled plasma (ICP), which applies an extra RF source power to control the attraction of ions independently. Higher plasma density can be achieved by ICP for the same source power and thus better anisotropy can be obtained. Figure 5.3 shows a basic schematic of the RIE process.
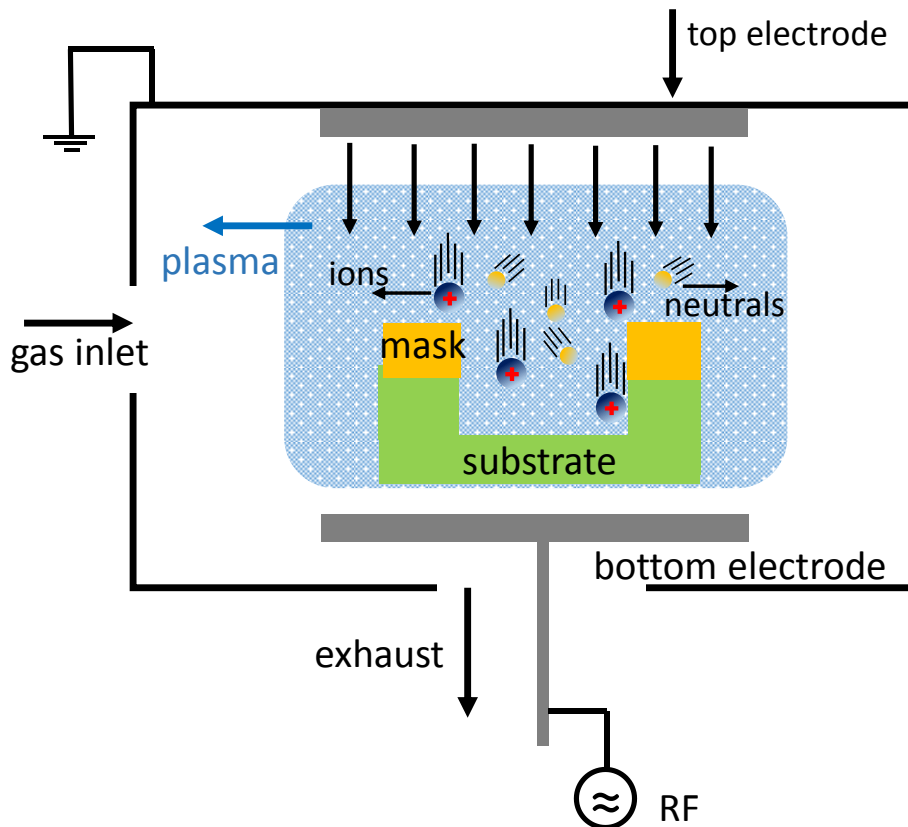

Figure 5.3 A basic schematic of RIE.

During RIE, ions and radicals participates in the reaction with the semiconductor materials, and both isotropic and anisotropic process exist. Isotropic etching means the same shape in all the crystal orientations and usually forms spherical sidewalls, which is regarded as the imperfection of devices such as waveguides and cavities. While anisotropic etching results in vertical sidewalls without horizontal etching. The former one is more chemical process while the

latter one is more physical effect during dry etching. Figure 5.4 shows the schematic of isotropic and anisotropic etching [96].
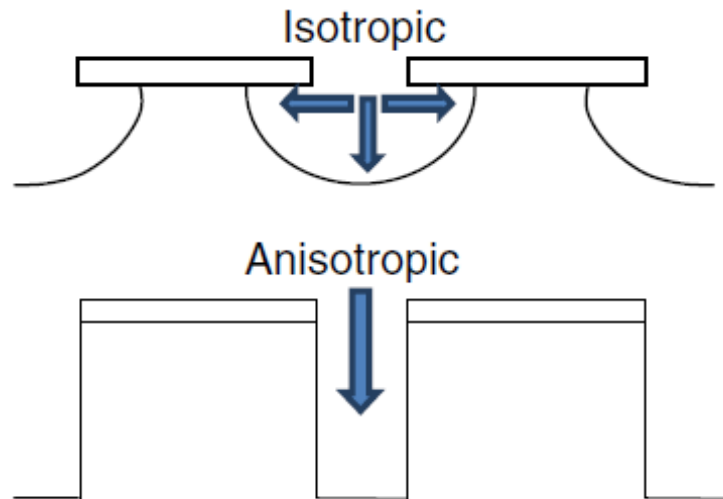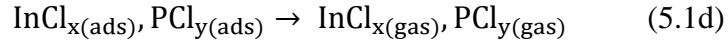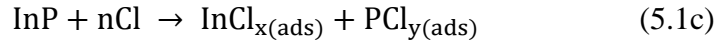

Figure 5.4 Schematic of isotropic and anisotropic etching [96].

For dry etching of InP-based materials, there exist two main methods: halogen-free chemistry of CH_4/H_2 and Cl_2-based chemistry. Both of them are tried in this research and etching conditions are optimized for good fabrication quality, which will be discussed in next sections respectively.

5.3.2 Cl₂-based dry etching

InP dry etching by Cl_2-based chemistry can be divided into following process [97]; generation of ion and electron [Eq. (5.1a)], generation of etchant [Eq. (5.1b)], chemical reaction and ion reaction [Eq. (5.1c)] and product desorption by evaporation [Eq. (5.1d)].

$$e + Cl_2 \rightarrow Cl_2^+ + 2e \qquad (5.1a)$$

$$e + \text{Cl}_2 \;\rightarrow\; e + 2\text{Cl} \tag{5.1b}$$

$$\text{InP} + n\text{Cl} \;\rightarrow\; \text{InCl}_{x(\text{ads})} + \text{PCl}_{y(\text{ads})} \tag{5.1c}$$

$$\text{InCl}_{x(\text{ads})}, \text{PCl}_{y(\text{ads})} \;\rightarrow\; \text{InCl}_{x(\text{gas})}, \text{PCl}_{y(\text{gas})} \tag{5.1d}$$

Many controlling parameters such as temperature, pressure, gas composition, bias power and source power should be taken into account and tested for a good etching. The condition of ICP-RIE machine using Cl_2-based chemistry for InP etching is listed in Table 5.3 [98], by which can achieve straight etching profile with smooth sidewalls. However, multilayer-structure of InGaAs/InP exhibits different property from that of single InP material during dry etching, as the etching rate and characterization are different.

Table 5.3 Etching condition for single InP material

Gas flow (sccm)	Source power /bias power (W)	Pressure (Pa)	Temperature (^oC)	Material
Cl_2/Ar (2:8)	140/110	1.0	220	InP

Figure 5.5 shows the etching results of InP dummy chip and epitaxial chip (see in Tab. 5.1), using the condition in Tab. 5.3. Compared to an InP dummy chip by the same fabrication prosess, undercut and slope angle appear in the etching profile of InP-based multi-layer chip, due to isotropic nature of RIE.

Is the isotropic etching profile critical for the property of proposed capsule-shaped metallic semiconductor laser? To evaluate this impact, simulation of cavities with different slope angles is investigated, shown in Figure 5.6. Here, for simplicity,

the undercut profile is simplified to a slope with an angle and carried out into the numerical calculation.
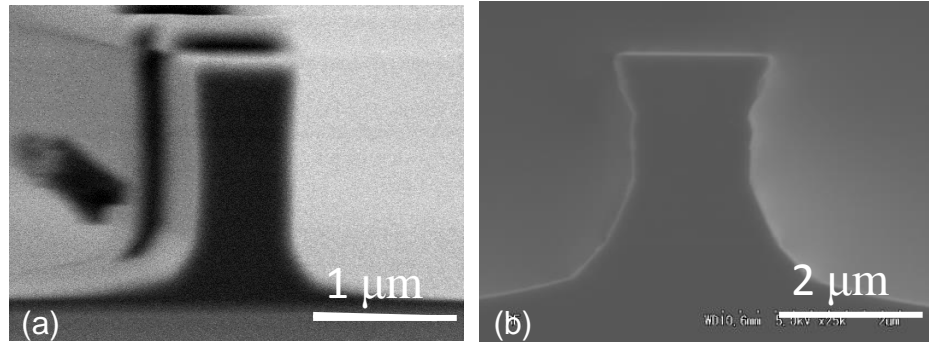

Figure 5.5 Etching profiles of InP dummy chip (a) and InGaAs/InP multi-layer chip, using the condition in Tab. 5.3.
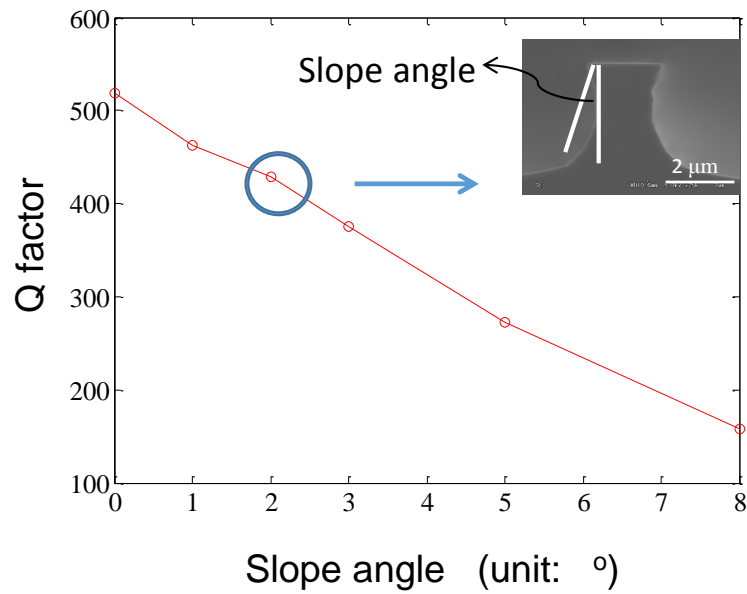

Figure 5.6 Q factors of the capsule-shaped cavity (L/R = 1.25) with 2.5 μm by 1.2 μm dimensions, as a function of slope angle. Insert, the definition of slope angle of the isotropic etching.
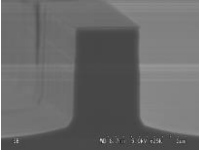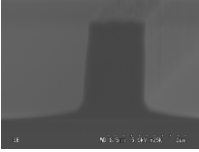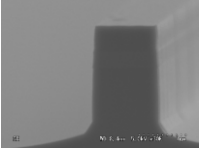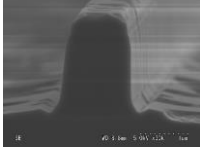
As it is shown in Fig. 5.6, a capsule-shaped FP cavity with a small slope angle can decrease the Q factor dramatically and rapidly, as the sloped mirrors push the resonant mode outside the cavity from the substrate, which is regarded as the radiation loss. Control of the slope angle within 3 degrees is necessary. Thus this isotropy of the RIE should be eliminated and better etching condition is to be improved.

In Cl_2-based chemistry, the role of chlorine radical is to chemically etch the III-V materials, while Ar is added to enhance physical etching and improve the anisotropy [96]. So adjustment of the gas composition is one way to achieve better etching profile. As higher anisotropy is improved by adding the ratio of Ar, more damages to the sample surface is introduced, due to the etching process. To a balance of straight etching profile and roughness, the Cl_2/Ar ratio is modified from 2:8 to 1:9, which is proved to be efficient.

Another effort is to modify the source power and bias power to investigate the effect of ions density on the dry etching. Note that when source power and bias power are increased, the etching rate will also increase and raise the localized temperature quickly at the place where the etching reaction happens. As the machine is not mounted a cooling system and controlling the temperature precisely is not available, any effects resulted from the large changes in temperature cannot be studied in detail. To exclude this issue, both slight changes of source/bias power ratio and gas composition are carried out into the etching conditioning.

According to the condition for InP etching in Tab. 5.3, conditioning of source/bias power ratio is taken into investigation, shown in Table 5.4. It should be mentioned that the wafer used in the conditioning is grown by our own MOVPE with a similar multi-layer structure of InGaAs/InP to that ordered from the company.

Table 5.4 Etching profile of different source/bias power. The Cl_2/Ar ratio is fixed to 1:9, and temperature is setting to 220 ^0C.

Unit (W)		Source power			
		110	140	160	180
B i a s p o w e r	110				
	140				
	160				
	180				
	200				

Basically, increasing power will increase the etching rate and introduce damages to the samples surface. As shown in Tab. 5.4, trenches appear after etching when source power is larger than 140 W, while the sidewall roughness becomes severe when the bias power is larger than 140 W. Besides, changes of bias power

do not bring as sensitive effect as that from changes of source power. Thus, both source power and bias power should be lower than 140 W and the results have similar etching profile which can be acceptable.

Figure 5.7 shows the optimal dry etching profile of epitaxial wafer ordered from land mark, with improved anisotropic sidewall in optimal condition than that in an old condition. Slight isotropy including small undercut and slope still exist after optimization, although has been already minimized. This is due to the nature of our Cl_2-based ICP machine, rather than the scheme of Cl_2-based chemistry itself.
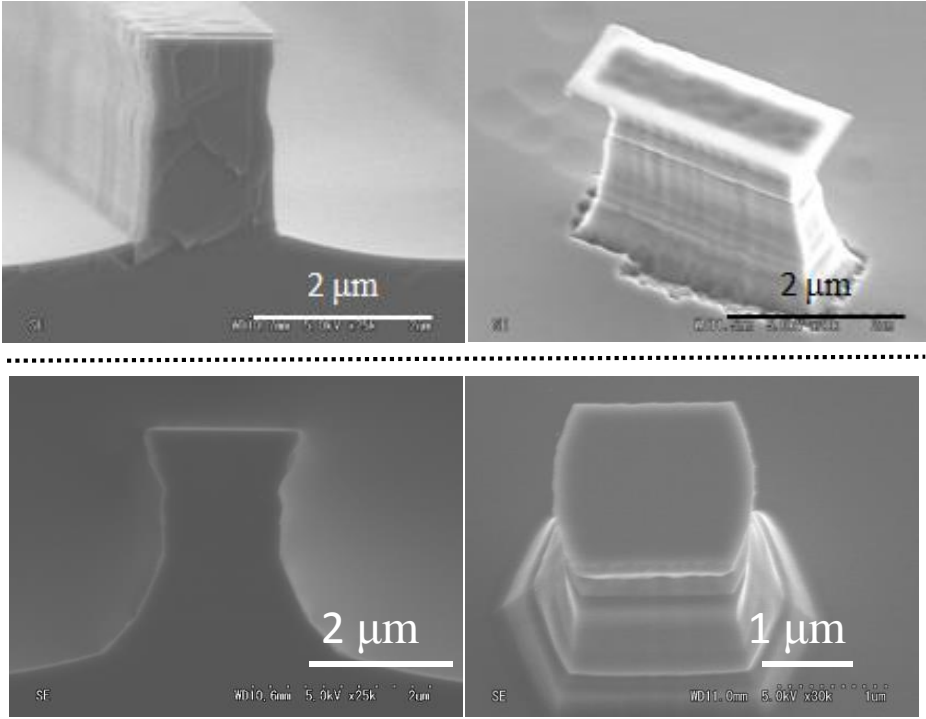

Figure 5.7 Optimal etching profiles of corss-section and 3D view by Cl_2/Ar ratio of 1:9, and source/bias power ratio of 140W:110W at 220 ^0C, in the first row. As a contrast, etching profiles in the second row are the result without optimization (Cl2/Ar ratio of 2:8).

To achieve more straight etching profile and obtain better property, another RIE process of CH_4/H_2 based chemistry is studied and optimized, which will be discussed in next section.

5.3.3 CH_4/H_2-based dry etching

CH_4/H_2-based chemistry is powerful in InP-base material etching, as the advantages of controllable etching depth (low etching rate), low risk (no toxic) and relatively low plasma damage [96], and is applied widely in fabrication of InP/InGaAsP materials and related micro or even nano devices [99]–[102]. The main radicals that react with InP in CH_4/H_2 plasma are CH_3 and H, which can help to generate volatile product in low temperature, as the following reaction [96],

$$CH_3 + H + InP \rightarrow In(CH_3)_3 + PH_3, \qquad (5.2)$$
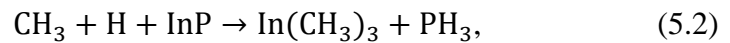
One important issue of this chemistry is that the excessive polymer deposition exists during the etching process and lower the quality of the surface. To overcome this, a cleaning procedure by O_2 plasma is used to control and eliminate the polymer, after some time of the dry etching process. Another drawback of this chemistry is when using ICP, the power should be well controlled into some low level, otherwise the desorption of phosphor atoms becomes faster and leaves behind the indium clusters, which degrades the quality of the sample surface [103]. Thus, in this research, RIE is used for a better and controlled etching quality, with the penalty of relatively lower etching rate.

Table 5.5 Condition of one etching-cleaning cycle of CH_4/ H_2-based RIE.

	H_2 (sccm)	CH_4 (sccm)	O_2 (sccm)	Press. (mTorr)	RIE (W)	Temp. (^oC)	Time (sec.)	DC bias (V)
Etching	48	7	0	15	80	60	300	-439
Cleaning	0	0	50	75	40	60	20	-240

After optimization of the gas composition and source power, the condition of one etching-cleaning cycle for CH_4/ H_2-based RIE is listed in Table 5.5. One –cycle can etch about 75-nm depth of the InP/InGaAs multi-layer material. And etching profile for 3-µm depth is shown in Figure 5.8.
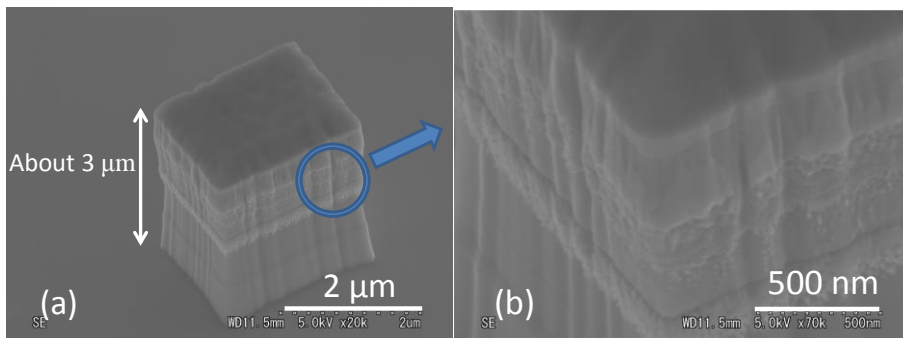

Figure 5.8 Etching profile by CH_4/ H_2-based RIE. (a) a rectangular cavity; (b) the surface of etched sidewall in details, corresponding the marked blue part in (a).

From Fig. 5.8, the overall etching shape is much better and anisotropic than that by Cl_2-based chemistry shown in Fig. 5.7 (Here the mask of sample in Fig. 5.8 is not good enough so that the etching boundary is not as smooth as that in Fig. 5.7, but this point has no sense with etching process itself.). However, obvious polymers and roughness appear after etching process, mainly exist on the top position of the

InP layer rather than the bottom part. As the last part of InP in the bottom (last 2 μm) is smooth with very few polymers, the etching and cleaning condition in Tab. 5.5 is effective; while polymers and roughness in the first part of InP (see in Fig. 5.8(b)) are caused by other issues such as localized temperature on the sample. In this process, after 10 cycles, dry etching is interrupted and N_2 is an inlet to cool down the temperature inside the chamber. And then the RIE is going on. Thus, top InP surfers from higher temperature in some cycles rather than that of bottom counterpart. One solution to this issue is applied a cooling down process after fewer etching-cleaning cycles. A cavity with much better etching profile done by the optimized RIE (cooling down process after 8 etching-cleaning cycles) is shown in Figure 5.9.
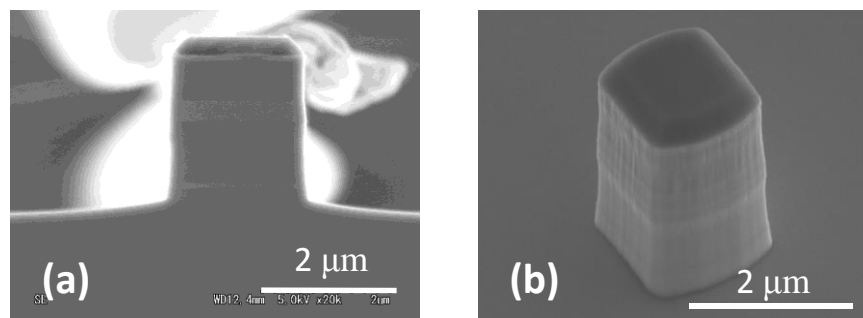

Figure 5.9. Optimal etching profile of a capsule shaped cavity by CH_4/H_2-based RIE. (a) cross-section view. (b) 3D view.

Up to now, two chemistries of dry etching of InGaAs/InP multi-layer structure and optimizations of etching conditions are studied and discussed. Some other improvement of the fabrication process will be in the next section.

5.4 Metal deposition

Metal deposition is another critical process of metallic semiconductor laser. EB evaporator is used to deposit Ag and Au as a metal-clad in the proposed design, where Au is used as a protective layer of Ag. The target (Ag) is heated by EB in high vacuum below 10^{-4} Pa, and is melted into plasma and flies to the substrate upon the target, where a film is formed. As the nature of this process, the evaporated material goes up straight in the vacuum because of the long mean-free path of a few tens of centimeters. Thus only the top of a 3D substrate can be deposited effectively, while the sidewalls are free from evaporation. This feature is schematically illustrated in Figure 5.10, the dashed line shows shadow area where cannot be deposited with target material. Besides, the areas in the plane which is parallel to the deposition orientation is also free of the evaporation, such as the facets A and B in Fig. 5.10.
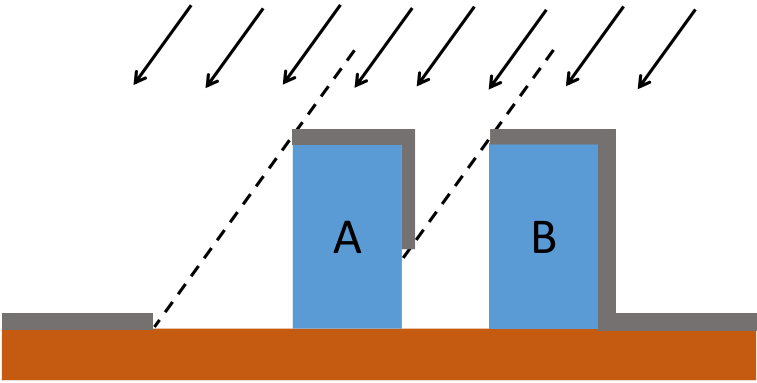

Figure 5.10 Oriental problem of EB evaporation. The arrows indicate the direction of evaporation. And the dashed line shows the shadow area.

To deposit Ag uniformly of a 3D cavity, at least twice evaporation should be done from ±45° angles that can cover all the surface of the cavity. In case that some

facets of the cavity are parallel to the evaporating orientation (see facets A and B in Fig. 5.10), the cavities to be evaporated are all oriented by 45° to avoid this issue. However, in practical cases, the sample can hardly be placed with strict 45° and the evaporation orientation also exists slightly different as designed. Twice evaporation sometimes is not sufficient for a uniform deposition while some blind angles remain to be free of Ag. Thus, an improvement process with 4-times evaporation is introduced, with ±45° angles of both the evaporation orientation and the cavity orientations on the holder.

Figure 5.11 shows the schematic of the orientations in 2 and 4-times evaporations, respectively. The corresponding deposition results are compared in Figure 5.12.
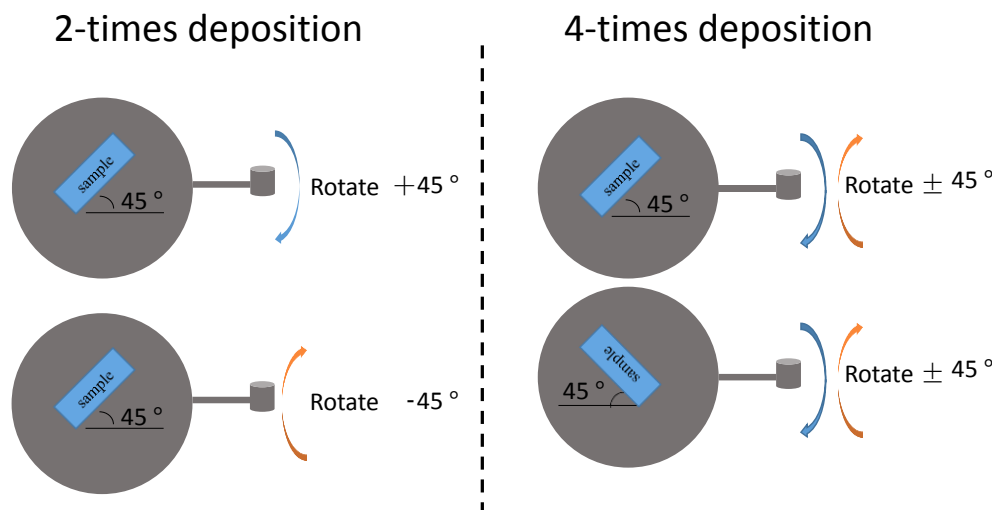
Figure 5.11 Schematic of the orientations in 2 and 4-times evaporations. Each grey area represents the sample holder with a handle to control the evaporation angles, while the blue one represents the sample.

From Fig. 5.12 (a) and (c), the top view of 2 and 4-times evaporation show symmetric shadows after this process. The corresponding 3D views are given in (b) and (d), and show obvious leakage of metal deposition (area marked by red-ring in

(b)) by 2-times method. As a contrast, by 4-times evaporation, the deposition of Ag and Au gets improved and more uniform, without any blind angles, shown in Fig. 5.12 (d).
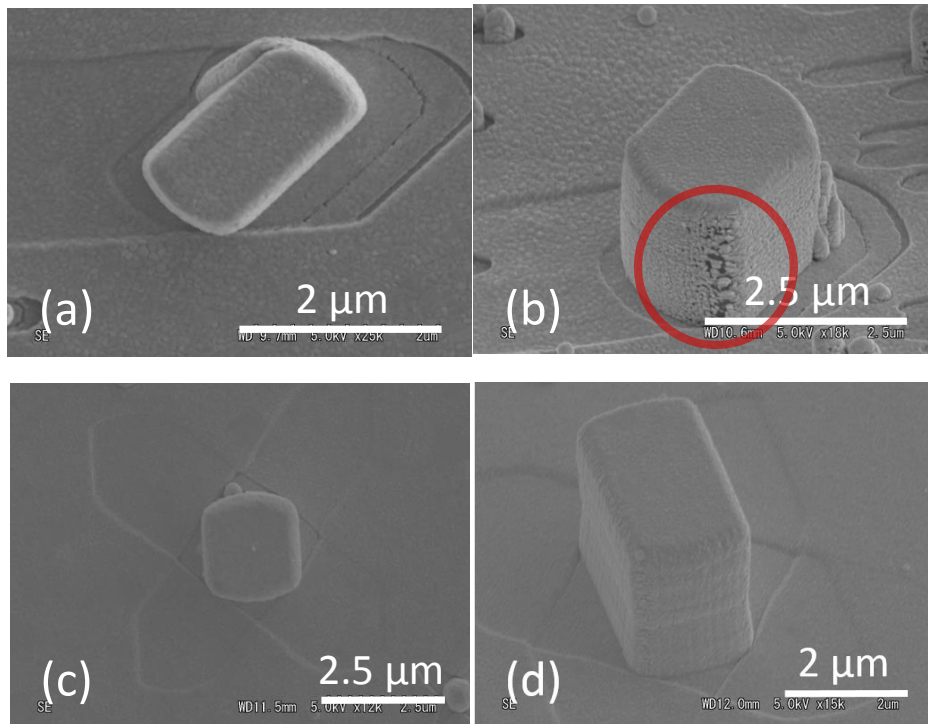

Figure 5.12 Ag and Au deposition results of 2-times (a-b) and 4-times (c-d) evaporation processes respectively. (a) and (c) show the top view while (b) and (d) show the 3D view. The marked area by red-ring in (b) shows the obvious leakage of metal deposition by 2-times method, while it is eliminated by 4-times improved process, shown in (d).

5.5 Issue of Cr mask

As it is discussed in section of process flow, chromium is deposited on the EBL pattern as a mask before SiO_2 dry etching of CHF_3/Ar (5:5) chemistry. Then the SiO_2 remained on the pattern plays the role of mask for InP/InGaAs etching. In Cl_2-based chemistry, Cl_2 also etch chromium as well as InP-based materials. While in

the CH$_4$/H$_2$ chemistry, Cr mask cannot be directly etched but drops into small pieces as contaminations on the surface of the chip, which acts as "masks" of CH$_4$/H$_2$ RIE to etch small pillar-like structures. This contamination caused from remaining Cr does not influence the property of the cavity directly, but can worsen the Ag deposition process once they happen to be so close to the cavities that their evaporation shadows hinder the Ag deposition on cavities. To solve this problem, thinner Cr mask (reducing from 40-nm to 20-nm thickness) is employed in the process, and the amount of Cr contaminations in dry etching process is reduced dramatically and the deposition quality is also improved. Figure 5.13 shows a comparison of cavities fabricated with different thick Cr mask.
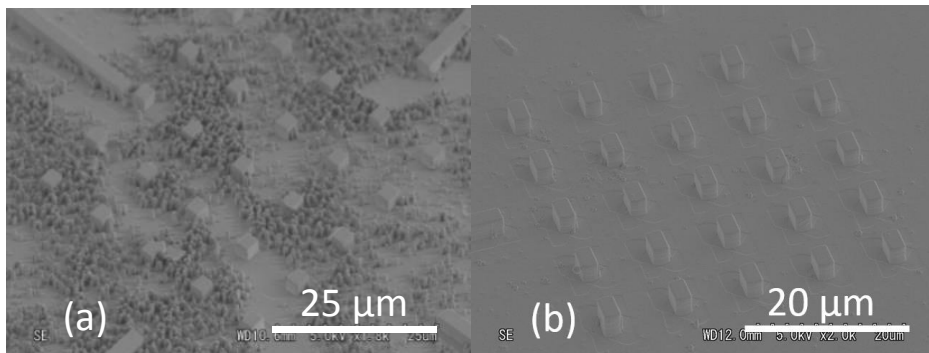
Figure 5.13 Cavities fabricated with different thick Cr mask. (a) 40-nm thick Cr; (b) 20-nm thick Cr.

5.6 Summary

In this chapter, fabrication of proposed capsule-shaped metallic semiconductor cavity is performed for the first time. Process flow and corresponding technique is introduced, and difficulties and problems during some processes are examined in details, especially the etching property and metal-deposition uniformity. To improve the anisotropic dry etching, different etching chemistries are investigated

and various conditions are tested. Due to the nature of machines in our lab, CH_4/H_2-based RIE achieves better etching profile and is optimized for the etching process of capsule-shaped structure. For metal deposition, to eliminate the blind angle during the EB evaporation, 4-times evaporating process is designed and obtains uniform metal-clad outside the semiconductor mesa. Other issue such as contamination caused by Cr mask is also taken into account and get improved.

Chapter 6

Photoluminescence characterization of capsule-shaped metallic semiconductor laser

6.1 Introduction

In this chapter, PL of fabricated capsule-shaped metallic semiconductor cavity is taken into measurement, to demonstrate the proof of concept for the proposed structure.

In following sections, firstly, the setup of PL systems is introduced, as well as the procedures of measurement. Then several PL measurement results are given and analyzed in details, which prove the prediction of numerical simulation in Chapter 4. At last, a brief summary and conclusion are made.

6.2 Setup of PL measurement

Figure 6.1 shows the schematic of PL setup in the measurement of fabricated capsule-shaped metallic semiconductor cavities.
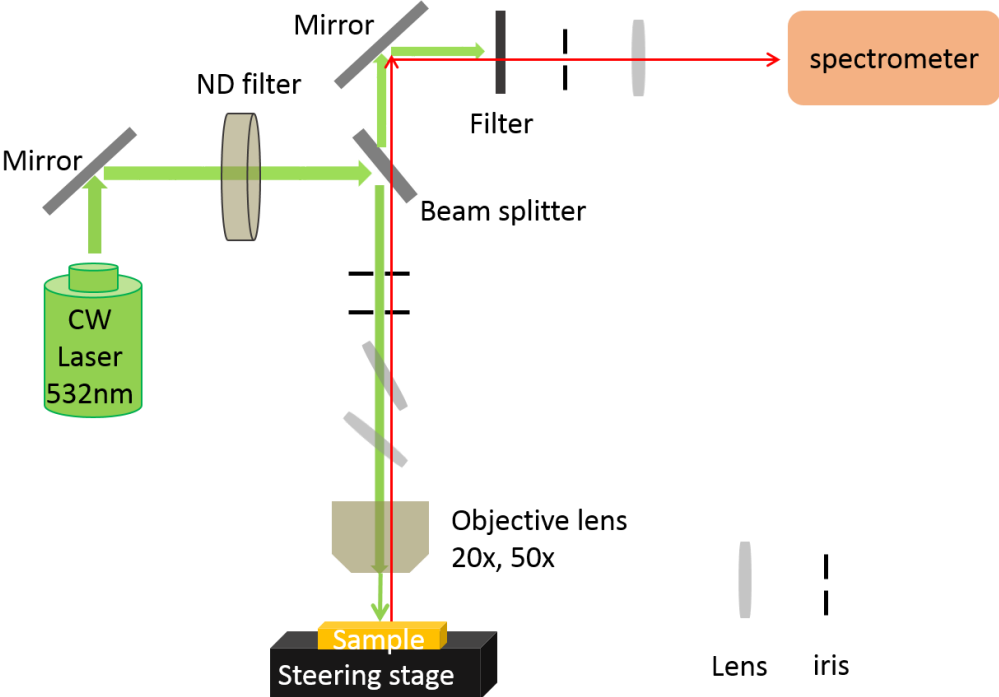

Figure 6.1 Schematic of PL measurement setup.

As shown in Fig. 6.1, the sample is placed on the steering stage, which can move by an electrical mechanism in x, y and z direction independently with a resolution of 0.1 nm. As the cavity dimension is around ~μm, this resolution is good enough for the PL system to focus on each cavity and collect the radiated light field. Light source in this system is a 532-nm continues-wave (CW) laser which stimulates the emission from each cavity. And the spectrum of the emitting field is analyzed by a spectrometer. To eliminate the thermal noise, the CCD camera of the spectrometer is cooled to -100 K.

To measure the emission from a specified cavity correctly and effectively, some necessary steps should be followed, as shown in Figure 6.2:

a)   Find the position of a group of cavities coarsely from the luminescence of cold light. As all these cavities with different dimensions are fabricated in groups with corresponding coordinates and marked bars, and thus can be readily distinguished from the backside of the substrate.

b)   Sweep and capture the position of cavities. To find the exact position of each cavity and measure the spectrum of its emission in further, an area with a group of cavities is swept by steering stage in x and y orientation respectively. To avoid over heating and even destroying the sample, low pumping power is used in this step to stimulate the emitting field and cavity-position maps can be obtained.

c)   Measure the spectrum of the specified cavity. Once the exact position of each cavity is obtained from step (b), the specified cavity can be precisely localized on the focus of the PL system. By modifying the light source power, clear spectrum and LL curve can be measured and analyzed.
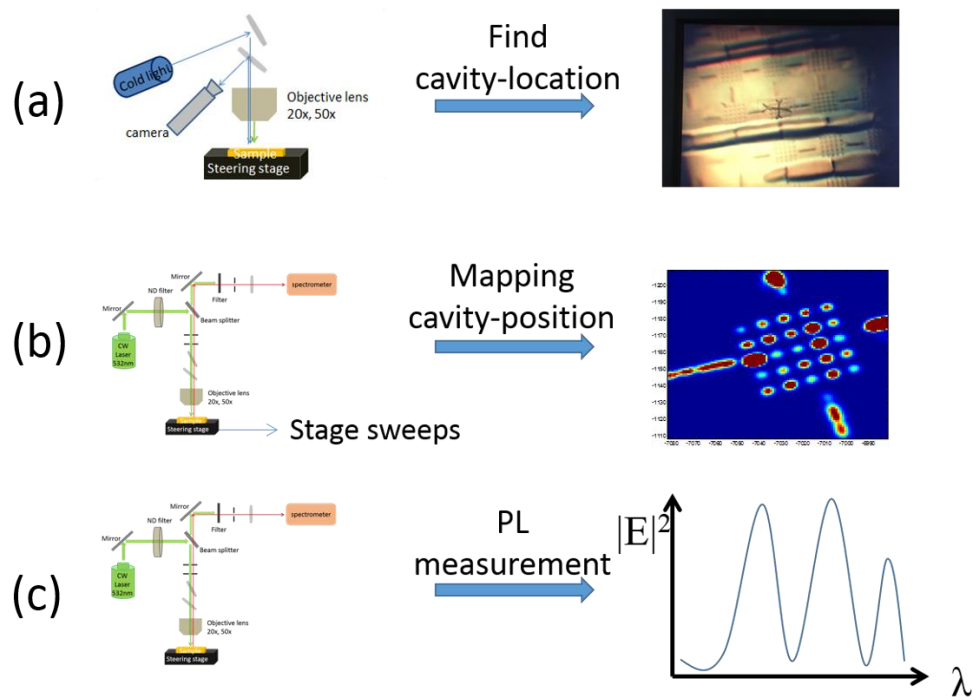
Figure 6.2 Schematic of PL measurement steps.

6.3 PL characterization of capsule-shaped metallic semiconductor cavity

PL characterizations of capsule-shaped and conventional rectangular cavities on the same chip are measured as a comparison, to show the effect of the capsule-shaped structure. Due to the fabrication process, especially the dry etching property, there are three different samples to be PL measured. For simplicity of discussion in following text, all these samples and their properties are listed in Table 6.1. Sample 1 and 2 are dry etched by ICP-RIE of Cl_2-based chemistry, showing undercut and slope properties of etching profile. While Sample 3 is fabricated by RIE of CH_4/H_2-based chemistry, getting much improvement of anisotropic etching profile.

Table 6.1 List of all samples which are taken into PL measurement.

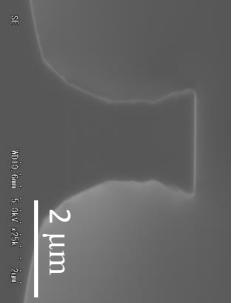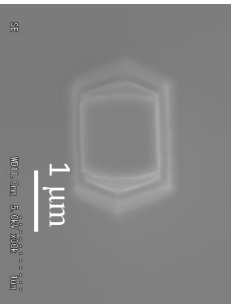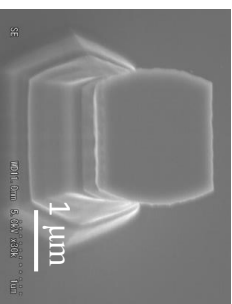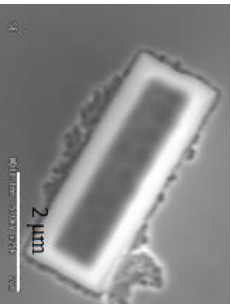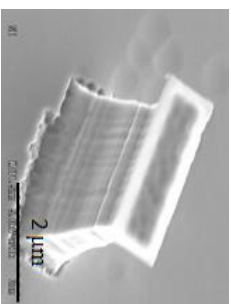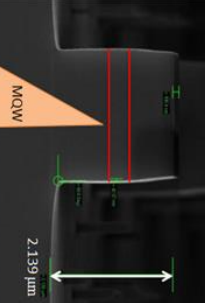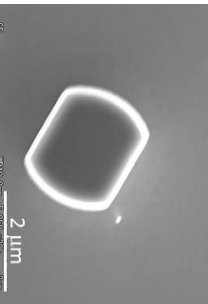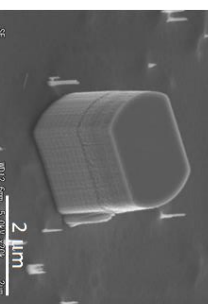|	Cross-section	Top view	3D view	Active core	Etching scheme
Sample 1				Bulk InGaAs	Cl$_2$-based ICP
Sample 2				Bulk InGaAs	Cl$_2$-based ICP
Sample 3				InGaAs/InP QW	CH$_4$/H$_2$-based RIE

Figure 6.3 shows the spectra of fabricated cavities in sample 1 with the same dimensions of 2.2 µm by 2.0 µm but different mirror curvatures. The spectra are pumped by a 532-nm laser at 2.5 mW at room temperature. As poor etching property with undercut and slope, shown in Tab. 6.1, the cavity shape cause extra radiation loss that can dramatically reduce the Q factor. Thus, the spectrum shows quite low Q values of all these cavities.
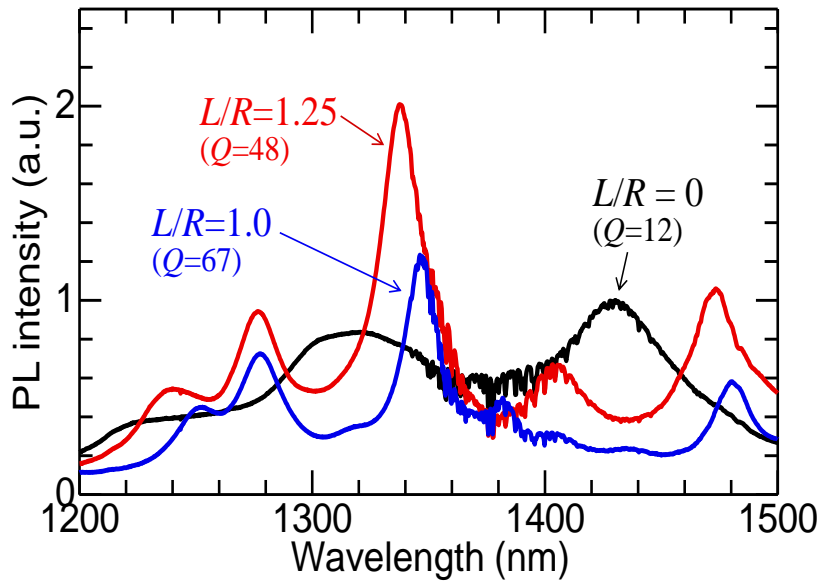
Figure 6.3 PL spectra of capsule-shaped and rectangular metallic cavities on sample 1. All the cavities have the same length (2.2 µm) and width (2.0 µm), and the mirror curvature is shown in the figure.

However, in spite of the low Q values of these cavities in sample 1, the capsule-shaped structure clearly shows an effective improvement of cavity Q factors, as shown in the Fig. 6.3. For example, the Q factor of the conventional rectangular structure ($L/R = 0$) is increased by a factor of 5 by introducing the confocal ($L/R = 1.0$) cylindrical structures.

To confirm the *Q*-factor enhancement effect of capsule-shaped structure, fabrication technique is improved and sample 2 with better etching profiles is taken into PL measurement. Figure 6.4 shows the PL characterization of two different cavities in sample 2, having the same length and width ($L = 1.8$ μm, $W = 1.4$ μm) and different values of mirror curvature of *R*. The pumping condition is a 532-nm laser at 0.9 mW in room temperature.

Figure 6.4 PL spectra of capsule-shaped and rectangular metallic cavities on sample 2. All the cavities have the same length ($L = 1.8$ μm) and width ($W = 1.4$ μm), and the mirror curvature is shown in the figure.

As the optical loss (for example, radiation loss) of sample 2 has been effectively reduced by the improvement of the fabrication process, the spectra in Fig. 6.4 get obvious *Q*-value enhancement rather than that of sample 1. For instance, the *Q* value of conventional rectangular cavity (72) in sample 2 is higher than that of optimal capsule-shaped one (67) in sample 1. This illustrates the importance of good fabrication in small-scale metallic semiconductor lasers.

It should be mentioned that it is not fair to compare the effect of capsule-shaped cavity between cavities on different chips, because of the unknown factors by different fabrication process, such as the dry etching shape, Ag deposition quality, *etc*. To exclude these unknown factors, comparison within the same chip is necessary. As it is shown in Fig. 6.4, for cavities with the same length ($L = 1.8$ μm) and width ($W = 1.4$ μm), by introducing a capsule-shaped design, the Q value can be effectively increased from 72 ($L/R = 0$, 1450-nm peak) to 120 ($L/R = 1$, 1430-nm peak), about 67% improvement. This result proves the 3D-FDTD simulation prediction, which is studied and discussed in Chapter 4.

Figure 6.5 PL spectra varies as the increasing input light power from 0.12 mW to 2.27 mW. Insert, the LL curve corresponding to the spectra. The measured cavity is placed on sample 2, corresponding to the capsule-shaped on in Fig. 6.4.

To study the output-input characterization of the optimal capsule-shaped cavity in Fig. 6.4, increasing light-source power from 0.12 mW to 2.27 mW is input to measure the output power and spectra, which is shown in Figure 6.5. The linewidth

of these spectra does not appear obvious changes or reduction, as this cavity cannot exhibit the lasing behavior, which is also shown in the insert in Fig. 6.5. This is because the cavity Q factor is still too low and thus suffering from high threshold gain required in the active layer of bulk InGaAs. As discussed in Chapter 4, Q value of a few hundreds (or at least above 200) is necessary to achieve an acceptable and practical threshold gain.

To reduce the radiation loss caused from imperfect fabrication process (mainly in dry etching process) and improve the cavity Q factor in further, CH_4/H_2-based RIE is optimized and achieve better anisotropic etching shape, which is shown in Tab. 6.1.
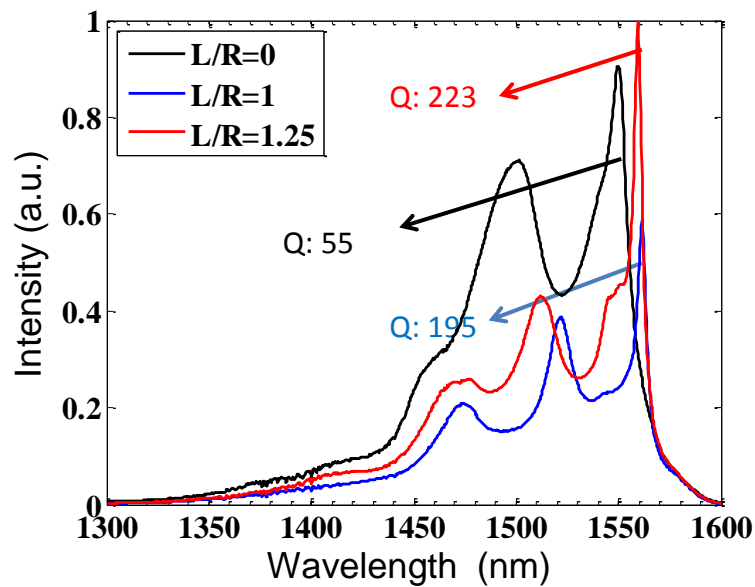
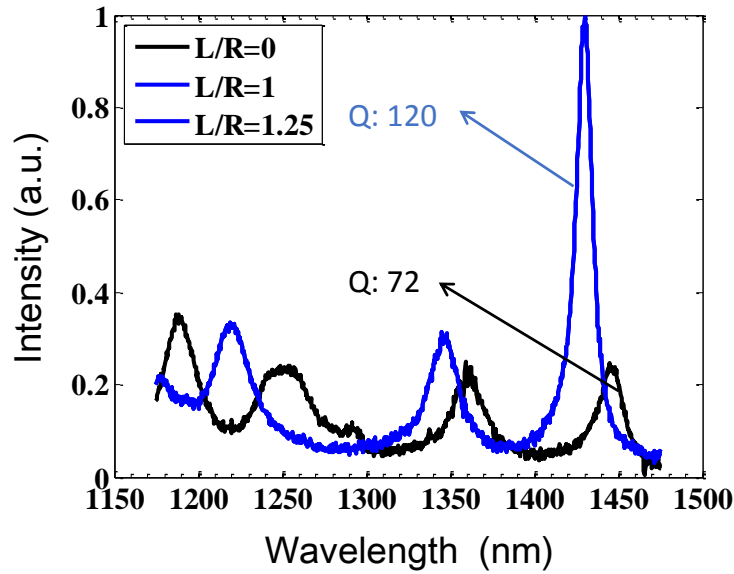

Figure 6.6 PL spectra of capsule-shaped and rectangular metallic cavities on sample 3. All the cavities have the same length ($L = 1.84$ μm) and width ($W = 0.8$ μm), and the mirror curvature is shown in the figure.

Figure 6.6 shows the PL characterization of three different cavities in sample 3, having the same length ($L = 1.84$ μm) and width ($W = 0.8$μm), but different values of mirror curvature of R. The pumping condition is a focused 532-nm laser beam at 0.28 mW in room temperature.

From the main peak around 1564 nm, the Q factors are extracted to be 55, 195, and 223, for the structures with $L/R = 0$ (rectangular), $L/R = 1.0$ (confocal), and $L/R = 1.25$, respectively. Above 4-fold improvement is observed by capsule-shaped design, in sample 3. And the observed cavity Q value is as high as 223, which is almost 2 times larger than that of sample 2. This illustrates that the quality of fabrication does affect the cavity property sensitively.
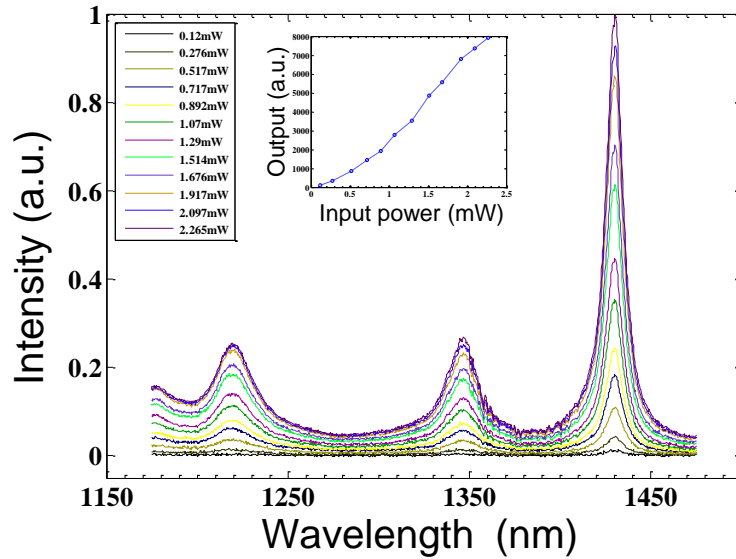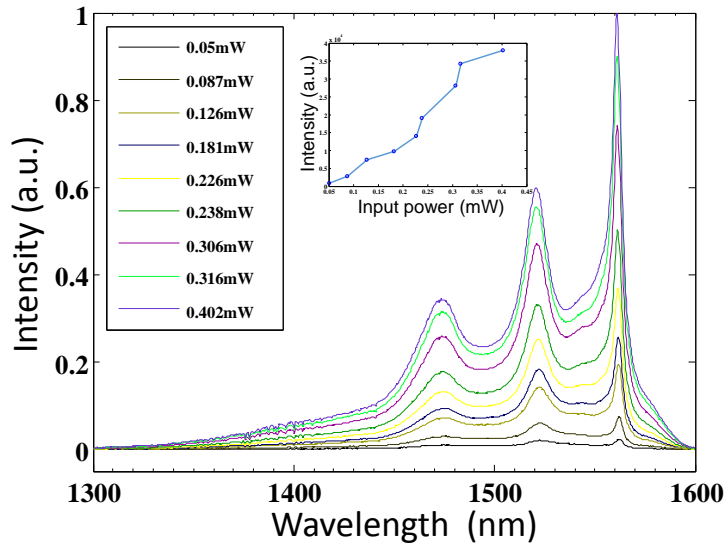

Figure 6.7 PL spectra varies as the increasing input light power from 0.05 mW to 0.40 mW. Insert, the LL curve corresponding to the spectra. The measured cavity is on sample 3, corresponding to the capsule-shaped one with $L/R = 1$ on in Fig. 6.6.

To analyze the emissions of cavities in sample 3 further, LL characterization is measured by increasing the input power from 0.05 mW to 0.40 mW. In spite of that the observed Q factor is around 200 and can be comparable to that value beyond threshold of a recent experimentally demonstrated metallic semiconductor laser [66], our capsule-shaped cavities still cannot achieve lasing, and only emit spectra with higher intensity but similar linewidth when the input power is increasing. This

LL property is shown in Figure 6.7, in the case of a capsule-shaped cavity with length 1.84μm, width 0.8 μm and $L/R = 1$.

One possible reason is that the localized temperature inside the cavity is increasing quickly accompany with the increase of input power, so that the large loss of recombination at high temperature hinders the cavity to achieve lasing threshold. As shown in the insert of Fig. 6.7, the LL curve seems to be "fluctuant", which can be rising quickly by increasing input power a little bit at some points but the magnitude of rising becomes relatively lower if the input power is increasing continuously. This just seems like an output "drop".

Another possible reason is that the extra optical loss (except the radiation loss in sample 2) introduced by the fabrication process, rather than the imperfection of the etching shape, such as the roughness of the sidewalls. The CH_4/H_2 chemistry (used for sample 3) can achieve better anisotropy during RIE, as a penalty, more roughness and corresponding propagation loss can be introduced by more participation of physical etching. Thus, for rectangular cavities with similar dimensions in both sample 2 and 3, similar cavity Q factors are PL observed around the range of a few tens (see in Fig. 6.4 and Fig. 6.6), as the reduced radiation loss from isotropic etching profile in sample 2 is compensated for by the increased propagation loss from roughness on sidewalls in sample 3. However, the capsule-shaped structure pushes the resonant mode distribution effectively into center of cavity, where is far from the sidewalls, and the propagation loss is reduced as well as the metallic loss. This is the reason why capsule-shaped design can achieve a higher enhancement of the Q factor in sample 3 rather than that of sample 2.

To evaluate the Q factor reduction by extra propagation loss caused by roughness on sidewalls, 3D-FDTD simulation of the cavities measured in Fig. 6.6 are carried out as a comparison. The simulated Q factors as a function of mirrors curvature of R are depicted in Figure 6.8.
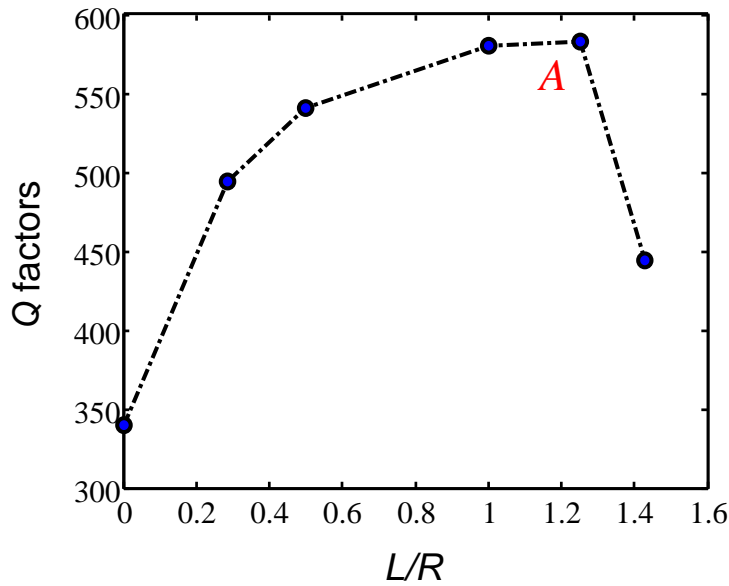
Figure 6.8 Simulated cavity Q factor of a capsule-shaped metallic cavity (L = 1840 nm, W = 800 nm.) for the TE mode, as a function of the mirror curvature. R. The marked point A is corresponding to the main peak of the red curve (L/R = 1.25) in Fig. 6.6.

Fig. 6.8 shows the simulated Q factors of cavities with perfect and smooth sidewalls, which are considerably higher than the measured values in Fig. 6.6. This is because that the high losses from the fabrication process are not included in simulations. In line with the observed spectra by PL measurement, Q factors can be increased dramatically by introducing capsule-shaped design and arrives at the maximum with L/R = 1.25.

Figure 6.9 compares the PL measured and simulated spectra of a capsule-shaped cavity in sample 3, with the dimension of L = 1840 nm, W = 800 nm and L/R = 1.25, which is corresponding to the marked point A in Fig. 6.6.

From Fig. 6.9, firstly, a self-explanatory point is that the main peaks around 1564 nm of both PL measured and simulated spectrum fit to each other well, with a few nanometers mismatch, which can be attributed to the imperfect cavity shape compared to that calculated in simulation. For the range from 1500 nm to 1550 nm,

the measured spectrum has peaks with higher intensity but broader linewidth, in comparison with those in simulation result. This can be attributed to the minute difference of the cavity shape introduced by the fabrication. For the range below 1450 nm, there exist no obvious peaks in the observed spectrum, which is different from the simulated one. This can be attributed to the fact that the material gain is quite low within this range and cannot stimulate any resonant modes.
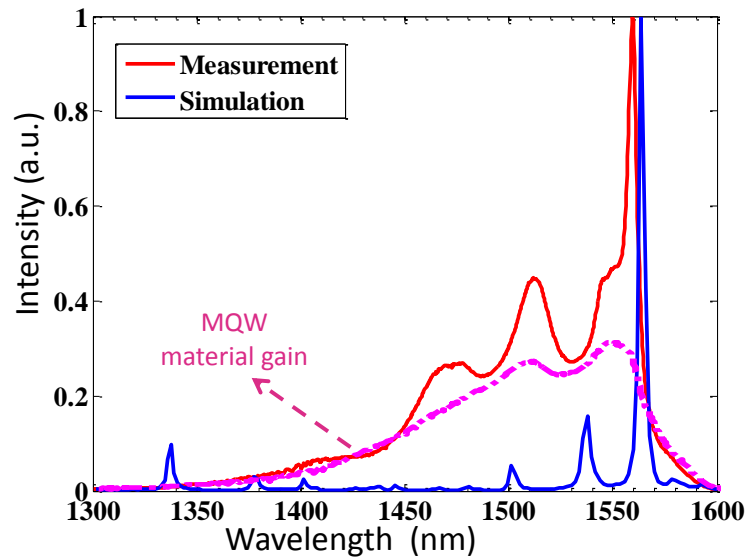
Figure 6.9 PL measured and simulated spectra of a capsule-shaped cavity in sample 3, corresponding to the marked point *A* in Fig. 6.8 (*L* = 1840 nm, *W* = 800 nm and *L/R* = 1.25).

To investigate the resonant mode pattern of the main peak around 1564 nm in Figure 6.9, electrical field distributions of three cross-section planes inside the cavity are shown in Figure 6.10. The observed spectrum is the evanescent field of the resonant FP mode which radiates from the substrate of the cavity.
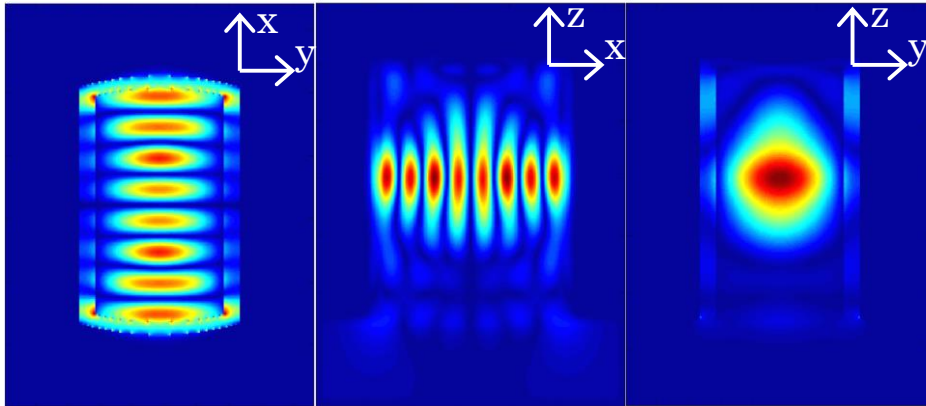
Figure 6.10 Electrical field distribution ($|E|$) of the resonant mode inside a capsule-shaped metallic cavity with $L/R = 1.25$ (corresponding to point A in Fig. 6.9) at three cross-section planes crossing the center of the cavity.

To understand the emitting field that is observed by PL measurement in further, far field of the radiation in Fig. 6.8 is numerically calculated by the NFFT, which is discussed in Chapter 4. Figure 6.11 shows the numerical result of the far-field pattern of the measured cavity in Fig. 6.9, by 3D-FDTD simulation. Unlike the radiation in near field, the far-field radiation shows main intensity distribution far away from the original point (the point perpendicular to the center of the cavity). Considering the fact that the NA of the objective lens used in the PL measurement is not high enough to collect the main patterns (θ around 60^0), only the pattern of moderate intensity ($\theta=0^o$, $\varphi=0^o$) can be collected by this PL setup. This disadvantage makes the measurement difficult and may degrade the pumping efficiency, as higher pumping power is needed to collect the moderate part of the emission.

Up to now, series of cavities are taken into PL measurement and all these observed spectra demonstrate the Q-factor enhancement effect of capsule-shaped structure. All the results are briefly listed in Table 6.2 as a summary.
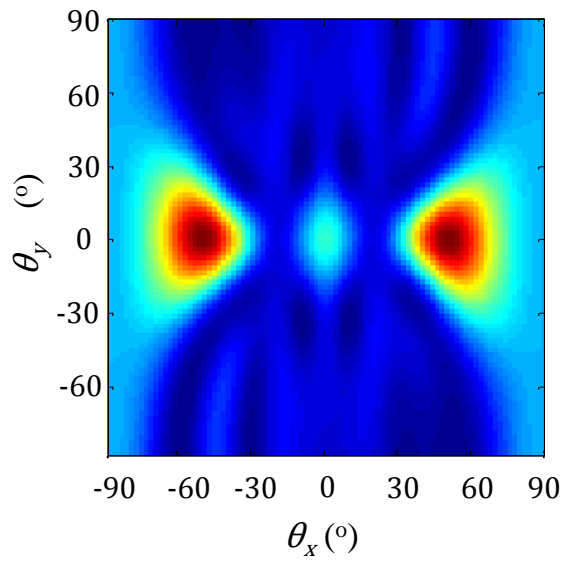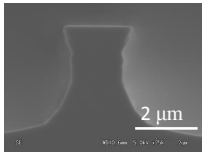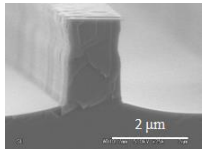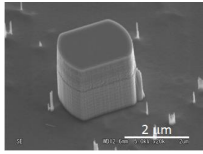
Figure 6.11 Simulated far field of the radiation from a capsule-shaped metallic semiconductor cavity, corresponding to the marked point A in Fig. 6.8 (L = 1840 nm, W = 800 nm and L/R = 1.25).

Table 6.2 List of all PL measurements of capsule-shaped metallic InGaAs/InP cavities

Sample #	Etching profile	Active core	Etching scheme	Foot-print ($/\lambda_0^2$)	Q factor	Enhan-cement
1		Bulk InGaAs	Cl_2-based ICP	2.31	67	5.6 fold
2		Bulk InGaAs	Cl_2-based ICP	1.23	120	1.7 fold
3		InGaAs/ InGaAsP MQW	CH_4/H_2-based RIE	0.60	223	4 fold

6.4 Discussions

6.4.1 Comparison with other demonstrations of metallic nanolasers

In Section 6.3, PL characterizations of series of fabricated capsule-shaped metallic cavities are discussed, and enhanced Q factor of 223 by the proposed structure is experimentally confirmed. Although it still does not achieve lasing, the observed Q value is comparable to other demonstrations of metallic nanolasers, which is shown in Figure 6.12.
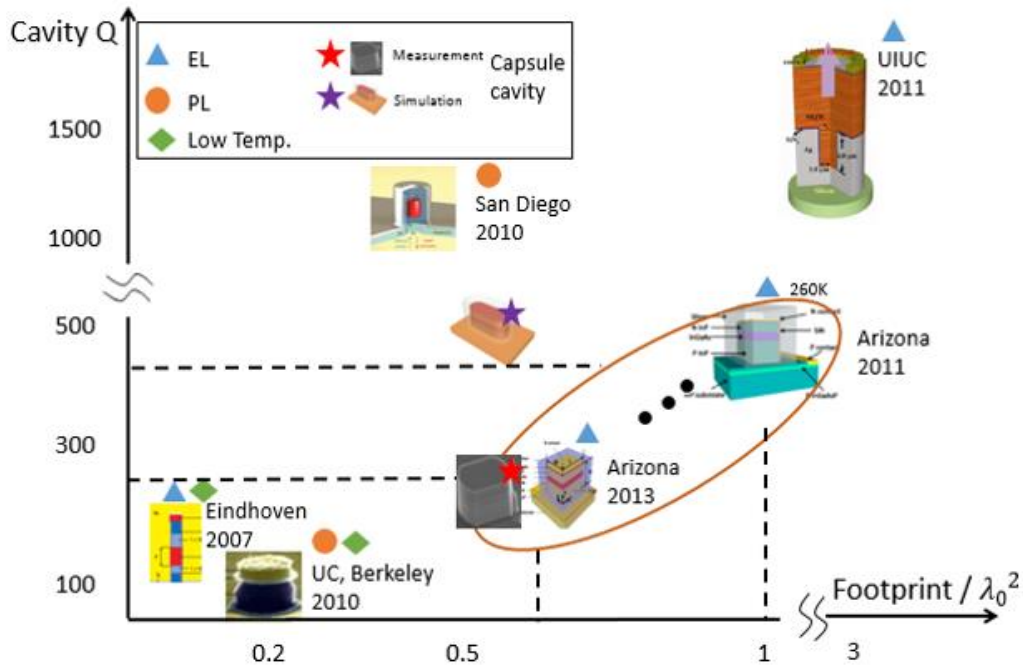
Figure 6.12 Comparison of Q factors between capsule-shaped metallic cavity structure and other demonstrated subwavelength metallic semiconductor lasers.

As it is discussed in Chapter 2, the FP-mode based metallic semiconductor lasers have moderate cavity Q factors and footprint in the successful demonstrations. For the proposed design of capsule-shaped topology, the simulated result shows a

smaller cavity footprint with higher Q factor (see in Fig. 6.12, marked by purple star), which is superior to the properties of conventional rectangular topology.

Due to imperfections of fabrication and the measurement technique in this research, the observed Q factor by PL measurement is much lower (see in Fig. 6.12, marked by red star) than that of simulation result, but still can shrink the cavity footprint with comparable Q value to that of rectangular cavities.

All these points demonstrate the advantage and effectiveness of the proposed capsule-shaped structure.

6.4.2 Obstacles of lasing operation

Lasing operation is not achieved in PL characterization of fabricated capsule-shaped metallic cavity structures in this research, although the Q factor enhancement effect is verified experimentally.

The possible reasons why it cannot achieve lasing are discussed here.

One important reason is the observed cavity Q factor (for example, 223 in case of sample 3) is much lower than that of the simulated one (583, by 3D-FDTD simulation, see in Fig. 6.8), which can be attributed to the extra losses introduced by the fabrication process. First, due to the resolution of EBL and the lift-off process of EB resist, the fabricated pattern is inevitably different from the optimal design. This factor may degrade the ability of the capsule-shaped topology that can confine the light mode like a Gaussian beam. So the field overlap at the sidewalls of a fabricated cavity is not reduced as much as the numerical design. Second, sidewall roughness and slight isotropic structure after dry etching also play vital roles in the decrease of the cavity Q factor, as it can introduce extra propagation loss which is not included in the simulation. Many efforts on two different dry-etching processes are made for the optimal etching shape, and finally the CH_4/H_2-based RIE is chosen for this research. However, slight slant and small roughness of the sidewalls still

exist (see in Fig. 5.9). This is another factor to degrade the performance of the capsule-shaped cavity in the PL measurement. Third, silver cladding of the cavity in this work is used for mirrors, which require high quality. Although the issue of leakage of metallic clad is solved by the improvement of silver-deposition process (see in Fig. 5.11 and 5.12), the quality of silver deposition is not optimized in this work. To reduce the scattering loss and SPP loss in metal surface, a general idea is to deposit the metal layer with larger grain size [104].
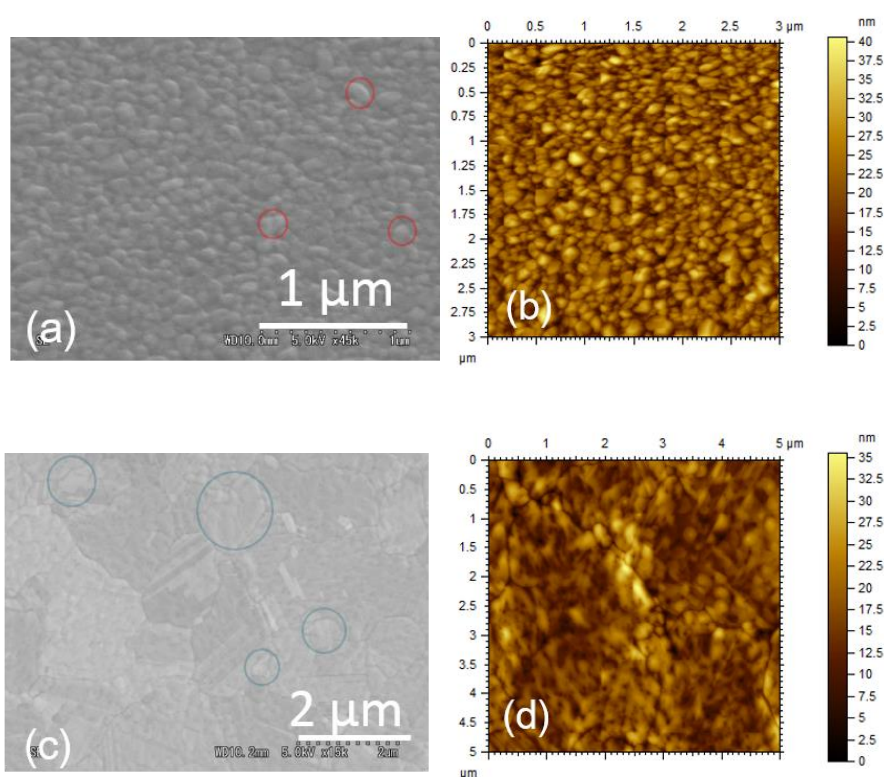
Figure 6.13 Silver surfaces on SiO_2 top of an InP dummy wafer. SEM (a) and AFM (b) images after EB evaporation; SEM (c) and AFM (d) images after un-optimized thermal annealing process.

To check the quality of silver claddings of fabricated metallic cavities in this work, a 300-nm thick silver layer is deposited to the SiO_2 top of an InP dummy wafer by EB evaporation, and then is examined by SEM and atomic force

microscope (AFM), shown in Figure 6.13. The grain size of silver surface can be improved from about tens of nanometers (after EB evaporation) to hundreds of nanometers by un-optimized thermal annealing process, while larger grain size that can be comparable to the cavity size is of great importance to achieve lasing at room temperature[66]. Thus, the thermal annealing of silver deposition process is also to be optimized in future work.

Another reason is the thermal effect of the sub-wavelength metallic cavity lasers. When the pumping light is injected into the cavity, the localized temperature at the active layer may increase quickly and cause extra thermal loss. Detailed discussion of this point is given in Section 6.3. As the target of this work is to demonstrate the effectiveness of the proposed capsule-shaped topology for sub-wavelength metallic cavity lasers, the optimization of thermal dissipation is not included and considered in this research. One method of overcome thermal effect is taking PL measurement in low temperature, and using pulsed laser with infrared frequency as the pumping source; while a more fundamental way is to investigated the thermal-dissipation issue of the metallic cavity and optimize the cavity structure, as well as the selection of insulator layer for better thermal performance, which will be studied in the future work.

A further issue is how far are the fabricated metallic cavity structures from lasing in this PL measurement? To this end, the threshold pumping power is studied theoretically in the following. It can be derived simply from the Eq. (3.8), by rewriting the carrier density in the form of optical injection (assuming quantum efficiency is 100%)

$$P_{th} = \frac{h\upsilon V(BN_{th}^2 + CN_{th}^3)}{\eta_i}, \tag{6.1}$$

where P_{th} is the threshold power by optical pumping, h is the Plank constant, υ is the frequency of the pumping laser, η_i is the optical injection efficiency, and other

parameters are the same as those in Tab. 4.2. The η_i is estimated by the overlap of focused 532-nm laser beam spot and the fabricated cavity size. Taking into account facts that the diameter of the incident laser beam is about 3 mm and the focal length of the objective lens is 10 mm, the focused spot size can be derived simply to be about 4.33 μm, by the approximation of focused Airy patterns. And considering the fabricated and measured cavities in this work are mainly in the range of 1~2 μm, here, the cavity length and width is assumed to be 2 μm and 1 μm respectively. Thus, the η_i can be evaluated to be about 10% under all these assumptions, and the P_{th} is estimated by Eq. (6.1) as a function of cavity Q factor, shown in Figure 6.14.
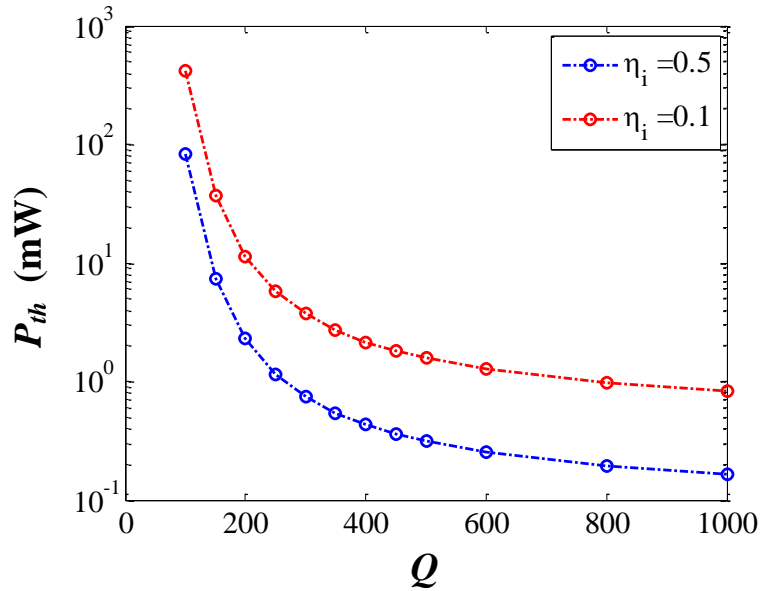
Figure 6.14 Estimated threshold power P_{th} of a capsule-shaped metallic cavity with 2 μm by 1 μm dimensions, as a function of Q factor ($L/R = 1$). A 532-nm focused laser beam is used for pumping light in this calculation.

From Fig. 6.14, it is obvious that for the metallic cavity ($L = 2$ μm, $W = 1$ μm, $L/R = 1$) pumped by a focused 532-nm laser beam in current PL system, the threshold power (red curve with injection efficiency of 10%) is considerably higher than that applied in measurements in Section 6.3. This explains why lasing is not achieved.

For example, in the case of Q value around 200, a threshold power of 11.4 mW is needed. Such a high pumping power may cause severe thermal loss and even damage the cavity, as it is discussed in the previous section. However, there still exists space to be improved.

One solution to reduce the threshold power is improving the cavity Q factors. As it is shown in Fig. 6.14 in red curve, the threshold power can be lowered down to about 1.6 mW if the Q value can be enhanced to 500, which is possible and numerically demonstrated in Fig. 6.8. Fabrication process needs to be improved and optimized to increase the Q factor, as discussed above.

Another improvement can be taken by utilizing an infrared laser as the pumping source. Compared with green laser used in this work, infrared laser takes the advantage of lower photon energy, which not only reduces the thermal loss of the cavity, but also increases carrier density inside so that the threshold power can be estimated to be reduced by half.

Further, high-NA lens can be mounted in the PL system for a smaller focused spot size, in order to improve the pumping efficiency effectively. For instance, if an objective lens with a focal length of 5 mm is used instead of the current one with a 10-mm focal length, the focus spot is shrunk to 2.2 μm and close to 50% injection efficiency can be achieved. As a result, the threshold power (blue curve) is dramatically reduced, compared to that of a low-NA lens (red curve), shown in Fig. 6.14. For example, the P_{th} can be reduced to 2.3 mW for the a cavity with Q value of 200, which is practical in the PL measurement.

Thus, for the proposed capsule-shaped metallic semiconductor cavity structure, it is practical to achieve lasing by making the three improvements discussed above in future work.

6.5 Conclusion

In this chapter, properties of fabricated capsule-shaped metallic InGaAs/InP cavities are characterized by PL. Firstly, the PL system is introduced briefly and the steps of measurement are also illustrated. As the objective cavities are in few-micrometers or even smaller scale, to distinguish a specified cavity with sophisticated design is an important issue. Here, a steering stage with resolution of 0.1 nm by an electrical mechanism is used to find and locate the precise location, and solving this problem well.

Secondly and most importantly, the PL measurement results are studied and analyzed in details. For series of samples with different shapes and qualities due to the fabrication process, the PL characterizations all experimentally confirm the Q factor enhancement effect of capsule-shaped cavity, compared to the conventional rectangular one, which demonstrates the 3D-FDTD simulation prediction in Chapter 4. Besides, better fabrication process can bring better sample quality with reduced optical loss, and thus can achieve higher cavity Q factors of PL emission. Due to different process, extra optical loss caused from isotropic etching shape or roughness sidewalls can be introduced to the fabricated samples, which is also discussed in this chapter. Besieds, simulations of the measured cavities are carried out to show a good consistency with experimental results.

Thirdly, factors that can hinder achieving lasing are analyzed and discussed. In spite of the observed Q factor of 223 in PL characterization, which is comparable and quite close to those of the successfully demonstrated metallic-cavity lasers, lasing is not achieved or not observed in the measurement. One reason is the extra high loss introduced from the fabrication process, even the process techniques are improved in this study (see details in Chapter 5), can reduce the designed Q values easily. Another reason is the local temperature inside the measuring cavities that can increase recombination loss quickly.

In short, by PL characterization of the fabricated capsule-shaped metallic InGaAs/InP cavities, it is experimentally confirmed that the proposed novel structure does reduce the metallic loss of the cavity and increase the Q factor effectively, in consistence with the 3D-FDTD simulation prediction. This is the most important issue in this dissertation and demonstrates the proof of concept of the proposal. Due to some reasons rather than the structure design but the fabrication and measurement technique, lasing is not observed yet, several corresponding improvements should be done in the future to achieve lasing.

Chapter 7

Conclusion

In this dissertation, a novel metallic semiconductor laser structure of "capsule-shaped cavity" is proposed, simulated and experimentally studied for the first time. This capsule-shaped design can form Gaussian-like mode profile and reduce the field overlap at the metallic sidewalls. Thus, the cavity Q factor can be improved effectively with the reduced SPP loss. Aiming at miniaturization of semiconductor lasers for applications in large-scale PICs, the proposed capsule-shaped structure is studied systemically in this work and therefore

In Chapter 2, the state of the art of metallic cavity lasers is investigated, including the cavity structures, lasing modes, metallic losses, and operating conditions. On the one hand, WG modes and FP modes, corresponding to circular and rectangular cavities, has advantages and disadvantages respectively, and both of them are experimentally demonstrated in recent years. On the other hand, considering the potential applications in PICs, the use of metallic lasers by waveguide coupling and the compatibility with other devices are two important issues, for which the FP-mode based cavity is more suitable. To reduce the high loss at the metallic sidewalls in the conventional rectangular FP cavity, a new design of capsule-shaped cavity with curved mirrors is proposed, which can support Gaussian-like resonant mode that is far away from the sidewalls.

In Chapter 3, theoretical analysis of the proposed metallic InGaAs/InP cavity lasers is done by the rate equation theory, and formulations of threshold gain and threshold current are derived. To estimate these values, cavity Q factors and confinement factors should be derived. Waveguide theory is used for an intuitive understanding and analysis, while some important issues such as the radiation field, mode pattern and precise cavity Q factor cannot be taken into account by this 1D or 2D theory. Then 3D-FDTD simulation method is briefly introduced, which is necessary for the novel structures. NFFT is also part of this chapter, as it is an important issue in both practical applications and measurements.

In Chapter 4, a series of 3D-FDTD simulations of capsule-shaped metallic cavities is carried out and discussed in details, including Q factors, mode patterns, confinement factors, threshold gains, threshold currents, radiation efficiency, waveguide coupling efficiency and far field radiation. It is numerically confirmed that by introducing an optimal capsule-shaped structure, Q value can be improved above 50%, compared to a conventional rectangular cavity. Besides, the threshold gain and current can be reduced exponentially by the proposed design. And further issues such as size shrinking effect, ease of waveguide coupling, external radiation efficiency are further discussed in this chapter. All these simulation results numerically demonstrate that the proposal in this dissertation is suitable and efficient for the ultra-small lasers for the potential applications in PICs.

In Chapter 5, fabrication of the capsule-shaped metallic InGaAs/InP cavity is performed for the first time. Extra losses can be introduced to this structure by imperfect fabrication process, which worsens the quality and property of the cavities. To overcome this challenge, some fabrication techniques are explored and improved, especially in the process such as dry etching and metal deposition.

In Chapter 6, PL characterization of fabricated cavities is measured and analyzed. All the observed spectra demonstrate the Q-factor enhancement effect of capsule-shaped structure, compared to that of a conventional rectangular cavity; and up to 4-fold improvement is achieved experimentally. These measured results are consistent with 3D-FDTD simulation prediction, and confirm the effectiveness of the proposal.

From all the simulated and experimental results, the proposed capsule-shaped metallic InGaAs/InP cavity structure is really suitable for the light source in PICs. This new design can reduce the high loss in the conventional metal-clad lasers, and is relatively easy to be coupled in the waveguide, and is compatible with other devices in PICs. It can be concluded that this proposal of capsule-shaped cavity is an essential component of the large-scale PICs in the future.

References

[1]   S. E. Miller, "Integrated optics: An Introduction," *Bell Syst. Tech. J.*, vol. 48, no. 7, pp. 2059–2069, 1969.

[2]   G. Gilardi and M. K. Smit, "Generic InP-Based Integration Technology : Present and Prospects," *Prog. Electromagn. Res.*, vol. 147, pp. 23–35, 2014.

[3]   I. M. Soganci, T. Tanemura, and Y. Nakano, "Integrated phased-array switches for large-scale photonic routing on chip," *Laser Photonics Rev.*, vol. 6, no. 4, pp. 549–563, 2012.

[4]   M. Kwack, T. Tanemura, A. Higo, and Y. Nakano, "Monolithic InP strictly non-blocking 8 ×8 switch for high-speed WDM optical interconnection," *Opt. Express*, vol. 20, no. 27, pp. 28734–28741, 2012.

[5]   S. W. Corzine, P. Evans, M. Fisher, J. Gheorma, M. Kato, V. Dominic, P. Samra, A. Nilsson, J. Rahn, I. Lyubomirsky, A. Dentai, P. Studenkov, M. Missey, D. Lambert, A. Spannagel, R. Muthiah, R. Salvatore, S. Murthy, E. Strzelecka, J. L. Pleumeekers, A. Chen, R. Schneider, R. Nagarajan, M. Ziari, J. Stewart, C. H. Joyner, F. Kish, and D. F. Welch, "Large-scale InP transmitter PICs for PM-DQPSK fiber transmission systems," *IEEE Photonics Technol. Lett.*, vol. 22, no. 14, pp. 1015–1017, 2010.

[6]   F. M. Soares, N. K. Fontaine, R. P. Scott, J. H. Baek, X. Zhou, T. Su, S. Cheung, Y. Wang, C. Junesand, S. Lourdudoss, K. Y. Liou, R. a. Hamm, W. Wang, B. Patel, L. a. Gruezke, W. T. Tsang, J. P. Heritage, and S. J. B. Yoo, "Monolithic InP 100-Channel 10-GHz Device for Optical Arbitrary Waveform Generation," *IEEE Photonics J.*, vol. 3, no. 6, pp. 975–985, 2011.

[7]   S. C. Nicholes, M. L. Mašanović, B. Jevremović, E. Lively, L. a. Coldren, and D. J. Blumenthal, "Large-scale photonic integration for advanced all-optical routing functions," in *Integrated Photonics Research, Silicon and Nanophotonics*, 2010.

[8]   C. A. M. Steenbergen, C. van Dam, A. Looijen, C. G. P. Herben, M. de Kok, M. K. Smit, J. W. Pedersen, I. Moerman, R. G. F. Baets, and B. H. Verbeek, "Compact low loss 8 × 10 GHz polarisation independent WDM receiver," *Proc. Eur. Conf. Opt. Commun.*, vol. 1, pp. 129–132, 1996.

[9]   H. Takaiashi, S. Suzuki, K. Kat0, and I. Nishi, "Arrayed-Waveguide Grating for Wavelength Division M Ulti/Dem U Ltiplexer With Nanom Etr E Resolution," *Electron. Lett.*, vol. 26, no. 2, pp. 87–88, 1990.

[10]   M. K. Smit, "New focusing and dispersive planar component based on an optical phased array," *Electron. Lett.*, vol. 24, no. 7, pp. 17–18, 1988.

[11]   M. Smit, J. van der Tol, and M. Hill, "Moore's law in photonics," *Laser Photonics Rev.*, vol. 6, no. 1, pp. 1–13, 2012.

[12]   H. Altug, D. Englund, and J. Vučković, "Ultrafast photonic crystal nanocavity laser," *Nat. Phys.*, vol. 2, pp. 484–488, 2006.

[13]   R. N. Hall, G. E. Fenner, J. D. Kingsley, T. J. Soltys, and R. O. Carlson, "Coherent light emission from GaAs junctions," *Phys. Rev. Lett.*, vol. 9, no. 9, pp. 366–368, 1962.

[14]   M. I. Nathan, W. P. Dumke, G. Burns, F. H. Dill, and G. Lasher, "Stimulated emission of radiation from GaAs p-n junctions," *Appl. Phys. Lett.*, vol. 1, no. 3, pp. 62–64, 1962.

[15]   T. M. Quist, R. H. Rediker, R. J. Keyes, W. E. Krag, B. Lax, a. L. McWhorter, and H. J. Zeigler, "Semiconductor maser of GaAs," *Appl. Phys. Lett.*, vol. 1, no. 4, pp. 91–92, 1962.

[16]   N. Holonyak and S. F. Bevacqua, "Coherent (visible) light emission from Ga(As1-xPx) junctions," *Appl. Phys. Lett.*, vol. 1, no. 4, pp. 82–83, 1962.

[17]   S. Reitzenstein, A. Bazhenov, A. Gorbunov, C. Hofmann, S. München, A. Löffler, M. Kamp, J. P. Reithmaier, V. D. Kulakovskii, and A. Forchel, "Lasing in high-Q quantum-dot micropillar cavities," *Appl. Phys. Lett.*, vol. 89, p. 051107, 2006.

[18]   S. Reitzenstein, C. Kistner, S. Munch, T. Heindel, C. Schneider, M. Strauss, A. Rahimi-Iman, K. Morgener, S. Hofling, M. Kamp, and A. Forchel, "Quantum dot micropillar lasers," *Commun. Photonics Conf. Exhib.*, vol. 2009-Suppl, pp. 1–10, 2009.

[19]   S. Reitzenstein, T. Heindel, C. Kistner, A. Rahimi-Iman, C. Schneider, S. Höfling, and A. Forchel, "Low threshold electrically pumped quantum dot-micropillar lasers," *Appl. Phys. Lett.*, vol. 93, p. 061104, 2008.

[20]   H. a M. Leymann, C. Hopfmann, F. Albert, A. Foerster, M. Khanbekyan, C. Schneider, S. Höfling, A. Forchel, M. Kamp, J. Wiersig, and S. Reitzenstein, "Intensity fluctuations in bimodal micropillar lasers enhanced by quantum-dot gain competition," *Phys. Rev. A*, vol. 87, p. 053819, 2013.

[21]   K. Ohira, S. Member, T. Murayama, S. Tamura, and S. Arai, "Low-Threshold and High-Efficiency Operation of Distributed Reflector Lasers With Width-Modulated Wirelike Active Regions," *IEEE J. Sel. Top. Quantum Electron.*, vol. 11, no. 5, pp. 1162–1168, 2005.

[22] Y. Akahane, T. Asano, and B. Song, "High- Q photonic nanocavity in a two-dimensional photonic crystal," *Nature*, vol. 425, pp. 944–947, 2003.

[23] L. Zhu, P. Chak, J. K. S. Poon, G. A. Derose, A. Yariv, and A. Scherer, "Electrically-pumped, broad-area, single-mode photonic crystal lasers," *Opt. Express*, vol. 15, no. 10, pp. 5966–5975, 2007.

[24] H.-G. Park, S.-H. Kim, S.-H. Kwon, Y.-G. Ju, J.-K. Yang, J.-H. Baek, S.-B. Kim, and Y.-H. Lee, "Electrically driven single-cell photonic crystal laser.," *Science*, vol. 305, no. 5689, pp. 1444–1447, 2004.

[25] B. Ellis, M. a. Mayer, G. Shambat, T. Sarmiento, J. Harris, E. E. Haller, and J. Vuckovic, "Ultra-low Threshold electrically pumped quantum dot photonic crystal nanocavity laser," *Nat. Photonics*, vol. 5, pp. 297–300, 2011.

[26] X. Wu, a. Yamilov, X. Liu, S. Li, V. P. Dravid, R. P. H. Chang, and H. Cao, "Ultraviolet photonic crystal laser," *Appl. Phys. Lett.*, vol. 85, no. 17, pp. 3657–3659, 2004.

[27] H. Altug and J. Vucković, "Photonic crystal nanocavity array laser," *Opt. Express*, vol. 13, no. 22, pp. 8819–8828, 2005.

[28] M. Nakamura, H. W. Yen, A. Yariv, E. Garmire, S. Somekh, and H. L. Garvin, "Laser oscillation in epitaxial GaAs waveguides with corrugation feedback," *Appl. Phys. Lett.*, vol. 23, no. 5, pp. 224–225, 1973.

[29] D. Englund, H. Altug, I. Fushman, and J. Vučković, "Efficient terahertz room-temperature photonic crystal nanocavity laser," *Appl. Phys. Lett.*, vol. 91, p. 071126, 2007.

[30] T. Baba and D. Sano, "Low-Threshold Lasing and Purcell Effect in Microdisk Lasers at Room Temperature," *IEEE J. Sel. Top. Quantum Electron.*, vol. 9, no. 5, pp. 1340–1346, 2003.

[31] L. Mahler, A. Tredicucci, R. P. Green, F. Beltram, C. Walther, J. Faist, H. E. Beere, and D. A. Ritchie, "Vertically emitting microdisk lasers," *Nat. Photonics*, vol. 3, pp. 46–49, 2008.

[32] Y. Kim, S. Kwon, J. M. Lee, M. Hwang, J. Kang, W. Il Park, and H. Park, "Graphene-contact electrically driven microdisk lasers," *Nat. Commun.*, vol. 3, p. 1123, 2012.

[33] P. Feng, Y. Zhang, Y. Wang, L. Liu, S. Zhang, H. Wang, and W. Zheng, "A novel hybrid III–V/silicon deformed micro-disk single-mode laser," *J. Semicond.*, vol. 36, no. 2, p. 024012, 2015.

[34] P. Mechet, S. Verstuyft, T. de Vries, T. Spuesens, P. Regreny, D. van Thourhout, G. Roelkens, and G. Morthier, "Unidirectional III-V microdisk lasers heterogeneously integrated on SOI," *Opt. Express*, vol. 21, no. 16, pp. 19339–19352, 2013.

[35] L. Liu, T. Spuesens, G. Roelkens, D. van Thourhout, P. Regreny, and P. Rojo-Romeo, "A thermally tunable IIIV compound semiconductor microdisk laser integrated on silicon-on-insulator circuits," *IEEE Photonics Technol. Lett.*, vol. 22, no. 17, pp. 1270–1272, 2010.

[36] C. Guo, Y. Huang, Y. Yang, X. Lv, and Q. Yao, "Design of unidirectional emission silicon/III-V laser for on-chip interconnects," *Front. Optoelectron.*, vol. 5, no. 1, pp. 94–98, 2012.

[37] D. L. Huffaker, D. G. Deppe, K. Kumar, and T. J. Rogers, "Native-oxide defined ring contact for low threshold vertical-cavity lasers," *Appl. Phys. Lett.*, vol. 65, no. 1, pp. 97–99, 1994.

[38] S. Nakamura, M. Senoh, and T. Mukai, "High-power InGaN/GaN double-heterostructure violet light emitting diodes," *Appl. Phys. Lett.*, vol. 62, no. 19, pp. 2390–2392, 1993.

[39] I. Hayashi, M. B. Panish, P. W. Foy, and S. Sumski, "Junction lasers which operate continuously at room temperature," *Appl. Phys. Lett.*, vol. 17, no. 3, pp. 109–111, 1970.

[40] M. Nakamura, A. Yariv, H. W. Yen, S. Somekh, and H. L. Garvin, "Optically pumped GaAs surface laser with corrugation feedback," *Appl. Phys. Lett.*, vol. 22, no. 10, pp. 515–516, 1973.

[41] K. Iga, S. Ishikawa, S. Ohkouchi, and T. Nishimura, "Room Temperature Pulsed Oscillation of GaAlAs/GaAs Surface Emitting Junction Laser," *IEEE J. Quantum Electron.*, vol. QE-21, no. 6, pp. 663–668, 1985.

[42] H. Soda, K. Iga, C. Kitahara, and Y. Suematsu, "GaInAsP/InP Surface Emitting Injection Lasers," *Jpn. J. Appl. Phys.*, vol. 18, no. 12, pp. 2329–2330, 1979.

[43] N. Chen, Y. Nakano, K. Okamoto, K. Tada, G. I. Morthier, and R. G. Baets, "Analysis, fabrication, and characterization of tunable DFB lasers with chirped gratings," *IEEE J. Sel. Top. Quantum Electron.*, vol. 3, no. 2, pp. 541–545, 1997.

[44] Y. Luo, Y. Nakano, K. Tada, T. Inoue, H. Hosomatsu, and H. Iwaoka, "Purely gain-coupled distributed feedback semiconductor lasers," *Appl. Phys. Lett.*, vol. 56, no. 17, pp. 1620–1622, 1990.

[45]   Y. Luo, H. L. Cao, M. Dobashi, H. Hosomatsu, Y. Nakano, and K. Tada, "Gain-coupled distributed feedback semiconductor lasers with an absorptive conduction-type inverted grating," *IEEE Photonics Technol. Lett.*, vol. 4, no. 7, pp. 692–695, 1992.

[46]   Y. Nakano and K. Tada, "Analysis, design, and fabrication of GaAlAs/GaAs DFB lasers with modulated stripe width structure for complete single longitudinal mode oscillation," *IEEE J. Quantum Electron.*, vol. 24, no. 10, pp. 2017–2033, 1988.

[47]   Y. Nakano, Y. Luo, and K. Tada, "Facet reflection independent, single longitudinal mode oscillation in a GaAlAs/GaAs distributed feedback laser equipped with a gain-coupling mechanism," *Appl. Phys. Lett.*, vol. 55, no. 16, pp. 1606–1608, 1989.

[48]   Y. Nakano, H. L. Cao, K. Tada, Y. Luo, M. Dobashi, and H. Hosomatsu, "Absorptive-grating gain-coupled distributed-feedback MQW lasers with low threshold current and high single-longitudinal-mode yield," *Jpn. J. Appl. Phys.*, vol. 32, no. 2, pp. 825–829, 1993.

[49]   Y. Nakano, Y. Uchida, and K. Tada, "Highly Efficient Single Longitudinal-Mode Oscillation Capability of Gain-Coupled Distributed Feedback Semiconductor Lasers-Advantage of Asymmetric Facet Coating," *IEEE Photonics Technol. Lett.*, vol. 4, no. 4, pp. 308–311, 1992.

[50]   S. Kita, S. Otsuka, S. Hachuda, T. Endo, Y. Imai, Y. Nishijima, H. Misawa, and T. Baba, "Photonic Crystal Nanolaser Biosensors," *IEICE Trans. Electron.*, vol. E95–C, no. 2, pp. 188–198, 2012.

[51]   S. Matsuo, T. Sato, K. Takeda, A. Shinya, K. Nozaki, E. Kuramochi, H. Taniyama, M. Notomi, T. Fujii, K. Hasebe, and T. Kakitsuka, "Photonic crystal lasers using wavelength-scale embedded active region," *J. Phys. D. Appl. Phys.*, vol. 47, p. 023001, 2014.

[52]   K. Takeda, T. Sato, A. Shinya, K. Nozaki, W. Kobayashi, H. Taniyama, M. Notomi, K. Hasebe, T. Kakitsuka, and S. Matsuo, "Few-fJ/bit data transmissions using directly modulated lambda-scale embedded active region photonic-crystal lasers," *Nat. Photonics*, vol. 7, pp. 569–575, 2013.

[53]   S. Matsuo, K. Takeda, T. Sato, M. Notomi, A. Shinya, K. Nozaki, H. Taniyama, K. Hasebe, and T. Kakitsuka, "Room-temperature continuous-wave operation of lateral current injection wavelength-scale embedded active-region photonic-crystal laser," *Opt. Express*, vol. 20, no. 4, pp. 3773–3780, 2012.

[54]   T. Shindo, M. Futami, T. Okumura, R. Osabe, T. Koguchi, T. Amemiya, N. Nishiyama, and S. Arai, "Lateral-current-injection type membrane DFB laser with surface grating," *IEEE Photonics Technol. Lett.*, vol. 25, no. 13, pp. 1282–1285, 2013.

[55] T. Shindo, T. Okumura, H. Ito, T. Koguchi, D. Takahashi, Y. Atsumi, J. Kang, R. Osabe, T. Amemiya, N. Nishiyama, and S. Arai, "GaInAsP/InP lateral-current-injection distributed feedback laser with a-Si surface grating," *Opt. Express*, vol. 19, no. 3, pp. 1884–1891, 2011.

[56] H. Song, K. Takemoto, T. Miyazawa, M. Takatsu, S. Iwamoto, T. Yamamoto, and Y. Arakawa, "Design of Si/SiO2 micropillar cavities for Purcell-enhanced single photon emission at 1.55 μm from InAs/InP quantum dots," *Opt. Lett.*, vol. 38, no. 17, pp. 3241–3244, 2013.

[57] D. Cao, A. Tandaechanurat, S. Nakayama, S. Ishida, S. Iwamoto, and Y. Arakawa, "Silicon-based three-dimensional photonic crystal nanocavity laser with InAs quantum-dot gain," *Appl. Phys. Lett.*, vol. 101, p. 191107, 2012.

[58] S. L. Chuang, C. Lu, and A. Matsudaira, "METAL-CAVITY NANOLASERS: HOW SMALL CAN THEY GO?," in *17th Microoptics Conf.*, 2011.

[59] S. L. McCall, a. F. J. Levi, R. E. Slusher, S. J. Pearton, and R. A. Logan, "Whispering-gallery mode microdisk lasers," *Appl. Phys. Lett.*, vol. 60, no. 3, pp. 289–291, 1992.

[60] M. T. Hill, Y. S. Oei, B. Smalbrugge, Y. Zhu, T. de Vries, P. J. van Veldhoven, F. W. M. van Otten, T. J. Eijkemans, J. P. Turkiewicz, H. de Waardt, E. J. Geluk, S. H. Kwon, Y. H. Lee, R. Nötzel, and M. K. Smit, "Lasing in metallic-coated nanocavities," *Nat. Photonics*, vol. 1, pp. 589–594, 2007.

[61] S. H. Kwon, J. H. Kang, C. Seassal, S. K. Kim, P. Regreny, Y. H. Lee, C. M. Lieber, and H. G. Park, "Subwavelength plasmonic lasing from a semiconductor nanodisk with silver nanopan cavity," *Nano Lett.*, vol. 10, pp. 3679–3683, 2010.

[62] K. Ding and C. Z. Ning, "Metallic subwavelength-cavity semiconductor nanolasers," *Light Sci. Appl.*, vol. 1, p. e20, 2012.

[63] M. Khajavikhan, A. Simic, M. Katz, J. H. Lee, B. Slutsky, A. Mizrahi, V. Lomakin, and Y. Fainman, "Thresholdless Nanoscale Coaxial Lasers," *Nature*, vol. 482, pp. 204–207, 2011.

[64] M. T. Hill, M. Marell, E. S. P. Leong, B. Smalbrugge, Y. Zhu, M. Sun, P. J. van Veldhoven, E. J. Geluk, F. Karouta, Y. S. Oei, R. Nötzel, C. Z. Ning, and M. K. Smit, "Lasing in metal-insulator-metal sub-wavelength plasmonic waveguides.," *Opt. Express*, vol. 17, no. 13, pp. 11107–11112, 2009.

[65] K. Yu, A. Lakhani, and M. C. Wu, "Subwavelength metal-optic semiconductor nanopatch lasers," *Opt. Express*, vol. 18, no. 9, pp. 8790–8799, 2010.

[66]   K. Ding, M. T. Hill, Z. C. Liu, L. J. Yin, P. J. van Veldhoven, and C. Z. Ning, "Record performance of electrical injection sub-wavelength metallic-cavity semiconductor lasers at room temperature," *Opt. Express*, vol. 21, no. 4, pp. 4728–4733, 2013.

[67]   C. Y. Lu, S. L. Chuang, A. Mutig, and D. Bimberg, "Metal-cavity surface-emitting microlaser with hybrid metal-DBR reflectors," *Opt. Lett.*, vol. 36, no. 13, pp. 2447–2449, 2011.

[68]   M. J. H. Marell, B. Smalbrugge, E. J. Geluk, P. J. van Veldhoven, B. Barcones, B. Koopmans, R. Nötzel, M. K. Smit, and M. T. Hill, "Plasmonic distributed feedback lasers at telecommunications wavelengths," *Opt. Express*, vol. 19, no. 16, pp. 15109–15118, 2011.

[69]   R. Perahia, T. P. M. Alegre, A. H. Safavi-Naeini, and O. Painter, "Surface-plasmon mode hybridization in subwavelength microdisk lasers," *Appl. Phys. Lett.*, vol. 95, p. 201114, 2009.

[70]   C. Lu, S. Chang, S. L. Chuang, T. D. Germann, U. W. Pohl, and D. Bimberg, "CW substrate-free metal-cavity surface microemitters at 300 K," *Semicond. Sci. Technol.*, vol. 26, p. 014012, 2011.

[71]   C. Lu, S. Chang, S. L. Chuang, T. D. Germann, U. W. Pohl, and D. Bimberg, "Characteristics of Metal-Cavity Surface-Emitting Microlaser," in *Proc. IEEE Photon. Soc. Annu. Meeting,* 2010, pp. 240–241.

[72]   P. Berini and I. De Leon, "Surface plasmon–polariton amplifiers and lasers," *Nat. Photonics*, vol. 6, pp. 16–24, 2012.

[73]   M. T. Hill, "Status and prospects for metallic and plasmonic nano-lasers," *J. Opt. Soc. Am. B*, vol. 27, no. 11, p. B36, 2010.

[74]   R. F. Oulton, "Surface plasmon lasers: Sources of nanoscopic light," *Mater. Today*, vol. 15, pp. 26–34, 2012.

[75]   C. Z. Ning, "Semiconductor nanolasers," *Phys. status Solidi B*, vol. 247, no. 4, pp. 774–788, 2010.

[76]   J. Zhang, L. Zhang, and W. Xu, "Surface plasmon polaritons: physics and applications," *J. Phys. D. Appl. Phys.*, vol. 45, p. 113001, 2012.

[77]   M. P. Nezhad, A. Simic, O. Bondarenko, B. Slutsky, A. Mizrahi, L. Feng, V. Lomakin, and Y. Fainman, "Room-temperature subwavelength metallo-dielectric lasers," *Nat. Photonics*, vol. 4, pp. 395–399, 2010.

[78]   K. Ding, Z. Liu, L. Yin, H. Wang, R. Liu, M. T. Hill, M. J. H. Marell, P. J. Van Veldhoven, R. Nötzel, and C. Z. Ning, "Electrical injection, continuous wave operation of subwavelength-metallic- cavity lasers at 260 K," *Appl. Phys. Lett.*, vol. 98, p. 231108, 2011.

[79]   K. Ding, Z. C. Liu, L. J. Yin, M. T. Hill, M. J. H. Marell, P. J. Van Veldhoven, R. Nœtzel, and C. Z. Ning, "Room-temperature continuous wave lasing in deep-subwavelength metallic cavities under electrical injection," *Phys. Rev. B*, vol. 85, p. 041301, 2012.

[80]   J. Y. Suh, C. H. Kim, W. Zhou, M. D. Huntington, D. T. Co, M. R. Wasielewski, and T. W. Odom, "Plasmonic bowtie nanolaser arrays," *Nano Lett.*, vol. 12, pp. 5769–5774, 2012.

[81]   J. H. Lee, M. Khajavikhan, A. Simic, Q. Gu, O. Bondarenko, B. Slutsky, M. P. Nezhad, and Y. Fainman, "Electrically pumped sub-wavelength metallo-dielectric pedestal pillar lasers," *Opt. Express*, vol. 19, no. 22, pp. 21524–21531, 2011.

[82]   K. Ding and C. Z. Ning, "Fabrication challenges of electrical injection metallic cavity semiconductor nanolasers," *Semicond. Sci. Technol.*, vol. 28, p. 124002, 2013.

[83]   E. S. Hosseini, S. Yegnanarayanan, A. H. Atabaki, M. Soltani, and A. Adibi, "High quality planar silicon nitride microdisk resonators for integrated photonics in the visible wavelength range," *Opt. Express*, vol. 17, no. 17, pp. 14543–14551, 2009.

[84]   A. Yariv, "Universal relations for coupling of optical power between microresonators and dielectric waveguides," *Electron. Lett.*, vol. 36, no. 4, pp. 321–322, 2000.

[85]   Q. Ding, A. Mizrahi, Y. Fainman, and V. Lomakin, "Dielectric shielded nanoscale patch laser resonators," *Opt. Lett.*, vol. 36, no. 10, pp. 1812–1814, 2011.

[86]   M. Kim, A. M. Lakhani, and M. C. Wu, "Efficient waveguide-coupling of metal-clad nanolaser cavities," *Opt. Express*, vol. 19, no. 23, pp. 23504–23512, 2011.

[87]   L. A. Coldren, S. W. Corzine, and M. L. Masanovic, *Diode Lasers and Photonic Integrated Circuits*, 2nd ed. Wiley, 2012.

[88]   T. Okimoto, "Research on InP-based multiple-quantum-well laser with metallic-cavity structure," *Master Thesis, Univ. Tokyo*, 2015.

[89]   A. Taflove and S. C. Hagness, *Computational Electrodynamics: The Finite-Difference Time-Domain Method*, 3rd ed. Artech House, 2005.

[90]   B. Zhang, T. Okimoto, T. Tanemura, and Y. Nakano, "Proposal and numerical study on capsule-shaped nanometallic semiconductor lasers," *Jpn. J. Appl. Phys.*, vol. 53, p. 112703, 2014.

[91] P. Wahl, D. S. Ly-Gagnon, C. Debaes, D. a B. Miller, and H. Thienpont, "B-CALM: An open-source GPU-based 3D-FDTD with multi-pole dispersion for plasmonics," *Opt. Quantum Electron.*, vol. 44, pp. 285–290, 2012.

[92] J. A. Roden and S. D. Gedney, "Convolution PML (CPML): An efficient FDTD implementation of the CFS-PML for arbitrary media," *Microw. Opt. Technol. Lett.*, vol. 27, no. 5, pp. 334–339, 2000.

[93] Y. Zou, J. S. Osinski, P. Grodzinski, P. D. Dapkus, W. C. Rideout, W. F. Shadin, J. Schlafer, and F. D. Crawford, "Experimental Study of Auger Recombination , Gain , and Temperature Sensitivity of 1 . 5 pm Compressively Strained Semiconductor Lasers," *IEEE J. Quantum Electron.*, vol. 29, no. 6, pp. 1565–1575, 1993.

[94] E. Zielinski, H. Schweizer, K. Streubel, H. Eisele, and G. Weimann, "Excitonic transitions and exciton damping processes in InGaAs/InP," *J. Appl. Phys.*, vol. 59, no. 6, pp. 2196–2204, 1986.

[95] K. Chieda, B. Zhang, T. Okimoto, T. Tanemura, and Y. Nakano, "Numerical Investigation on Compact Metallic-Cavity Optical Modulator Integrated on InP-Based Waveguide," in *iNOW-2015, August 3-7, Tokyo, Japan*, 2015.

[96] F. Karouta, "A practical approach to reactive ion etching," *J. Phys. D. Appl. Phys.*, vol. 47, p. 233501, 2014.

[97] D. M. M. and H. F. Dylla, "Plasma Etching: An Introduction," in *Plasma-Materials Interactions*, Academic Press, 1989.

[98] M. Zaitsu, "Polarization Control inside Photonic Integrated Circuits Using InP Half-Ridge Polarization Converters," *PhD Thesis, Univ. Tokyo*, 2014.

[99] S. J. Choi, K. Djordjev, S. J. Choi, and P. D. Dapkus, "CH_4-based dry etching of high Q InP microdisks," *J. Vac. Sci. Technol. B*, vol. 20, no. 1, pp. 301–305, 2002.

[100] J. H. den Besten, R. G. Broeke, M. van Geemert, J. J. M. Binsma, F. Heinrichshorff, T. van Dongen, E. A. J. M. Bente, X. J. M. Leijtens, and M. K. Smit, "An integrated 4×4-channel multiwavelength laser on InP," *IEEE Photonics Technol. Lett.*, vol. 15, no. 3, pp. 368–370, 2003.

[101] T. R. Hayes, M. A. Dreisbach, P. M. Thomas, W. C. Dautremont-Smith, and L. A. Heimbrook, "Reactive ion etching of InP using CH_4/H_2 mixtures: Mechanisms of etching and anisotropy," *J. Vac. Sci. Technol. B*, vol. 7, no. 5, pp. 1130–1140, 1989.

[102] I. Adesida, K. Nummila, E. Andideh, J. Hughes, C. Caneau, R. Bhat, and R. Holmstron, "Nanostructure fabrication in InP and related compounds," *J. Vac. Sci. Technol. B*, vol. 8, no. 6, pp. 1357–1360, 1990.

[103] S. J. Pearton, U. K. Chakrabarti, a. P. Kinsella, D. Johnson, and C. Constantine, "Electron cyclotron resonance plasma etching of InP in $CH_4/H_2/Ar$," *Appl. Phys. Lett.*, vol. 56, no. 15, pp. 1424–1426, 1990.

[104] M. Kuttge, E. J. R. Vesseur, J. Verhoeven, H. J. Lezec, H. a. Atwater, and A. Polman, "Loss mechanisms of surface plasmon polaritons on gold probed by cathodoluminescence imaging spectroscopy," *Appl. Phys. Lett.*, vol. 93, p. 113110, 2008.

[105] E. D. Palik, *Handbook of Optical Constants of Solids*. Academic Press, 1985.

Publications

Journal papers

[1] ***Baifu Zhang***, Takuya Okimoto, Takuo Tanemura and Yoshiaki Nakano, "Proposal and numerical study on capsule-shaped nanometallic semiconductor lasers", Jpn. J. Appl. Phys.53, 112703 (2014).

[2] ***Baifu Zhang***, Koh Chieda, Takuya Okimoto, Takuo Tanemura and Yoshiaki Nakano, "Q factor improvement by capsule-shaped cavity structure for subwavelength metallic lasers", submitted to Physica Status Solidi (a).

International conference

[3] ***Baifu Zhang***, Takuya Okimoto, Takuo Tanemura and Yoshiaki Nakano, "Capsule-Shaped Metallic-Cavity Laser with Reduced Plasmonic Loss", CLEO June 8-13, 2014 San Jose, U.S.A.

[4] ***Baifu Zhang***, Takuya Okimoto, Takuo Tanemura and Yoshiaki Nakano, "Observation of Q factor Improvement by Capsule-Shaped Subwavelength Metallic-Cavity Structures", IPRM-2015, June 28 – July 2, 2015 Santa Barbara, U.S.A.

[5] ***Baifu Zhang***, Koh Chieda, Takuya Okimoto, Takuo Tanemura and Yoshiaki Nakano, "Experimental confirmation of Q-factor enhancement by capsule-shaped cavity for sub-wavelength metallic laser", iNOW-2015, August 3–7, 2015 Tokyo, Japan.

[6] Koh Chieda, ***Baifu Zhang***, Takuya Okimoto, Takuo Tanemura and Yoshiaki Nakano, "Numerical Investigation on Compact Metallic-Cavity Optical Modulator Integrated on InP-Based Waveguide", iNOW-2015, August 3–7, 2015 Tokyo, Japan.

[7] Yufeng Fu, ***Baifu Zhang***, Jon Oyvind Kjellman, Takuo Tanemura, Yoshiaki Nakano, "Numerical study on hollow hexagonal InGaAs microdisk laser on silicon", IPRM-2014, May 11-15, 2014 Montpellier, France.

Domestic conference

[8] ***Baifu Zhang***, Koh Chieda, Takuya Okimoto, Takuo Tanemura and Yoshiaki Nakano, IEICE Society Conference, "InP-Based Capsule-Shaped Cavities for Sub-Wavelength Metallic Lasers", IEICE Society Conference, September 8-11, 2015 Sendai, Japan (invited).

[9] ***Baifu Zhang***, Takuya Okimoto, Takuo Tanemura and Yoshiaki Nakano, "Fabrication and photoluminescence characterization of capsule-shaped metallic InP/InGaAs cavity structures", JSAP Spring Meeting, March 11-14, 2015 Kanagawa, Japan.

[10] ***Baifu Zhang***, Takuya Okimoto, Takuo Tanemura and Yoshiaki Nakano, "Design of capsule-shaped cavity for nanometallic semiconductor lasers", IEICE Technical Report (LQE2014), LQE2013-125, Dec. 2013.

Acknowledgements

I would like to express my gratitude to all persons around me, without whose constant support and kind help I could not finish my PhD course.

First of all, I am very grateful to Prof. Yoshiaki NAKANO for giving me the opportunity to work in Nakano-Sugiyama-Tanemura lab and for his continuous support, help and encourage during my doctor course. I have benefitted greatly from him and his group, not only about several aspects of research, but also about the deep insight and broad perspective. The environment and atmosphere of Nakano group are full of international communications of different cultures, wisdoms and thoughts, and bring to me a sea of happiness and invaluable experience during my life in Tokyo.

I would like to appreciate to Prof. Takuo TANEMURA for his great helps and supports. During the time I spend here, he was always kind and patient enough to listen to my countless queries and taking time to inspire me and solve all of them, including the valuable advice of my research plan, instructive discussions on physical theories, analysis of the experimental data, and patient corrections of my research papers and presentations. All these activities are the precious memories of my PhD course.

I also appreciate to Prof. Masakazu SUGIYAMA for his insightful advice and comments at laboratory meetings, from which I get enlightened from various perspectives and viewpoints. His great enthusiasm on research encourages me a lot to chase my PhD degree.

I specially appreciated to Prof. Yasunobu NAKAMURA and Prof. Shinji YAMASHITA, who are the committee members of my doctoral defense. I profited a lot from their valuable and indispensable suggestions, advices and questions, which make my research more reasonable and systemic. Their amiable attitude to young generations and keen insight into science impressed me greatly.

I would like to specially thank to Dr. Kejellman Jon and Mr. Takuya Okimoto, for their numerous discussions and a great help in detailed research activities. They were always selfless to share valuable research experience, and were friendly to have communications with me among various areas. I benefited a lot from their kindness and wisdom.

During my three years in the University of Tokyo, many people offered me selfless help and kind encouragement, including Assistant Prof. Kentaroh Watanabe, Assistant Prof. Akio Higo, Assistant Prof. Yupeng Wang, Assistant Prof. Hassanet Sodabanlu, Dr. Myung-Joon Kwack, Dr. Masaru Zaitsu, Dr. Hiromasa Fujii, Dr. Cai Liu, Dr. Hongbo Wang, Dr. Heng Zhong, Mr. Akihiro Nakamura, Mr. Yuxiao Zeng, Mr. Yufeng Fu, Mr. Ming Cui, Mr. Mohiyuddin Atharuddin Kazi, Mr. Masafumi Ayata, Mr. Kasidit Toprasertpong, Mr. Warakorn Yanwachirakul, Mr. Koh Chieda, Mr. Yudo Kawabata, Mr. Kentaro Suzuki, Mr. Masaharu Fukuda and Ms. Wenhui Zhan. And also I acknowledge to all the members of Nakano lab for their kindness and cooperation, and our happy study life.

Last but not least, I wish to express my deepest gratitude to my parents, who offer constant support and encouragement to me forever.

Baifu Zhang

Tokyo

2015 Summer